RESOLUTION-LOSSLESS ULTRASOUND TOMOGRAPHY FOR HEALTH MONITORING OF COMPOSITE STRUCTURES:
FROM NANOCOMPOSITE SENSOR NETWORK DEVELOPMENT TO MACHINE LEARNING-ENABLED IMAGING

JIANWEI YANG

PhD

The Hong Kong Polytechnic University

2022

The Hong Kong Polytechnic University

Department of Mechanical Engineering

Resolution-lossless Ultrasound Tomography for Health Monitoring of Composite Structures: *from Nanocomposite Sensor Network Development to Machine Learning-enabled Imaging*

Jianwei YANG

A thesis submitted in partial fulfilment of the requirements for the degree of Doctor of Philosophy

June 2022

CERTIFICATE OF ORIGINALITY

I hereby declare that this thesis is my own work and that, to the best of my knowledge and belief, it reproduces no material previously published or written, nor material that has been accepted for the award of any other degree or diploma, except where due acknowledgment has been made in the text.

YANG Jianwei

ABSTRACT

Ultrasound tomography (UT), by virtue of its high accuracy, intuitive presentation of results and standardized implementation, has gained prominence in structural health monitoring (SHM)-driven integrity assurance and health management of composite structures. With an appropriately selected type of sensor, UT for SHM canvasses subtle variation in ultrasound signals by benchmarking pristine counterparts, subsequently associates the variation to material deterioration or damage occurrence, and projects evaluation results in pixelized images through proper tomographic imaging algorithms.

However, a densely configured sensor network, either externally mounted on or internally implanted in composites, alters the microstructure of the fibre-reinforced matrix, influences the interlaminar stress distribution in the sensor vicinity, introduces artificial defect, and consequently lowers the structural load-carrying capacity. On the other hand, any attempt to minimize such intrusion by limiting the sensor number is usually at the cost of undermining the detection resolution and accuracy. Indeed, it is a challenging task to strike a balance between the sensing cost (*i.e.*, the number of sensors) and sensing effectiveness (*i.e.*, the accuracy of tomography) when implementing UT-based SHM.

In this PhD study, an implantable, nanocomposite-inspired, piezoresistive sensor network is developed for implementing UT-based SHM of carbon fibre-reinforced polymer (CFRP) laminates. The nanocomposite ink, formulated with graphene nanosheets (GNSs) and polyvinylpyrrolidone (PVP), is tailored to acquire the percolation threshold of conductive nanofillers. The above ink is then deposited on partially precured B-stage epoxy films using spray deposition process and circuited via highly conductive carbon nanotube fibres (CNT-fibres) as wires, to form a dense sensor network, which is then implanted into CFRP laminates during autoclaving procedure. With a morphologically optimized nano-architecture in nanocomposites, the quantum tunnelling effect can be triggered in percolated networks, which enables the sensors to faithfully response from quasi-static loads to high-frequency guided ultrasonic waves (GUWs). Quasi-static tensile test is performed to gauge possible degradation in tensile properties and change in failure modes of the CFRP laminates owing to the implantation of a sensor network.

Using the developed implantable sensor network, in conjunction with the use of only a handful of surface-mounted PZT wafers as excitation sources, a dense sensor network can be configured, to circumvent the *limited-angle problem* that conventional UT-based imaging algorithms may have. The implanted sensor network has been proved owing the capability in perceiving GUWs in a broad frequency regime with high precision up to 450 kHz experimentally. The enhanced reconstruction algorithm for the probabilistic inspection of damage (RAPID)-based imaging algorithm, which is revamped by continuously iterating and updating the scale parameter β, presents superior accuracy, compared with the conventional RAPID algorithm when used to evaluate both the location and shape of anomaly, endowing the UT-based SHM with higher imaging resolution while not at the cost of sacrificing the composites' original integrity.

To further achieve real *in-situ* UT-based SHM and solve the restricted sensing capability due to inadequate sensing paths in the implanted sensor network, a hierarchical, algebraic reconstruction technique (ART) based tomographic imaging approach, facilitated by convolutional neural network (CNN) based machine learning (ML), is developed, targeting resolution-lossless tomography for SHM of composites. The blurry ART images, as the inputs to train a CNN with an encoder-decoder-type architecture, are segmented using convolution and max-pooling to extract defect-modulated image features. The max-unpooling boosts the resolution of ART images with transposed convolution. Trained with the insufficient databases via a mixed numerical and experimental method, the CNN is used to detect and characterize artificial anomaly and delamination in the CFRP laminates. Results demonstrate that the developed approach accurately images artificial anomaly and delamination, in the meantime it minimizes the false alarm by eliminating image artifacts.

In conclusion, starting from mechanism study, through design to fabrication of sensors, new breeds of implantable, nanocomposite-inspired, piezoresistive sensor network is developed. Successful application paradigms in UT of the implanted sensor network, either using the enhanced RAPID or ML-enabled imaging, have accentuated the alluring potentials of *in-situ* UT-based SHM.

A LIST OF PUBLICATIONS ARISING FROM THIS STUDY

Refereed Journal Papers

1. **Yang, J.**, Su, Y., He, Y., Zhou, P., Xu, L., & Su, Z. (2022) Machine learning-enabled resolution-lossless tomography for composite structures with a restricted sensing capability. ***Ultrasonics***, 125, 106801.
2. **Yang, J.**, Su, Y., Liao, Y., Zhou, P., Xu, L., & Su, Z. (2022). Ultrasound tomography for health monitoring of carbon fibre–reinforced polymers using implanted nanocomposite sensor networks and enhanced reconstruction algorithm for the probabilistic inspection of damage imaging. ***Structural Health Monitoring***, 21(3): 1110-1122.
3. Su, Y., Xu, L., Zhou, P., **Yang, J.**, Wang, K., Zhou, L. M., & Su, Z. (2022). *In-situ* cure monitoring and in-service impact localization of FRPs using pre-implanted nanocomposite sensors. ***Composites Part A: Applied Science and Manufacturing***, 154, 106799.
4. Xu, L., Wang, K., Su, Y., He, Y., **Yang, J.**, Yuan, S., & Su, Z. (2022). Surface/sub-surface crack-scattered nonlinear Rayleigh waves: A full analytical solution based on elastodynamic reciprocity theorem. ***Ultrasonics***, 118, 106578.
5. Su, Y., **Yang, J.**, Liao, Y., Zhou, P., Xu, L., Zhou, L. M., & Su, Z. (2021). An implantable, compatible and networkable nanocomposite piezoresistive sensor for *in-situ* acquisition of dynamic responses of CFRPs. ***Composites Science and Technology***, 208, 108747.

6. Su, Y., Xu, L., Zhou, P., **Yang, J.**, Wang, K., Zhou, L. M., & Su, Z. (2021). Carbon nanotube-decorated glass fibre bundles for cure self-monitoring and load self-sensing of FRPs. ***Composites Communications***, 27, 100899.
7. Li, Y., Wang, K., Wang, Q., **Yang, J.**, Zhou, P., Su, Y., ... & Su, Z. (2021). Acousto-ultrasonics-based health monitoring for nano-engineered composites using a dispersive graphene-networked sensing system. ***Structural Health Monitoring***, 20(1), 240-254.
8. Zhou, P., Yang, X., Su, Y., **Yang, J.**, Xu, L., Wang, K., ... & Su, Z. (2021). Direct-write nanocomposite sensor array for ultrasonic imaging of composites. ***Composites Communications***, 28, 100937.
9. Zhou, P., Liao, Y., Yang, X., Su, Y., **Yang, J.**, Xu, L., ... & Su, Z. (2021). Thermally stable, adhesively strong Graphene/Polyimide films for inkjet printing ultrasound sensors. ***Carbon***, 184, 64-71.
10. Xu, L., Wang, K., Yang, X., Su, Y., **Yang, J.**, Liao, Y., ... & Su, Z. (2021). Model-driven fatigue crack characterization and growth prediction: A two-step, 3-D fatigue damage modeling framework for structural health monitoring. ***International Journal of Mechanical Sciences***, 195, 106226.
11. Zeng, Z., Zhang, C., Lin, B., **Yang, J.**, Liu, X., Wang, T., ... & Dai, Y. (2021). Eddy current testing of residual stress state in aluminum alloy. ***IEEE Transactions on Instrumentation and Measurement***, 70, 1-8.
12. Zhou, P., Cao, W., Liao, Y., Wang, K., Yang, X., **Yang, J.**, ... & Su, Z. (2020). Temperature effect on all-inkjet-printed nanocomposite piezoresistive sensors for ultrasonics-based health monitoring. ***Composites Science and Technology***, 197, 108273.

Refereed Conference Papers

1. **Yang, J.**, Su, Y., Zhou, P., Xu, L., & Su, Z. (2022) Convolutional neural network enabled resolution-lossless tomography for composites with restricted sensing capability. ***in Proceedings of 9th Asia Pacific Workshop on Structural Health Monitoring***.
2. **Yang, J.**, Su, Y., Zhou, P., Xu, L., & Su, Z. (2021) Enhanced RAPID tomography for health monitoring of CFRPs using implanted nanocomposite sensor networks. ***in Proceedings of the 13th International Workshop on Structural Health Monitoring***.
3. Su, Y., **Yang, J.**, Xu, L., Zhou, P. & Su Z. (2021) An implantable, compatible and networkable nanocomposite sensor for continuous monitoring of FRPs. ***in Proceedings of the 13th International Workshop on Structural Health Monitoring***.

ACKNOWLEDGEMENTS

First and foremost, I am extremely grateful to my supervisor, Prof. Zhongqing Su, for his invaluable advice, continuous support, and patience during my PhD study. His immense knowledge and plentiful experience have encouraged me all the time in my academic research and daily life. Without his enlightening instruction and meticulous supervision, it would be an impossible mission for me to continue my study and complete this thesis. It is my great fortune to complete my PhD study under his supervision.

Throughout this venture, I also express my gratitude to my friends. It is a great fortune to meet them and get acquainted in Hong Kong. I am indebted to Dr. Yaozhong Liao, Dr. Kai Wang, Dr. Yehai Li, for their timely guidance and help during my study period. With help from Dr. Lei Xu, Dr. Yiyin Su, Dr. Pengyu Zhou, Dr. Xiongbin Yi, Mr. He Yang, and Mrs. Tianhui Lu, I am able to make my research progress and my life full of joy at HKPU.

Last but not least, I would like to express my deepest appreciation to my family, for their love, care, and patience at all times. Special thanks to beloved Mrs. Xin Zhang, as well as her family. Their encouragement and support help me overcome various obstacles in pursuing my PhD degree.

NOMENCLATURE

Acronyms and Initialisms

UT	Ultrasound tomography
SHM	Structural health monitoring
CFRP	Carbon fibre-reinforced polymer
GNS	Graphene nanosheet
PVP	Polyvinylpyrrolidone
CNT	Carbon nanotube
GUW	Guided ultrasonic wave
RAPID	Reconstruction algorithm for the probabilistic inspection of damage
ART	Algebraic reconstruction technique
CNN	Convolutional neural network
ML	Machine learning
CT	Computed tomography
FBP	Fan-beam projection
FWI	Full waveform inversion
ANN	Artificial neural network
NDE	Non-destructive evaluation
PZT	Lead zirconate titanate
EMAT	Electromagnetic acoustic transducer
PVDF	Polyvinylidene fluoride
CPC	Conductive polymer composite

CB	Carbon black
ICT	Inductively coupled transducer
ToF	Time of flight
SVM	Support vector machine
EML	Extreme learning machine
PNN	Probabilistic neural network
FAN	Fuzzy ARTMAP network
LSSVM	Least square support vector machine (LSSVM)
1-D	One-dimension
PI	polyimide
SEM	Scanning electron microscope
AVE	Advanced video extensometer
SDC	Signal difference coefficient
Res-Conn	Residual connection
BN	Batch normalization
3-D	Three-dimension
FE	Finite element

Symbols

u	Displacement
f	Body force
ρ	Density
μ	Shear modulus
λ	Lamé constant
E	Young’s modulus
v	Poisson’s ratio
h	Half-thickness of the infinite isotropic plate
k_{wave}	Wavenumber
ω	Circular frequency
λ_{wave}	Wavelength
C_L	Velocity of longitudinal mode
C_T	Velocity of transverse/shear mode
L	Longitudinal mode
T	Transverse/shear mode
S_i	Symmetric mode
A_i	Anti-symmetric mode
σ	Electrical conductivity of nanofiller-dispersed composites
p	Volume fraction of nanofillers
p_c	Percolation threshold of composites
t	Exponential constant of composites
$R_{nanoparticle}$	Intrinsic resistance of nanoparticles
$R_{contact}$	Constriction resistance of nanoparticles

R_{tunnel}	Tunnelling resistance of nanoparticles
V	Electrical potential difference
J	Tunnelling current density
A_t	Cross-sectional area of tunnel
h_{planck}	Planck’s constant
d_n	Distance between two nanoparticles,
e	Quantum of electricity
m	Mass of electron
λ_l	Potential height of insulating layer
$\mathrm{Cov}(X, Y)$	Covariance of signal X and signal Y
X_k	Discretized form of X
Y_k	Discretized form of Y
K	Discretized data
μ_{X}	Mathematical expectation of X
μ_Y	Mathematical expectation of Y
$P(x, y)$	Defect distribution probability
(x, y)	Coordinate of an arbitrary point in inspection region
M	Number of actuators
N	Number of sensors
$P_{ij}(x, y)$	Probability of defect at (x, y) estimated by sensing path $[i, j]$
i	Actuator i
j	Sensor j
SDC_{ij}	Signal difference coefficient calculated by sensing path $[i, j]$
$w_{ij}(x, y)$	Weighted matrix related to spatial distribution of defect
l	Distance between two points indicated in subscript

β	Scaling parameter
(x_d^0, y_d^0)	Coordinate of initially estimated defect location
(x_d^n, y_d^n)	Coordinate of updated defect location after n iterations
$A[i, j]$	Magnitude of GUW signal
A_{ini}	Initial amplitude of probing GUW signal
$\mu[m, n]$	Attenuation of GUW signal in cell $[m, n]$
$d[i, j, m, n]$	Distance in cell $[m, n]$ along sensing path $[i, j]$
C	Wave attenuation constant
$\mu^0[m, n]$	Estimated initial attenuation value in cell $[m, n]$
$\Delta_{average}\mu[m, n]$	Average difference of attenuation value
k	Iteration number
$L[i, j]$	Length of sensing path $[i, j]$
C^{l-1}	Input of l^{th} convolution layer
C^l	Output of l^{th} convolution layer
K^l	Convolution kernels
b^l	Offset
f_{act}	Non-linear activation function

TABLE OF CONTENTS

LIST OF FIGURES

LIST OF TABLES

CHAPTER 1

Introduction

1.1 Background and Motivation

Composite structures have been increasingly adopted by the aerospace industry to provide significant weight reduction and substantial performance enhancement. However, composite structures are highly vulnerable to low-velocity impacts for their low transverse strength, resulting in various types of defect such as delamination, indentation, fibre breakage or matrix cracking, leading to catastrophic failure of the entire structure without timely detection of the defect after it accumulates above a critical threshold. This has entailed strong needs of effective, rapid and efficient inspection technique which can characterize the defect in its early stage, so as to ensure the durability and reliability of composite structures.

Facilitated by recent scientific advances and technological breakthroughs in sensing technology, material sciences, additive manufacturing, electronic packaging, and signal processing, structural health monitoring (SHM)-driven integrity assurance and health management has evolved to become a standard building block in various industrial sectors. SHM denotes a system with the ability to detect and interpret adverse “changes” in a structure under inspection in a real-time manner when the structure is subjected to progressive ageing and material deterioration throughout service life [1]. Successful implementation of SHM on composite structures has been proven effective in reducing maintenance cost, accompanying the substantial improvement of reliability and safety.

Amidst diverse SHM approaches, ultrasound tomography (UT), irrespective of the popularity and demonstrated effectiveness of for damage evaluation, has become an attractive technique by interpreting the transmission of ultrasonic energy through an object, on which basis UT approaches characterize material properties and detect material defect [2-11]. Sharing a similar principle with that of the X-ray-based computed tomography (CT) in clinics, UT-based SHM explores subtle variation in propagation characteristics of ultrasonic waves guided by the object under inspection, to image changes in the object caused by structural damage or material degradation, via appropriate tomographic imaging algorithms such as fan-beam projection (FBP), algebraic reconstruction technique (ART), full waveform inversion (FWI), and reconstruction algorithm for probabilistic inspection of damage (RAPID). However, conventional UT by virtue of imaging algorithms including FBP, ART, FWI and RAPID often shows inferior accuracy when insufficient sensors are used, due to the narrow scanning angle and inadequate number of sensing path available in the sensor network, during tomographic image reconstruction – a deficiency referred to as *limited-angle problem* [12]. The limited-angle scanning can make signal acquisition incomplete, potentially leading to ignorance of damage in certain areas within the inspection region. To warrant a broad scanning angle and sufficient sensing paths for reconstruction of a precise tomographic image, sensors have to be configured in a dense manner. Nevertheless, a densely configured transducer network alters the microstructure of the fibre-reinforced matrix, influences the interlaminar stress distribution in the sensor vicinity, introduces artificial defect, and consequently lowers the structural load-carrying capacity. Indeed, it is a challenging task to strike a balance between the sensing cost (*i.e.*, the number of sensors) and sensing effectiveness (*i.e.*, the resolution and accuracy of tomography) when implementing UT-based SHM for composite structures.

In terms of the sensing cost, to perceive signals for implementing UT, a deliberately designed transducer network [12-28], in either a dense or sparse a configuration, has to be externally mounted to or internally implanted into the composite structures under monitoring. However, among commercially available transducers, there is barely one with both qualified sensitivity and compatibility, either the sensitivity is limited by its intrinsic capacity, or the sensor is too rigid and brittle. Moreover, with inevitable intrusion to the original structure, a multitude of sensors, in whichever type, may degrade the structural integrity to some extent, regardless of their intended role of detecting defect or damage-caused structural deterioration. This possibly lowers local material strength, introduces defect/stress concentration/debonding, downgrades resistance to corrosion, and imposes weight and penalty to original structures due to unwieldy cables and wires used in a sensor network. The advances and technological breakthroughs in emerging nanotechnology make it possible to develop new kinds of sensors capable of accommodating demanding sensing requirements for high-precision SHM. In such a backdrop, it is imperative to develop new genres of sensor that are able to strike a compromise among flexibility (adaptability to curved structures), weight (low mass addition to inspected structures), volume (ignorable degradation in mechanical properties of inspected structures), and very importantly, responsivity and sensitivity (capability of perceiving broad signals up to an ultrasonic frequency regime), whereby to implement *in-situ* UT-based SHM.

Taking into account the sensing effectiveness, machine learning (ML), as represented by artificial neural network (ANN) and convolutional neural network (CNN), has emerged as a prevalent data-driven technique to predictively model high-degree complexity and abstraction. As mentioned previously, any attempt to minimize such intrusion by limiting the transducer number is usually at the cost of undermining the detection resolution and accuracy, because the reconstruction of a precise ultrasound tomographic image is guaranteed only when the sensor network for signal acquisition is of adequate density. To overcome this common problem, the matrix convolution operation is introduced, in which only key features of inputs are extracted for the training – known as CNN [29]. CNN has proven capability of exploring complex non-linear mappings between inputs and outputs – a daunting task to conventional ANN [30-36]. The introduction of CNN-based ML endows UT with the ability in targeting resolution-lossless tomography of composite structures with a restricted sensing capability. However, the accuracy and effectiveness of CNN depend substantially on a multitude of factors including mainly the training algorithms adopted, completeness of data available for training, and compatibility of a trained database to new inputs which are not included in the training. These factors, by nature, may narrow the application spectrum of ML-driven SHM. The significance of enhancing the compatibility and applicability of a trained database, with minimal extra effort to re-train an CNN, cannot be overemphasized.

1.2 Research Objectives

Aimed at circumventing the above commented deficiencies in prevailing UT-based SHM for composite structures, this PhD study is dedicated to developing a new nanocomposite-inspired sensor network, which can be implanted into composite structures, featuring sufficient sensitivity to guided ultrasonic waves (GUWs), for implementing *in-situ* resolution-lossless tomography based on CNN-based ML and facilitated by ART and RAPID. Driven by this target, the following objectives are embraced in this study:

(i) to fabricate a new breed of implanted nanocomposite-inspired sensor network with an enhanced sensing capability, improved mechanical properties and reduced weight;

(ii) to optimize and simplify the manufacturing process of implanted nanocomposite-inspired sensor network;

(iii) to demonstrate the capability of implanted nanocomposite-inspired sensor network of capturing dynamic signals from low frequency dynamic vibration, through medium frequency impact, to guided ultrasonic waves;

(v) to deliver resolution-lossless tomography for SHM of composite structures, based on CNN-based ML and facilitated by ART-based imaging algorithm.

1.3 Scope of the Thesis

In this PhD study, an implantable, nanocomposite-inspired, piezoresistive sensor network is developed for implementing *in-situ* resolution-lossless UT-based SHM of composite structures. This thesis is systematically organized in the order of fabrication of implantable piezoresistive sensor network, acquisition of GUWs using implanted sensor network, enhancement of RAPID imaging, construction of CNN-enabled ART imaging, and proof-of-concept application paradigms.

In Chapter 2, to start with, the basic concept of GUW-based SHM – a non-invasive and real-time technique of monitoring the integrity of composite structures, is introduced, and the theoretical fundamentals of guided ultrasonic waves are briefly summarized. Irrespective of the popularity and demonstrated effectiveness of UT for damage evaluation, several practical tomographic imaging approaches are presented and compared. Central to the realization of UT-based SHM is extracting structural health information from acquired wave signals. Ultrasonic wave signals are acquired by ultrasound sensors, and thus ultrasound sensors play the irreplaceable yet paramount role in an SHM system. Various categories of ultrasound sensors for this purpose are also summarized, including nanocomposite-inspired sensors and implanted sensors. Finally, considering the superior capability of ML in improving the sensing effectiveness of UT, recent studies on ML-facilitated SHM are reviewed, including the application of ANN and CNN. At the same time, the theoretical fundamentals of CNN are briefly summarized according to the categories of network architectures and activation functions.

In Chapter 3, in recognition of the deficiency of existing UT approaches for composite structures, a new breed of nanocomposite-inspired, piezoresistive sensor network is developed using a spray deposition process. Individual sensors, deposited on a pre-treated B-stage epoxy film, are networked via highly conductive carbon nanotube fibres as wires, to form a dense sensor network. Flexible, light, sensitive to broadband dynamic signals, the sensor network is implanted into CFRP laminates, to fulfil GUWs-based UT. Morphological characterization is performed to observe the interface between the CFRP laminate and implanted sensing unit, meanwhile to investigate the intrusion of the implanted sensor network to the host composites. Quasi-static tensile test is performed to gauge possible degradation in tensile properties and change in failure modes of the CFRP laminates owing to the implantation of a sensor network.

In Chapter 4, using the developed implantable sensing units, a dense sensor network can be configured, to circumvent the limited-angle problem that conventional UT-based imaging algorithms may have. Especially for the conventional RAPID algorithm, the selection of a constant parameter is inadequate to warrant accurate depiction of defect when the defect is at an arbitrary position within the inspection region. By introducing the continuously iterated and updated scaling parameter , the RAPID-based imaging algorithm is enhanced to facilitate processing of inadequate signals rendered by the sensor network, resulting in not only the improved accuracy of defect localization, but also the enhanced geometrical depiction and severity estimate of defect. Experiment is conducted to demonstrate fidelity of acquired GUW signals, showing no remarkable discrepancy in sensing performance between the developed implantable sensor network over a broad frequency range, and examine accuracy of the enhanced RAPID algorithm.

In Chapter 5, a hierarchical, ART-based UT approach, facilitated by CNN-based ML, is developed, targeting resolution-lossless tomography for SHM of composite structures, even when the sensing capability of the composite structures is restricted owing to inadequate transducers of the sensor network. In this approach, a CNN, which features encoder-decoder-type architecture including the convolution and transposed convolution blocks with residual connections, is configured. The blurry ART images, as CNN inputs, are segmented using convolution and max-pooling to extract defect-modulated image features. The max-unpooling boosts the resolution of ART images with transposed convolution. For validation, the sensing capability of a sensor network, which is pre-implanted in a CFRP laminate, is purposefully restricted, to obtain an insufficient number of GUW signals via a mixed numerical and experimental method. Trained by the insufficient inputs, the CNN is used to detect and characterize artificial anomaly and delamination in the CFRP laminate.

Chapter 6 serves as the conclusion of the thesis, where recommendations for future research are also made.

CHAPTER 2

State of the Art: A Literature Review

2.1 Introduction

With the motivation to enhance structural safety, and drive down exorbitant maintenance cost of composite structures, this PhD study is dedicated to developing implanted nanocomposite-inspired sensor network for *in-situ* resolution-lossless UT-based SHM and ML techniques. This chapter reviews the state of the art of some key aspects of UT-based SHM and ML techniques that are related to this PhD study. To start with, the basic concept of GUW-based SHM – a non-invasive and real-time approach of monitoring the integrity of composite structures, is introduced, and the theoretical fundamentals of GUWs are briefly summarized. Irrespective of the popularity and demonstrated effectiveness of UT for damage evaluation, several practical tomographic imaging approaches are presented and compared. Central to the realization of UT-based SHM is extracting structural health information from acquired wave signals. As the most rudimental but a critical step throughout the implementation, ultrasound sensors play the irreplaceable yet paramount role. Various categories of ultrasound sensors for this purpose are also summarized, including nanocomposite-inspired sensors and implanted sensors. Considering the superior capability of ML in improving the sensing effectiveness of UT, recent studies on ML-facilitated SHM are reviewed, including applications of ANN and

CNN. At the same time, the theoretical fundamentals of CNN are briefly summarized according to the categories of network architectures and activation functions.

2.2 Guided Ultrasonic Wave-based Health Monitoring of Composite Structures

2.2.1 Basic Concept of SHM

In the past decades, composite structures have been widely used in various industrial sectors (*e.g.*, aerospace industries, civil infrastructure, and energy engineering, *etc.*) for its specific properties compared with metallic counterparts, such as high strength, high stiffness and light weight. However, composite structures are often damaged by low-velocity impacts, while such damages are often invisible and may lead to catastrophic failure. Hence, it calls for an effective and efficient inspecting technique which could detect the damage promptly and thus ensure the safety of these composite structures. Non-destructive evaluation (NDE) techniques, when included within the framework of structural health monitoring (SHM), offers exciting and challenging possibilities to meet such requirements. The advantages of bringing NDE and SHM together are that it facilitates life cycle management decisions, reduces inspection down time, eliminates component tear down, provides early warning of failure during operation, and brings about life cycle cost reduction [38]. Amongst the various industries that stand to benefit from such a combined approach, the aircraft industry perhaps is the most visible beneficiary, as it spends 27% of the life cycle cost on inspection [39].

SHM can be operated in two different manners: one is passive SHM and another is active SHM. Passive SHM is mainly used to measure the real-time parameters and then deduce the status of structural health by using same algorithms. For instance, thousands of sensors should be placed beforehand to supervisory control the flight status of an aircraft (*e.g.*, velocity of wind, turbulence, g-factors, aircraft structural vibration) and then use the prepared algorithms to deduce whether the aircraft still can fly safely or not and how much the remaining life is. It's difficult to locate where the damage occurred when using passive SHM. In comparison, active SHM is concerned with addressing the exact location of damage. Active SHM systems utilize actively generated GUWs of specific frequency and magnitudes. Such an active manner effectively minimizes the negative influence of signal noise, and enhances the system controllability and diagnosis accuracy. By interpreting changes of subtle GUWs features, multiscale damage or faults in an inspected structure can be pinpointed and characterized, either qualitatively or quantitatively, and the remaining service life of the structure can also be derived.

2.2.2 Fundamentals of Guided Waves

Elastic waves in a solid medium can be one of the modalities (*e.g.,* Rayleigh waves, Lamb waves, Stonely waves and Creep waves), distinguished by the motion of particles [1]. Particularly, among above modalities, Lamb waves are selected as the GUWs in SHM, based on the merits of Lamb waves under high frequency. Meanwhile, Lamb waves refer to those in thin plates that provide upper and lower boundaries to guide continuous propagation of the waves [40].

In a thin isotropic and homogeneous plate as shown in **Figure 2.1**, no matter what kind of wave modes is, elastics waves can be represented by the Cartesian tensor notation as [41]

$$(\lambda+\mu)\cdot\nabla(\nabla u)+\mu\cdot\nabla^2 u+\rho\cdot f=\rho\cdot\ddot{u}\,, \tag{2.1}$$

$$\lambda=\frac{E\cdot\mu}{(1+\nu)(1-2\nu)} \tag{2.2}$$

$$\mu=\frac{E}{2(1+\nu)} \tag{2.3}$$

In the above, u and f are the displacement and body force, respectively; ρ and μ are the density and shear modulus of the plate, respectively; λ signifies the Lamé constant that is related to the Young's modulus E and Poisson's ratio ν of the plate; $\nabla=\frac{\partial}{\partial x_1}+\frac{\partial}{\partial x_2}+\frac{\partial}{\partial x_3}$ and $\nabla^2=\frac{\partial^2}{\partial {x_1}^2}+\frac{\partial^2}{\partial {x_2}^2}+\frac{\partial^2}{\partial {x_3}^2}$.

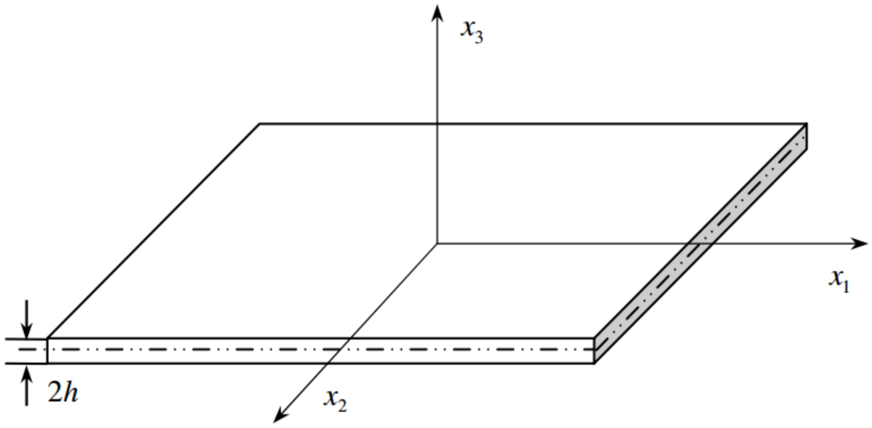

Figure 2.1 An infinite isotropic thin plate of 2*h* in thickness.

Lamb waves are guided to propagate in an isotropic and homogeneous plate, consisting of symmetric (in-plane motion) and anti-symmetric modes (out-of-plane motion). Both symmetric and anti-symmetric modes are of dispersive nature, showing strong dependence on wave excitation frequency, and Lamb waves can be expressed as [40]

$$\frac{\tan(qh)}{\tan(ph)} = -\frac{4k_{wave}^2 qp}{\left(k_{wave}^2 - q^2\right)^2} \qquad \text{for symmetric mode,} \tag{2.4}$$

$$\frac{\tan(qh)}{\tan(ph)} = -\frac{\left(k_{wave}^2 - q^2\right)^2}{4k_{wave}^2 qp} \qquad \text{for anti-symmetric mode.} \tag{2.5}$$

$$p^2 = \frac{\omega^2}{{C_L}^2} - k_{wave}^2,\ q^2 = \frac{\omega^2}{{C_T}^2} - k_{wave}^2,\ k = \frac{2\pi}{\lambda_{wave}}, \tag{2.6}$$

where h, k_{wave}, ω and λ_{wave} are the half-thickness of the plate, wavenumber, circular frequency and wavelength of the wave, respectively. C_L and C_T are the velocities of longitudinal and transverse/shear modes (L stands for the longitudinal modes and T the transverse/shear modes hereafter), respectively, defined by

$$C_L = \sqrt{\frac{E(1-\nu)}{\rho(1+\nu)(1-2\upsilon)}} = \sqrt{\frac{2\mu(1-\upsilon)}{\rho(1-2\nu)}}, \tag{2.7}$$

$$C_T = \sqrt{\frac{E}{2\rho(1+\nu)}} = \sqrt{\frac{\mu}{\rho}}, \tag{2.8}$$

In short, the Lamb wave can be divided into two different modes, using S_i and A_i (i = 0, 1) as the symbols, one is symmetric and the other is anti-symmetric. The lowest order of symmetric and anti-symmetric have the same subscript (showing as S_0 and

A_0, respectively). **Equations 2.4** and **2.5** are known as the Rayleigh-lamb equations. The schematics of particle motion in the symmetric and anti-symmetric Lamb wave modes are plotted in **Figure 2.2**, indicating the displacement direction of particles and the resulting motion. S_i modes predominantly have radial in-plane displacement of particles, **Figure 2.2(a)**, while A_i modes mostly have out-of-plane displacement, **Figure 2.2(b)**.

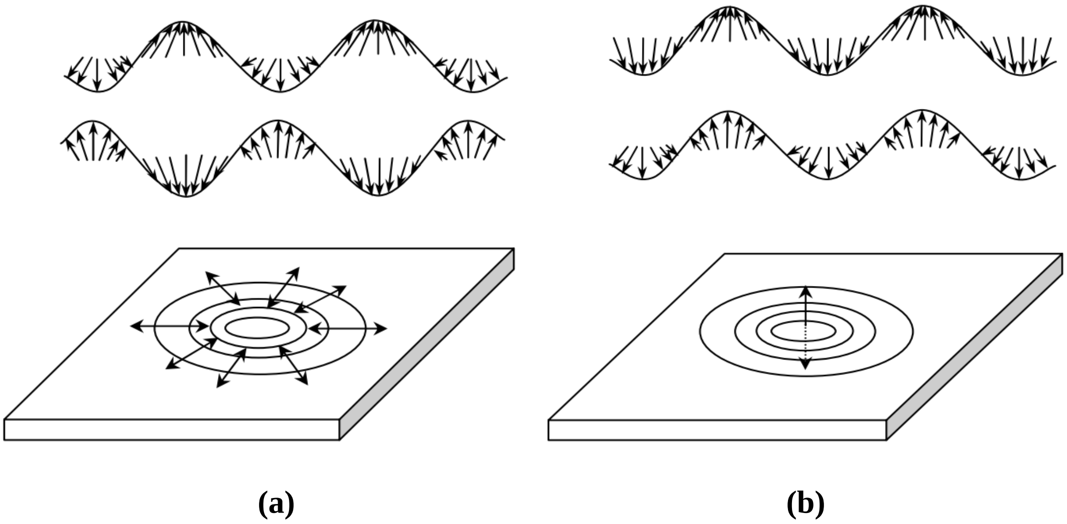

Figure 2.2 (a) Symmetric Lamb wave modes; (b) anti-symmetric Lamb wave modes

2.3 Ultrasound Tomography

UT, by virtue of its high accuracy, intuitive presentation of results and standardized implementation, has gained prominence in SHM-driven integrity assurance and health management of engineering assets. With an analogous principle as the CT using X-ray radiography in clinic, UT for SHM canvasses subtle variation in ultrasound signals by benchmarking pristine counterparts, subsequently associates the variation to material deterioration or damage occurrence, and projects evaluation results in pixelized images through proper tomographic imaging algorithms. SHM applications require that sensors be permanently installed on or implanted in structures. Consequently, only a limited number of sensors can be installed on a structure. This limited number of sensors impacts the resolution of the reconstructed tomographic image and the sensitivity of the inspection approach. In UT, it is important to choose a practical tomographic imaging approach in order to get a precise reconstructed tomographic image. **Table 2.1** summarizes the various UT techniques to date. Considering the advantages and limitations of each technique, common similarities emerge.

UT for SHM has been the core of intensive research over the years. Representatively, Hinders *et al.* [42-46] are among those trailblazers who first exploited guided wave-based tomography. In this series of pioneering studies, comprehensive theory of implementing UT for damage detection was developed, with proven effectiveness in detecting flaws and anomalies in metallic and composite structures [44]. Jansen *et al.* [47] used Lamb waves to reconstruct tomographic images for visualizing defect in metallic and composite structures via an ultrasonic immersion. McKeon *et al.* [43, 44] compared the FBP and ART – two popular approaches to implement UT, for characterizing damage in multi-layered aircraft structures, and concluded that ART showed higher accuracy and fidelity over FBP. Rose *et al.* [48, 49] extended the RAPID-based tomographic imaging to damage localization and growth monitoring, and compared RAPID against FBP and ART, in terms of the image quality and image construction efficiency, to argue that RAPID offered higher flexibility in sensor network configuration, greater tolerance to ambient noise, and faster image construction with higher resolution. Rao *et al.* [50, 51] proposed a full waveform inversion (FWI)-based tomography method and demonstrated its precision by evaluating the remaining wall thickness of an isotropic plate.

Table 2.1 Overview of existing UT techniques.

Technique	Description	Advantages and limitations
Contact tomography	Contact tomography uses standard piezoelectric sensors to excite and receive guided waves. The sensors are displaced using standard mechanical scanning instrumentation. Alternatively, the inspected part can be rotated while keeping the sensor position fixed.	**Advantages:** high spatial resolution and image resolution due to fine mechanical scanning indexing. **Limitations:** consistent coupling must be maintained between transducer and specimen; scanning hardware is bulky and expensive.
Air-coupled tomography	Air-coupled transducers excite and receive tomography guided waves at some lift-off from the specimen surface. The transducers and specimen are manipulated using mechanical scanning instrumentation similar that used with contact tomography.	**Advantages:** high spatial resolution and image resolution due to fine mechanical scanning indexing; no direct contact between transducer and specimen is required. **Limitations:** scanning hardware is bulky and expensive.
Immersion tomography	Immersion tomography submerges the specimen in ultrasonic immersion tanks. immersion transducers can be moved in one or two dimensions. Similarly, the specimen can be rotated on a turntable while keeping transducer position fixed.	**Advantages:** high spatial resolution and image resolution due to fine mechanical scanning indexing; no direct contact between transducer and specimen is required. **Limitations: s**canning hardware is bulky and expensive; specimen must be submerged in immersion tank.
Laser generation tomography	In laser generation tomography, a pulsed laser is used to excite a guided wave in the specimen. The transducer position is automatically controlled by a translation and/or rotation stage. Contact, air-coupled, and EMAT transducers can be used as receivers.	**Advantages:** high spatial resolution and image resolution due to fine mechanical scanning indexing; no direct contact between transducer and specimen is required. **Limitations:** scanning hardware is bulky and expensive; laser generation instrumentation is also bulky and expensive.

2.4 Nanocomposites Sensors and Implanted Sensors

Regardless of the popularity and proven effectiveness of UT for SHM, implementation of UT usually entails a deliberately designed transducer network in a dense configuration, using commercially available transducers shown in **Figure 2.3** and **Table 2.2**, as typified by metal-foil strain gauges [13], lead zirconate titanate (PZT) wafers [14-20], optical fibres [21], electromagnetic acoustic transducers (EMAT) [22], and piezoelectric polymer film-type sensors (*e.g.*, polyvinylidene fluoride (PVDF) and its copolymers) [23-28]. Among them, the sensitivity of strain gauges and PVDFs is limited inherently to signals of low frequency (lower than hundred kilohertz [52]), as a result of the low piezoelectric coefficients that PVDF-type sensors possess [53]; PZT wafers are rigid and unwieldy to adapting to a curved surface, and a transducer network with multitudinous PZT wafers introduces intrusion to host structures; optical fibre-based sensors are fragile, necessitating extra protection, and in generally they are insensitive to damage far from sensor vicinity. Implanting optical fibres into a structure not only complicates the fabrication process but may degrade local material strength; EMATs are typically used for evaluation of metallic structures only, and moreover the transduction efficiency is normally insufficient compared with most piezoelectric transducers.

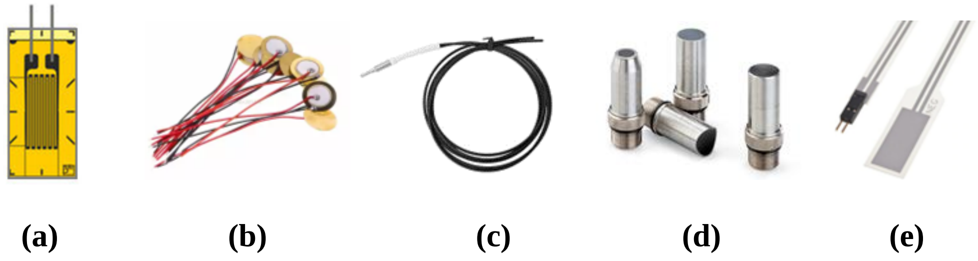

Figure 2.3 (a) Metal-foil strain gauge; (b) PZT wafers; (c) optical fibre; (d) acoustic transducers; (e) PVDF.

Table 2.2 Overview of commercially available transducers used in SHM.

Transducer	Applications	Installation
Metal-foil gauge	Detecting large and low-frequency deformations	Surface-mounted
PZT wafer	Detecting damage or working as active sensor	Surface-mounted or implanted
Optical fibre	Detecting deformation and damage	Surface-mounted or implanted
EMAT	Detecting structural damage or measuring thickness	Surface-mounted or air/fluid-coupled
PVDF	Detecting damage for large area and curved surface	Surface-mounted or implanted

With an appropriately selected type of transducer, a transducer network can be either externally mounted on or internally implanted in composites to implement UT. However, a densely configured transducer network, as shown in **Figure 2.4(a)**, when implanted, alters the microstructure of the fibre-reinforced matrix, influences the interlaminar stress distribution in the sensor vicinity, introduces artificial defect, and consequently lowers the structural load-carrying capacity, regardless of the fact that the intended role of the implanted transducer network is to monitor structural integrity degradation. On the other hand, any attempt to minimize such intrusion by limiting the transducer number is usually at the cost of undermining the detection resolution and accuracy, as illustrated in **Figure 2.4(b)**, because reconstruction of a precise tomographic image is guaranteed by rich information that can only be provided by a dense transducer network. Indeed, it is a challenging task to strike a balance between the sensing cost and sensing effectiveness when implementing UT-based SHM for composites using implanted transducers.

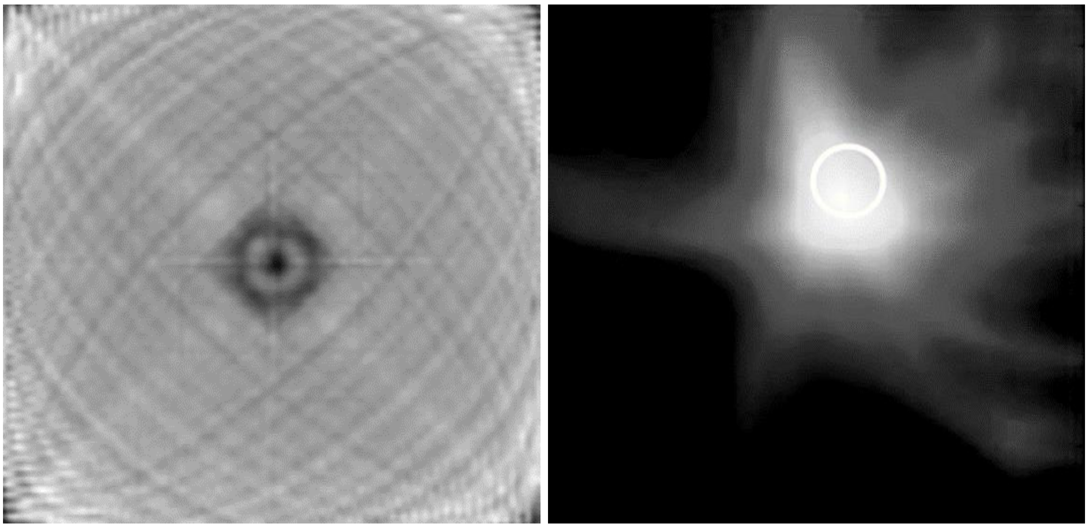

(a) **(b)**

Figure 2.4 (a) Dense sensor network with high resolution and accuracy; (b) sparse sensor network with low resolution and accuracy.

2.4.1 Nanotechnology

Nowadays, the most urgent thing for improving the SHM is to find out a new type of material to fabricate advanced sensors with new function and superior performance. Conductive polymer composites (CPCs) have proved to meet all the requirements, which can be typified by carbon black (CB), carbon nanotubes (CNTs), and graphene, as shown in **Figure 2.5**. The nanoscale of the nanofillers and mature synthetic technology allows them to be dispersed in polymer matrices uniformly, and the coalescence between nanofillers and polymers introduces some appealing and unique material features, such as low fabrication cost, low density, desired flexibility, easy tailorability in shape, immunity to corrosion, and favourable electrical-mechanical performance [54, 55].

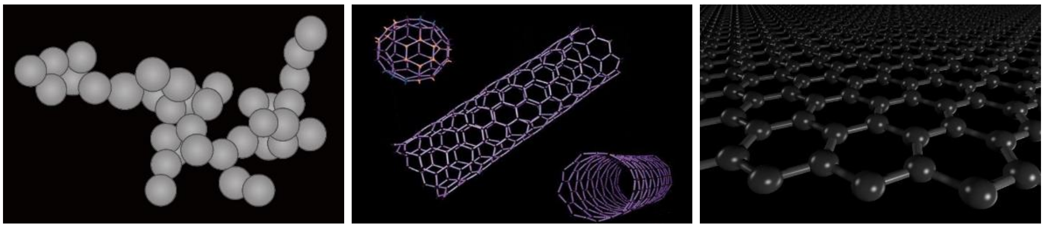

(a) **(b)** **(c)**

Figure 2.5 (a) Carbon black; (b) carbon nanotubes; (c) graphene.

CB is a material produced by the incomplete combustion of heavy petroleum products such as coal tar, ethylene cracking tar, and a small amount from vegetable oil. CB is a form of paracrystalline carbon that has a high surface-area-to-volume, but still lower than that of activated carbon. CB has been widely used as a conductive particle and in filled isolating polymer, because it is relatively inexpensive and manufacturing process is simple, but the most important property of CB is the superior performance in terms of its high electrical conductivity [54].

CNTs are allotropes of carbon with a cylindrical nanostructure, as a kind of novel functional material that has superiority in optical, electrical and mechanical properties, chemical and thermal stability. CNTs can be structured with length-to-diameter ratio of up to 132,000,000:1, significantly larger than for any other material. CNTs get its name from their surface morphology-long, hollow structure with the walls formed by one-atom thick sheets of carbon [56].

Graphene is an allotrope of carbon in the form of a two-dimensional, atomic-scale, hexagonal lattice in which one atom forms each vertex. It is the basic structural element of other allotropes, including graphite, charcoal, CNTs and fullerenes. The strength of graphene is about 200 times stronger than the strongest steel while the conductivity of graphene is 10^{-6} Ω·cm. Because of the single layer of atom which restricted the electrons can only transfer in a specific plane, graphene possesses a unique property that the kinematic velocity of electrons can reach 1/300 of the speed of light, far more than the kinematic velocity in general materials. Graphene also shows a large and nonlinear diamagnetism, even greater than graphite. Researchers have identified the bipolar transistor effect, ballistic transport of charges and large quantum oscillations in the material [57].

Upon evenly dispersed in a dielectric polymer, conductive nanofillers, such as 2-D graphene nanoparticles, can create an electrical network in the polymer. The electrical properties of the composites can be described, according to the percolation theory [58, 59], as

$$\sigma \propto (p - p^{c})^{t} , \tag{2.9}$$

where σ signifies the electrical conductivity of the nanofiller-dispersed composites, p the volume fraction of nanofillers, p_c the percolation threshold of the composites, and exponential t a constant associated with the composites. The percolation threshold represents a critical volume fraction of the nanofillers, beyond which a slight increase in the nanofiller content can give rise to a tremendous leap in the conductivity of the composites [58, 59]. In a nanoparticles-formed conductive network, the electrical resistance consists of three key components: the intrinsic resistance of nanoparticles ($R_{nanoparticle}$), the constriction resistance owing to direct contact of nanoparticles ($R_{contact}$), and the tunnelling resistance between two neighbouring nanoparticles (R_{tunnel}), namely

$$R = R_{nanoparticle} + R_{contact} + R_{tunnel} \,. \tag{2.10}$$

In particular, the tunnelling effect describes the phenomenon that when the insulative barrier between two neighbouring nanoparticles becomes thinner than a critical threshold, a tunnelling current can be triggered when electrons move through a barrier that they classically should not be able to move through. It is the quantum tunnelling effect that brings somewhat appealing and unique properties to nanocomposites such as semi-conductive properties. In **Equation 2.10**, R_{tunnel} is defined as [60]

$$R_{tunnel} = \frac{V}{A_t J} = \frac{2h_{planck}^2 d_n}{3A_t e^2 \sqrt{2m\lambda_l}} \cdot \exp\left(\frac{4\pi d_n}{h_{planck}} \sqrt{2m\lambda_l} \right), \tag{2.11}$$

where V denotes the electrical potential difference, J the tunnelling current density, A_t the cross-sectional area of the tunnel, h_{planck} the Planck's constant, d_n the distance between two nanoparticles, e the quantum of electricity, m the mass of electron, and λ_l the potential height of insulating layer. The tunnelling resistance, R_{tunnel}, depends on the thickness and material properties of the insulating layer, which is much higher than the other two types of resistance ($R_{nanoparticle}$ and $R_{contact}$) by a multitude of orders of magnitude. The tunnelling effect is particularly prominent when two nanoparticles are in a close proximity (of the order of several nanometres) but not in a direct contact. This stresses that at the percolation threshold, the quantum tunnelling effect dominates the electrical resistance manifested by the nanocomposites; beyond the threshold, nanoparticles become contacted or overlapped, under which the tunnelling effect tends to be weak and the conductivity of the nanocomposites saturates.

It is such an electro-mechanical property of the nanocomposites that serves the underlying mechanism to be harnessed, on which basis the conventional composites are functionalized, and endowed with a capability to respond to GUWs, as illustrated schematically in **Figure 2.6**. It is noteworthy that the GUW-induced strain features an extremely low magnitude that is of the order of several micro-strain, under which the tunnelling effect is the key mechanism resulting in change in the conductivity of the nanoparticles-formed sensing network as interpreted earlier. In virtue of the GUW-triggered tunnelling effect in the nanoparticles-formed percolating network, properly fabricated and optimized nanoparticles-dispersed composites can warrant desired sensitivity to propagating GUWs.

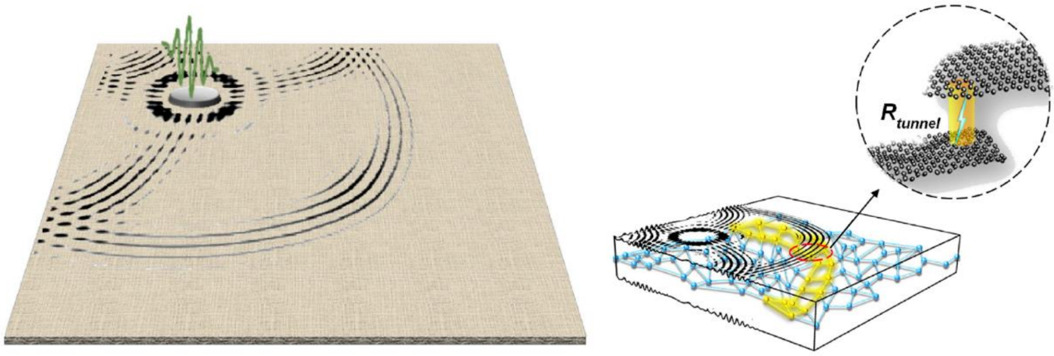

(a) **(b)**

Figure 2.6 (a) GUW excitation and propagation in a composite plate; (b) GUW-triggered tunnelling effect in the nanoparticles-formed percolating network, leading to change in local electrical resistance.

2.4.2 Nanocomposite-inspired Sensors

Recent advances in emerging nanotechnology have paved a new trail towards innovative sensors made of nanocomposites, to remarkably downsize a sensor but enhance its sensing capability. Nanocomposite sensors made of various carbon nanofillers show appealing features such as low density, good flexibility, environmental and chemical stability, along with superb sensitivity. This category of sensors has secured the superiority in measurement, detection and monitoring. Favourable examples include the measurement of material strain induced by quasi-static loads [61, 62] or under low-frequency dynamic loads [63, 64], and identification of structural damage [65, 66]. Representatively, Qin *et al*. [67] reported a type of graphene/PI nanocomposites that showed enhanced sensitivity to structural deformation under compression, bending, stretching and torsion. Wu *et al*. [68] designed piezoresistive strain sensors consisting of vertical graphene nanosheets that were arranged in a maze-like network and sandwiched between two polydimethylsiloxane substrates, and the sensors presented good stretchability, excellent linearity and high sensitivity to dynamic strains when compared with conventional metal-foil strain sensors. Qiu *et al*. [63] fabricated graphene-based cellular elastomers with reduced graphene oxide, and thus-produced elastomers could provide instantaneous and high-fidelity electrical response to dynamic pressures up to 2 kHz. Zeng *et al.* [69, 70] developed a CB/PVDF sensor that was able to respond to dynamic responses in a broadband frequency regime from static strain, through medium-frequency structural vibration, to high-frequency ultrasound. Liu *et al.* [52] attempted a new nanocomposite sensor, coatable on a structural surface, in lieu of conventional PZT wafers. This type of sensor showed high fidelity, ultrafast response, and great sensitivity to broadband acoustic-ultrasonic signals, and captured signals were comparable with those obtained using commercial sensors such as PZT wafers. Liao *et al.* [71, 72] investigated a nano-engineered thin film-type piezoresistive sensor, as shown in **Figure 2.7**, coatable or sprayable on a structural surface for *in-situ* acquisition of dynamic strain up to 1.4 MHz. Nevertheless, traditional metallic cables and wires, to network individual sensors for forming a sensor network, are still of necessity in these approaches. The use of printed circuits [73, 74] may, to some extent, reduce the weight and volume of cables and wires, but the surface-mounted printed circuits show high likelihood of detachment from the host structures under cyclic loads.

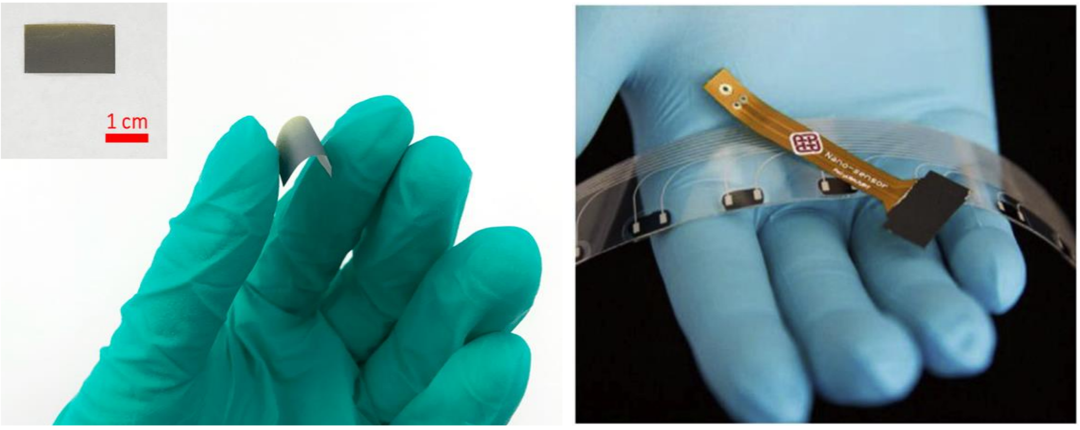

(a) **(b)**

Figure 2.7 Produced spray-on nanocomposite sensor: (a) a screen-printed nanocomposite flake, showing resilience; (b) a self-contained sensor with electrode pair.

2.4.3 Implanted Sensors

In various current applications, signals are collected using surface-mounted transducers, for their convenience of attachment, maintenance and replacement. However, with inevitable intrusion to composite structures, these sensors (*e.g.*, PZT) per se, degrade the structural integrity to some extent, regardless of their intended role of detecting damage-caused structural degradation. They possibly lower local material strength, introduce defect, stress concentration and debonding, downgrade resistance to corrosion, and, owing to the use of cables and wires for networking individual sensors, impose weight and penalty to original composite structures. Such degradation due to sensor intrusion is further intensified when structures are manipulated in cruel environment. Under cyclic loads, integrated sensor networks, along with shielded cables and wires, are running a high risk of de-attaching from host structures. Moreover, with sensors directly exposed to the working environment, the capture of signals can be severely compromised by noise from a variety of sources. Therefore, the reliability and repeatability of signal acquisition may be inadequate.

Several studies implanted separated piezoelectric transducers into the composite structures to create *in-situ* sensor network. Su *et al.* [75] used an implanted piezoelectric network composed of miniaturized circuited wafers to locate and gauge delamination in CFRP laminates thanks to Lamb wave sensing, as shown in **Figure 2.8**. This technique shown excellent identification results combined to good robustness to environmental noise as well as stability and repeatability in data acquisition, when compared to *ex-situ* sensors methods. Masmoudi *et al.* [76-82] inserted PZT wafers of various dimensions inside composite laminates, to perform SHM of these materials using the PZTs as *in-situ* AE sensors during mechanical loading. The intrusiveness studies showed that the implanted PZTs caused only slight degradation of the composite’s mechanical properties if the PZT dimensions did not exceed certain limits. Chilles *et al.* [83] did it with a standard PZT transducer able to remotely send information to an external SHM acquisition unit thanks to a coil system using electromagnetic coupling. This inductively coupled transducer (ICT) system was used to perform GFRP laminates cure monitoring and damage detection thanks to bulk waves and guided waves generation and reception with a single *in-situ* ICT sensor performing pulse-echo measurements. Dziendzikowski *et al.* [84-86] used different kinds PZT wafers of implanted and surface-mounted transducers to perform a sensitivity comparison. The indication of damage was found in to be more significant for implanted sensors compared to surface-attached ones, with good stability and irrespective of PZTs relative orientation, network geometry or material anisotropy. Katunin *et al.* [87] also pointed out the fact of adding more sensors in the implanted network to enhance its accuracy in detecting impacts using damage indexes (DIs).

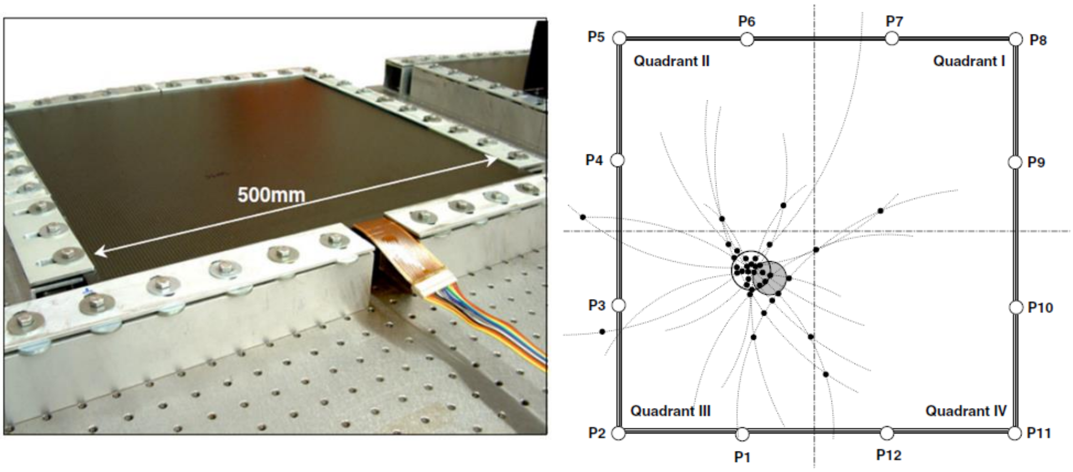

(a) **(b)**

Figure 2.8 (a) Set-up of CFRP laminate in test; (b) delamination searching strategy and results (grey circle: actual delamination; white circle: region of high probability for the occurrence of delamination).

Multiple layers can also be implanted inside the composite structures to create multiple sensing paths. Wang *et al.* [88] and Qing *et al.* [89] implanted SMART Layers in built-in-plane paths and through-the-thickness paths inside a multiple-layer thick ceramic-composite armour panel and a filament-wound bottle to be able to monitor impact damage, as shown in **Figure 2.9**. Qing *et al.* also noticed that the PZTs contained in the layers fully implanted in the bottle produced stronger diagnostic signals than the one only attached to its surface, which once again confirms the interest of fully *in-situ* sensor networks.

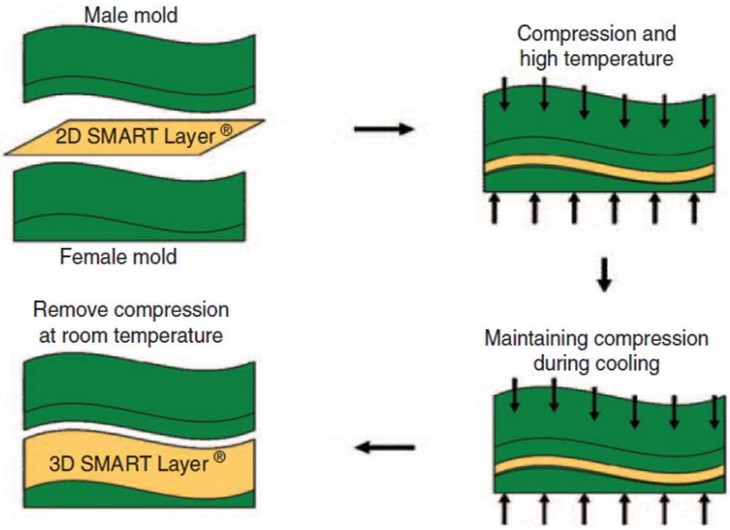

Figure 2.9 2-D to 3-D conversion process of a diagnostic SAMRT Layer.

Some researchers preferred using piezoelectric polymer film-type sensors to perform *in-situ* AE and SHM. De Rosa *et al.* [90] and Caneva *et al.* [91] worked on the integration of commercially available PVDF elements into glass/epoxy and aramid/epoxy composites to perform AE, and prove that these sensors can be used as *in-situ* low-cost, light, flexible and reliable SHM devices. Park *et al.* [92] did the same kind of calibration tests with two PVDF sensors implanted in GFRP laminates made with different hardeners, and also found a good correlation between generated and detected PLBs. Caneva *et al.* and Park *et al.* noticed that the PVDF had more difficulties to localize damage coming from long distances and attributed it to the low sensitivity of PVDF and damping of the viscoelastic matrix. Blanas *et al.* [93], Schulze *et al.* [94] and Bae *et al.* [95] implanted PVDFs into GFRP and CFRP laminates to realize *in-situ* impact detection thanks to the film detecting the propagation of the elastic wave generated by the impact.

2.5 Machine Learning Facilitated SHM

2.5.1 Basic Concept of ML

With demonstrated effectiveness in predictively modelling complexity and abstraction of engineering problems [96-98], ML has secured its popularity in data-driven SHM. Chief amongst the use of ML for SHM is the ANN [99, 100], with examples including localization of impact [98], construction of force history [99], assessment of delamination in composites [100]. Biologically inspired, an ANN is a computational model comprising a multitude of layers of computational units, known as artificial neurons, which are analogous to those of the neurons of a biological nervous system. An ANN predicts or forecasts new outputs, in response to new stimuli via probability-weighted associations that are obtained via training using a series of known input-output pairs. The validity of the ANN metamodels directly depend on the training process and the amount of data available. Sensor data should not be input as a discrete signal as it contains too much information and it requires extraction of specific features such as time of flight (ToF) of signals for impact detection on a plate, which is problem-dependant and cannot be generalized [101]. ANNs are generally accurate for the scope of a given training data, so for a real-life impact identification and characterization, a large range of training data is required [102]. Other ML algorithms that have been tested for simple applications including support vector machine (SVM) [101], extreme learning machine (ELM) [103, 104], probabilistic neural network (PNN) [105, 106], fuzzy ARTMAP network (FAN) [107-109], least square support vector machine (LSSVM) [101]. However, all these methods can be applied for relatively-simple structures only and lack of generalization.

To overcome a common problem that the ANN and other prevailing ML algorithms confront – the drastic decrease in computational efficiency as the quantity of data for training increases, the matrix convolution operation is introduced, in which only key features of inputs are extracted for the training – known as CNN [110]. CNN has proven capability of exploring complex non-linear mappings between inputs and outputs – a daunting task to conventional ANN [111-117]. CNN has found its superior niches in ML-facilitated image classification [118], object recognition [119], speech recognition [120], semantic segmentation [121], medical studies [122], computer vision [123], and damage diagnosis [124] to name a few. Abdeljaber *et al.* [125] proposed a new, real-time vibration-based structural damage detection system based on one-dimension (1-D) CNN. One of the main advantages of this method is that raw signals are used for the optimal damage-sensitive feature extraction. Further study [126] emphasized how CNNs can fuse and simultaneously optimise feature extraction and classification into a single task: a learning block in the training phase of the CNN, such that it eliminates the need of feature extraction beforehand. Thus, using a CNN with raw data as input will be more advantageous than traditional extraction methods. De Oliveira *et al.* [127] developed a CNN-based SHM technique for an aluminium specimen for damage detection. Moreover, the rotating machinery domain features other studies using CNNs such as [128], that uses images with the actual damage as training data [129-133], which emphasize that traditional methods ignore abundant information from the signals when extracting only a few features, such as mean value, standard deviation and kurtosis.

As will be readily seen, when extended to SHM and damage identification, the accuracy and effectiveness of CNN, as well as other prevailing ML algorithms, depend substantially on a multitude of factors including mainly the training algorithms adopted, completeness of data available for training, and compatibility of a trained database to new inputs which are not included in the training. These factors, by nature, may narrow the application spectrum of ML-driven SHM. The significance of enhancing the compatibility and applicability of a trained database, with minimal extra effort to re-train an CNN, cannot be overemphasized. What is more, most of the reported work with CNN have been on simple structure with isotropic properties and the scalability of the method on real structures under operational load have not been demonstrated.

2.5.2 Fundamentals of CNN

Although there are many variations in the CNN, the main composition of the architecture includes convolution layers, pooling layers and full connection layers [134-148]. The convolution layer is the core of the CNN. It is used for extracting information from its input using a number of filters that are automatically learned to detect certain features in an image. Each filter will scan through the input from the upper left hand side corner to the bottom right hand side corner, each creating a feature map. As more convolutional layers are connected in series the output of one such layer becomes the input of another, and its features are extracted again increasing the level of complexity, and hence the accuracy, but also increasing the training time and the risk of overfitting. Thus, there is a trade-off, and the number of convolution layers, as well as the number of filters and their sizes in the metamodel, are chosen by performing the trial-and-error method.

The pooling layer performs the down-sampling in the width and height, reducing the dimensions of its input and, hence, reducing the number of parameters to be computed [30]. This reduces the complexity of the network and the possibility of overfitting. The pooling operation operates on each depth slice of the input separately, down-sampling them all in the same manner. Each of the slices will be divided into several patches, equal in area to the filter size set by the user when defining the pooling layer. The most used filter size is (2, 2), so each slice can be divided into several adjacent but disjoint patches of two neurons high and two neurons long. The output of the pooling layer is a smaller volume, but equal in depth to the input.

The full connection layer is a regular densely connected layer. Each of its output neurons is connected to all the neurons from the input [30]. This is implemented at the output together with an activation function to give the predictions. The nodes at the output of the layer contain the probabilities of the input to the CNN belonging to all classes. As each of those nodes is connected to all the neurons of the input to the layer, each receives all the information from the first half of the network, containing the convolutional and pooling layers.

In addition to the above layers, activation function is also a key part in CNN. The main purpose of activation function is to introduce nonlinearity in the relationship between the output of a node and the input of another node [149]. There are multiple types of activation function, and the main ones are described as follows:

(i) Sigmoid function: The curve has an ‘S’ shape as shown in **Figure 2.10**, and it is given by the following equation [150]

$$sig(x) = \frac{1}{1+e^{-x}} \tag{2.12}$$

Since the function is not centred on the origin but on the (0, 0.5) point, as well as the limited region of high sensitivity, when using Sigmoid function, the learning algorithms have difficulties in updating the weights to improve the performance causing a difficult process of optimisation and a slow convergence. In addition, as the output varies between 0 and 1, if a large input is applied, it will be scaled down significantly. Therefore, a large change in the input will result in a small change in the output. This problem is called the vanishing gradient, and it can be problematic when using multiple layers in the network.

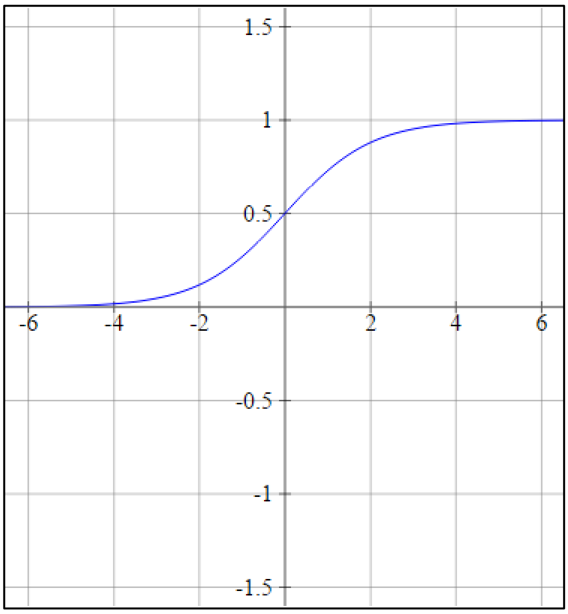

Figure 2.10 Illustration of Sigmoid activation function.

(ii) Tanh function: The hyperbolic tangent function is a slightly improved version of the Sigmoid function, in which the activation function is centred on the origin. The function has an ‘S’ shape, as shown in **Figure 2.11**, and saturate at -1 for $x = -\infty$, and 1 for $x = \infty$ [151]

$$tanh(x) = \frac{2}{1+e^{-2x}} - 1 \tag{2.13}$$

Using the Tanh function, the optimisation can be easier compared with the Sigmoid function. However, the output still saturates, the high sensitivity region is still small, and the vanishing gradient is still a critical problem.

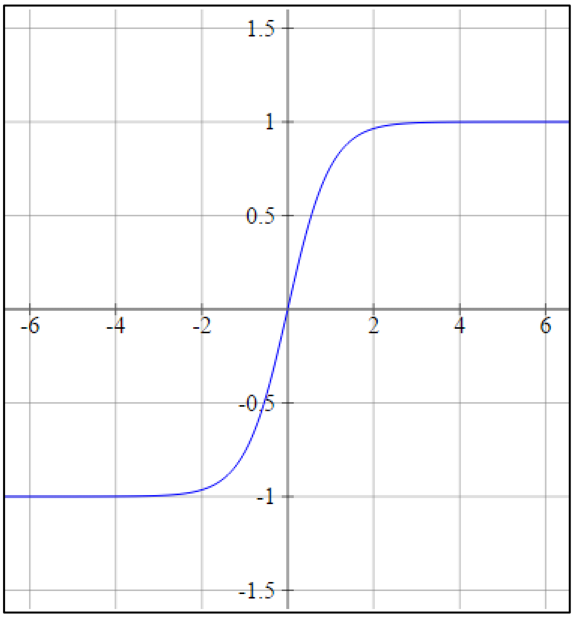

Figure 2.11 Illustration of Tanh activation function.

(iii) ReLU function (Rectified Linear Unit): the function curve has two regions, as shown in **Figure 2.12**, depending on the value of the input. For negative inputs, the function output is 0, while for positive inputs, the result is equal to the input itself [152]

$$\mathrm{ReLU} = \begin{cases} 0, x < 0 \\ x, x \geq 0 \end{cases} = max(0, x) \tag{2.14}$$

The ReLU function has numerous advantages when comparing with the Sigmoid or the Tanh functions. Firstly, it was proven to be approximately six times faster in convergence comparing to the hyperbolic tangent. Secondly, as the function increases from 0 to ∞ for positive inputs, a large variation in the input will be translated to a large variation in the outputs so the vanishing gradient problem is avoided. The function is no longer saturated and have one non-linear region (*i.e.*, for $x<0$) and one linear region (*i.e.*, for $x\geq0$), but overall it is still a non-linear function. Nevertheless, when using backpropagation for training the network, the linear region will bring many desirable advantages of linear activation functions. It is computationally easier performed than the previous two activation functions.

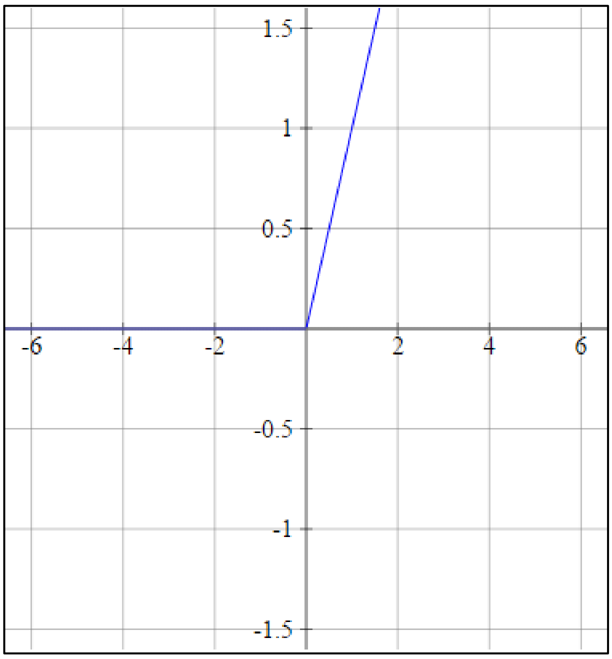

Figure 2.12 Illustration of ReLU activation function.

(iv) Softmax function: the function is used to normalise the output vector of the CNN to a vector of length *K*, whose values sum to 1. This final vector contains a range of probabilities, and the position of the maximum one can be the predicted. The

Softmax function can be mathematically written as [30]

$$f\left(x\right)=\frac{e^{xj}}{\sum_{k=1}^{K}e^{xk}} \tag{2.15}$$

2.6 Summary

In this chapter, the basic concept of guided ultrasonic wave-based SHM is introduced, and the theoretical fundamentals of guided ultrasonic waves are briefly summarized. Among the existing SHM approaches, passive SHM is mainly used to measure the real-time parameters and then deduce the status of structural health by using specific algorithms, while active SHM utilizes actively generated GUWs of specific frequency and magnitudes to monitoring structural integrities. As the popularity and demonstrated effectiveness of UT in active SHM, several practical tomographic imaging approaches are presented and compared. However, conventional UT by virtue of imaging algorithms often shows inferior accuracy when insufficient sensors are used. Central to the realization of UT-based SHM is extracting structural health information from acquired wave signals, thus ultrasound sensors play the irreplaceable yet paramount role in an SHM system. Various categories of sensors for this purpose are surveyed and summarized, including nanocomposite-inspired sensors and implanted sensors. Finally, considering the superior capability of ML in improving the sensing effectiveness of UT, recent studies on ML-facilitated SHM are reviewed, including the application of ANN and CNN. At the same time, the theoretical fundamentals of CNN are briefly summarized according to the categories of network architectures and activation functions. As will be readily seen, when extended to SHM and damage identification, the accuracy and effectiveness of CNN, as well as other prevailing ML algorithms, depend substantially on a multitude of factors including mainly the training algorithms adopted, completeness of data available for training, and compatibility of a trained database to new inputs which are not included in the training. These factors, by nature, may narrow the application spectrum of ML-driven SHM. In conclusion, this PhD thesis will start from the design and fabrication of an implantable, nanocomposite-inspired sensor network, through the improvement of RAPID imaging to ML-enabled imaging, to truly implement *in-situ* UT-based SHM.

CHAPTER 3

Fabrication of Implantable Piezoresistive Sensor Network

3.1 Introduction

In this chapter, a new breed of nanocomposite-inspired, piezoresistive sensor network is developed using a spray deposition process. Individual sensors, deposited on a pre-treated B-stage epoxy film, are networked via highly conductive carbon nanotube fibres as wires, to form a dense sensor network. Flexible, light, sensitive to broadband dynamic signals, the sensor network is implanted into CFRP laminates, to fulfil GUWs-based UT. Morphological characterization is performed to observe the interface between the CFRP laminate and implanted sensing unit, meanwhile to investigate the intrusion of the implanted sensor network to the host composites. Quasi-static tensile test is performed to gauge possible degradation in tensile properties and change in failure modes of the CFRP laminates owing to the implantation of a sensor network.

3.2 Pre-curing of B-staged Epoxy Film

For fabricating a compatible, implantable sensing unit with minimized intrusion to the host composites, a B-staged epoxy is pre-cured for depositing sensing units and unit-associated wires/circuits, and in the meantime insulating sensing units from conductive fibres in CFRPs. A high temperature-resistant release film (AIRTECH® WL5200B nonperforated peel ply) is selected as the substrate, onto which the B-staged epoxy is deposited. The release film is immersed in acetone and sonicated in an ultrasonic bath (Branson® 5800 Ultrasonic Cleaner, 40 kHz) for 30 min to remove contaminants, and is heated at 65 °C in a vacuum oven for 15 min to evaporate the residual acetone. The B-staged epoxy is poured on one end of the release film and then evenly squeezed to the other end of the film using an applicator at 80 °C. The thickness of the coated B-staged epoxy is ~20 μm, measured using an electronic spiral micrometre. Up to this stage, the B-staged epoxy on the film is still chemically reactive. To reduce the resin flowability and maintain a desired morphology of the spray-coated sensing units, the epoxy film is pre-cured in a vacuum environment at 130 °C to achieve 40 % of the full degree of curing. **Figure 3.1** illustrates the main process of fabricating precured B-staged epoxy films.

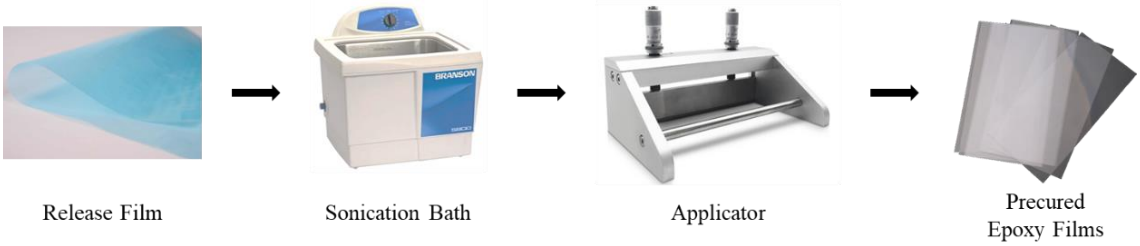

Figure 3.1 Schematic diagram of fabricating precured B-staged epoxy films

3.3 Fabrication of Spray-coated Nanocomposite Sensing Units

A standard solution mixing process is applied to prepare nanocomposite ink. PVP (Sigma-Aldrich® PVP K-30) is chosen as the matrix, and GNSs (TANFENG®, thickness: ~1 nm, diameter: ~50 μm, SSA: ~1200 m^2/g, and purity: > 99 wt.%) as the modified nanofillers (mass ratio of GNSs to PVP is 1:19). The GNS/PVP hybrid (1 g) is dispersed in ethanol (20 ml), and magnetically stirred at 500 rpm at an ambient temperature (25 °C) for two hours, followed with a sonication in the ultrasonic bath for one hour. Thus-produced nanocomposite ink is sprayed directly onto the above prepared pre-cured epoxy film using an airbrush (HD-130). The scanning speed of the nozzle (5 cm/s), stream pressure (0.35 MPa) and distance of target to nozzle (10 cm) are precisely controlled during the spraying process, to warrant a consistent initial resistance of the ink. During deposition, the B-staged epoxy is adhesive, in which a small amount of ethanol remains, and the morphology of the ink tends to be affected by the residual ethanol in the subsequent procedure of heating treatment. To eliminate such effect, the ink deposited on the pre-cured epoxy film is placed in a frozen drying oven to vaporize the residual ethanol.

During the spraying process, a thin polyimide (PI) film with a desired hollowed-out is prepared, serving as a moulding layer. The film is pressed onto the pre-cured epoxy film. The hollowed-out precisely defines the geometry of a sensing unit, to be 5 mm in width and 20 mm in length, after the nanocomposite ink is sprayed on the PI film and then the moulding layer is peeled off from the pre-cured epoxy film. A pair of electrodes is introduced to each sensing unit, by aligning two CNT-fibres

(DexMat® CNT-film) along the two long edges of a unit. Another identical pre-cured B-staged epoxy film is placed atop each sensing unit which has been deposited on the substrate, whereby to encapsulate each sensing unit and insulated it from conductive fibres upon implantation into CFRPs. Each encapsulated sensing unit is fully cured at 130 °C for 30 min under a vacuum condition. With such a manufacturing approach, the thickness of each sensing unit is ~45 μm only, measured in scanning electron microscope (SEM) images, inflicting minimal intrusion to the host composites. The manufacturing procedure of preparing the nanocomposite sensing units is flowcharted in **Figure 3.2**, and thus-fabricated sensing units with CNT-fibre-based electrodes and wires are photographed in **Figure 3.3**. With a resistance of ~20 Ω/m only, the CNT-fibres also function as wires to network individual sensing units. The wire is ~1 mm in width and ~10 μm in thickness only, impacting ignorable intrusion to the composites.

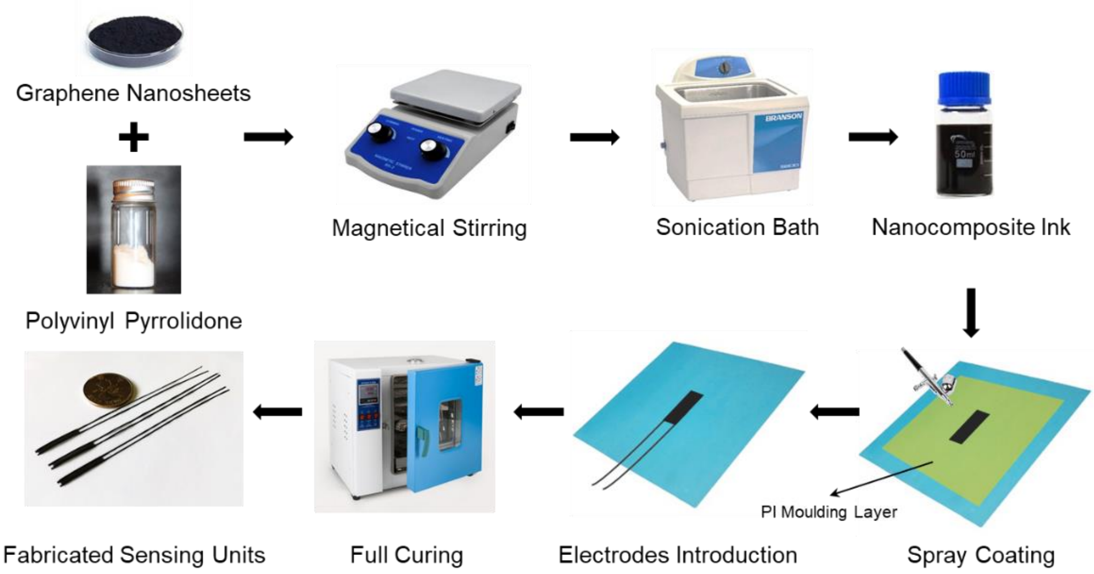

Figure 3.2 Flowchart of fabricating the spray-coated nanocomposite sensing units.

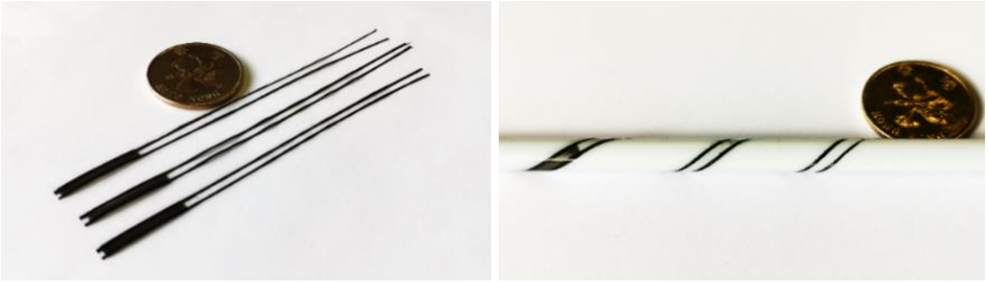
(a) (b)

Figure 3.3 Photographs of (a) fabricated nanocomposite sensing units; (b) sensing unit showing a high degree of flexibility (diameter of the plastic rod in photo: 8 mm).

3.4 Implantation of Sensor Network into CFRP Laminates

A series of quasi-isotropic CFRP laminates (500 × 500 × 1.15 mm^3) is prepared in accordance with a standard autoclaving procedure. Each laminate is of 8-layer unidirectional prepregs (T300, Torayca®) with the stacking sequence of [0°/90°/45°/-45°]$_S$. For proof-of-concept validation, 16 sensing units are networked with CNT-fibre-based wires to form a sensor network, which is then implanted between the 4th and 5th layers of each laminate during autoclaving, as illustrated schematically in **Figure 3.4**. The autoclave mould is heated at a rate of 1.5 °C /min from an ambient temperature to 80 °C, followed with a post-curing at 130 °C for another one hour. The curing pressure remains at 160 psi. The strong adhesion of prepreg and the high pressure of autoclaving ensure accurate position of each sensing unit in the CFRP laminate during fabrication. Upon full curing, the nominal thickness of each laminate measures ~1.15 mm. Each laminate is trimmed using a water jet cutter (OMAX® PROTOMAX).

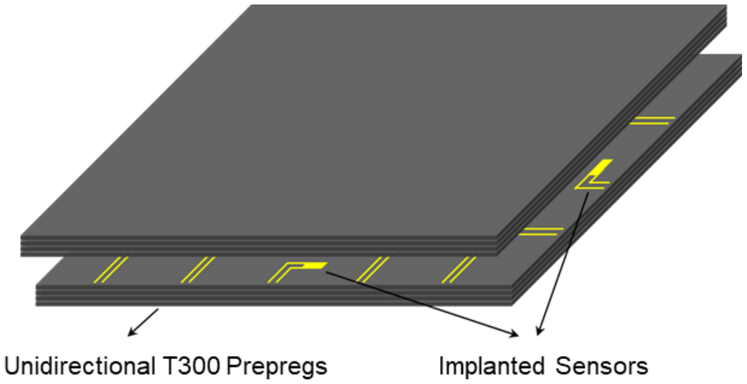

Figure 3.4 Schematic illustration of a CFRP laminate with an implanted sensor network comprising nanocomposite sensing units.

3.5 Morphological Characterization and Mechanical Properties

Morphological characterization of the spray-coated sensing units is performed using SEM (TESCAN® Vega 3), to observe good homogeneity, **Figures 3.5(a)** and **(b)**, in which the GNS aggregates are observed to distribute in PVP densely and evenly. Such a trait is conducive to the creation of a uniform conductive network in the sensing unit. **Figures 3.5(c)** and **(d)** show the intersection of the CFRP laminate with an implanted sensing unit (cross-section view), to reveal that the interface between the CFRP laminate and implanted sensing unit is indistinguishable, implying an ignorable intrusion of the implanted sensor network to the host composites.

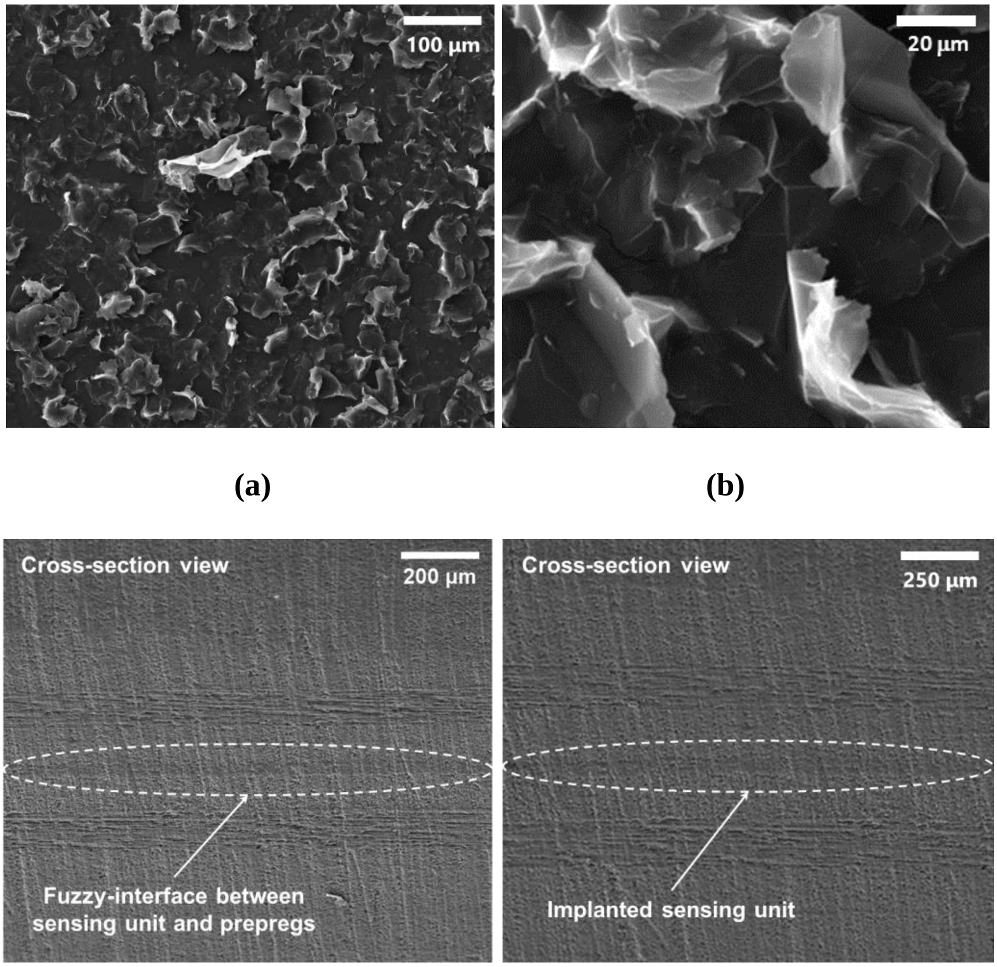

(a) (b)

(c) (d)

Figure 3.5 SEM images of (a, b) spray-coated nanocomposites showing densely and evenly distributed GNSs in PVP, in two different scales; (c, d) intersecting surface of CFRP laminate with an implanted sensing unit showing ignorable intrusion of the sensing unit to the host composites.

Quasi-static tensile test, in accordance with ASTM D3039 [153], is performed to gauge possible degradation in tensile properties and change in failure modes of the CFRP laminates owing to the implantation of a sensor network. To this end, two types of CFRP laminates are fabricated with and without an implanted sensing unit, each measuring 250 × 25 × 1.15 mm^3. Both laminates are adhered with two aluminium end tabs before test to avoid premature failure around the gripping device

(Scotch-Weld® 2216 Epoxy Adhesive). Laminates are pulled at a constant crosshead speed of 2 mm/min on a universal testing system (INSTRON® 5982) until the fracture, during which strain is recorded using an advanced video extensometer (AVE). **Figure 3.6** represents the tensile testing results of the two types of laminates, to note no measurable difference in between. The averaged tensile moduli of the two types of laminates are 45.86 GPa and 44.80 GPa, respectively, implying a slight decrease of ~2.31% only, due to the implantation of the sensing unit. The slight variation in failure tensile stress/strain between laminates with and without an implanted sensing unit is attributed to the discrepancy in specimen preparation and tests.

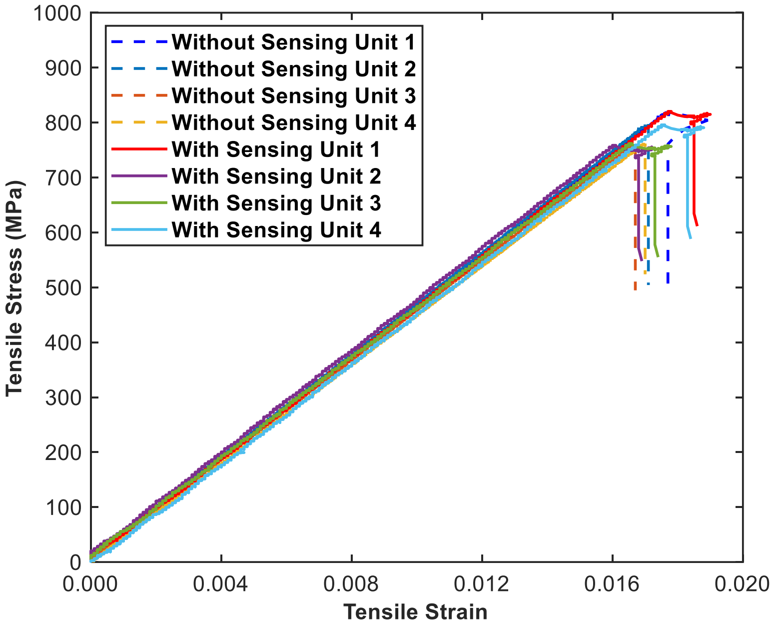

Figure 3.6 Tensile strain-stress relation of CFRP laminates with and without an implanted sensing unit.

3.6 Summary

In this chapter, an implantable, nanocomposite-inspired, piezoresistive sensor network is developed for implementing UT-based SHM of CFRP laminates. The nanocomposite ink, formulated with GNSs and PVP, is tailored to acquire the percolation threshold of conductive nanofillers. The above ink is then deposited on partially precured B-stage epoxy films using spray deposition process and circuited via highly conductive CNT-fibres as wires, to form a dense sensor network, which is then implanted into CFRP laminates during autoclaving procedure. With a morphologically optimized nano-architecture in nanocomposites, the quantum tunnelling effect can be triggered in percolated networks, which enables the sensors to faithfully response from quasi-static loads to high-frequency GUWs. Quasi-static tensile test is performed to gauge possible degradation in tensile properties and change in failure modes of the CFRP laminates owing to the implantation of a sensor network.

CHAPTER 4

UT Imaging for Composites Using Enhanced RAPID Algorithm

4.1 Introduction

In this chapter, using the developed implantable sensing units, a dense sensor network can be configured, to circumvent the *limited-angle problem* that conventional UT-based imaging algorithms may have. Especially for the conventional RAPID algorithm, the selection of a constant parameter β is inadequate to warrant accurate depiction of defect when the defect is at an arbitrary position within the inspection region. By introducing the continuously iterated and updated scaling parameter β, the RAPID-based imaging algorithm is enhanced to facilitate processing of inadequate signals rendered by the sensor network, resulting in not only the improved accuracy of defect localization, but also the enhanced geometrical depiction and severity estimate of defect. Experiment is conducted to demonstrate fidelity of acquired GUW signals, showing no remarkable discrepancy in sensing performance between the developed implantable sensor network over a broad frequency range, and examine accuracy of the enhanced RAPID algorithm.

4.2 Enhanced RAPID Imaging

Conventional UT by virtue of imaging algorithms including FBP, ART, FWI and RAPID often shows inferior accuracy when insufficient sensors are used, due to the narrow scanning angle and inadequate number of sensing path available in the sensor network, during tomographic image reconstruction – a deficiency referred to as *limited-angle problem* [12]. The limited-angle scanning can make signal acquisition incomplete, potentially leading to ignorance of damage in certain areas within the inspection region. To warrant a broad scanning angle and sufficient sensing paths, sensors have to be configured in a dense manner. Using the developed implantable sensing units, in conjunction with the use of only a handful of surface-mounted PZT wafers as excitation sources, a dense transducer network can be configured, to circumvent the *limited-angle problem* that conventional UT-based imaging algorithms may have.

In addition, aimed at precisely estimating the geometrical features and severity of defect (*e.g.*, uneven resin during curing, or impact-induced delamination), conventional RAPID algorithm is revamped here, in which the probability of a defect presence at a pixel within the inspection region is calibrated, in terms of (i) the severity of defect-induced change in signals captured by different sensing paths, and (ii) the relative position of the defect with regard to all sensing paths in the transducer network. To quantify defect-induced change in signals, signal difference coefficient (SDC) – a GUW feature, is defined for tomographic imaging. SDC is statistical difference in signals between the current status and the reference status, which reads

$$\mathrm{SDC} = 1 - (\mathrm{Cov}(X,Y)/\sigma_X\sigma_Y)\,, \tag{4.1}$$

where Cov(X, Y) signifies the covariance of the reference signal X and the current signal Y, given by

$$\mathrm{Cov}(X,Y) = \sum_{k=1}^{K}(X_k - \mu_X)(Y_k - \mu_Y)\,, \tag{4.2}$$

$$\sigma_X\sigma_Y = \sqrt{\sum_{k=1}^{K}(X_k - \mu_X)^2}\sqrt{\sum_{k=1}^{K}(Y_k - \mu_Y)^2}\,, \tag{4.3}$$

where X_k and Y_k (k=1, 2, …, K) are discretized forms of X and Y, each with K discretized data; μ_X and μ_Y are the mathematical expectation of X and Y. The defect distribution probability, $P(x, y)$, can be defined as a linear summation of SDC calculated by all sensing paths rendered by the transducer network with a total of M actuators and N sensors, as

$$P(x,y) = \sum_{i=1}^{M}\sum_{j=1}^{N}P_{ij}(x,y) = \sum_{i=1}^{M}\sum_{j=1}^{N}\mathrm{SDC}_{ij}w_{ij}(x,y)\,, \tag{4.4}$$

where (x, y) is the coordinate of an arbitrary point within the inspection region; $P_{ij}(x, y)$ denotes the probability of defect occurrence at (x, y) that is estimated by the sensing path linked by actuator i (located at (x_i, y_i)) and sensor j (located at (x_j, y_j)); SDC_{ij} is the SDC value calculated by that sensing path; $w_{ij}(x, y)$ signifies the weighted matrix related to the spatial distribution of the defect, and it, for the sensing path i-j, is defined as

$$w_{ij}(x,y) = (\beta - R_{ij}(x,y)) / (\beta - 1), \tag{4.5}$$

$$R_{ij}(x,y) = (l_{(x,y)\to(x_i,y_i)} + l_{(x,y)\to(x_j,y_j)}) / l_{(x_i,y_i)\to(x_j,y_j)}, \tag{4.6}$$

where l is the distance between the two points indicated in subscript; β is a scaling parameter which controls the size of the effective elliptical distribution area, and the amplitude of which tapers from its maximum value along the line connecting the two ellipse foci to zero on the periphery of the ellipse [154], as illustrated in **Figure 4.1**.

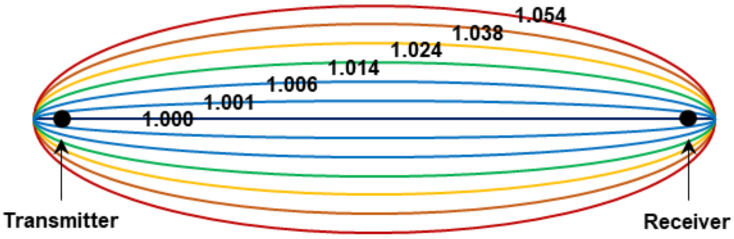

Figure 4.1 Illustration of the elliptical distribution area of the RAPID algorithm.

Provided that an unreasonably small value of β is selected, artifacts can be introduced in the reconstructed image; in the contrast, imaging resolution degrades if β is unjustly large. In prevailing RAPID algorithms, the scaling parameter β is usually selected as the consistent of 1.05, with the assumption that the distances from the defect to all the sensing units are the same – that, however, is not the case in reality. It is therefore that the selection of a constant parameter β is inadequate to warrant accurate depiction of defect when the defect is at an arbitrary position within the inspection region.

In this enhanced RAPID imaging algorithm, based on the principle of iteration, the scaling parameter β and the defect distribution probability $P(x, y)$ is continuously iterated and updated, using every single sensing path in the transducer network, after initial calculation of the approximate defect location using **Equations 4.1 – 4.6**, as

$$\beta^{n+1} = R_{ij}(x_d^n, y_d^n) = (l_{(x_i,y_i)\to(x_d^n,y_d^n)} + l_{(x_j,y_j)\to(x_d^n,y_d^n)}) / l_{(x_i,y_i)\to(x_j,y_j)}\,, \tag{4.7}$$

$$P^{n+1}(x,y) = \sum_{i=1}^{M}\sum_{j=1}^{N} P_{ij}^{n+1}(x,y) = \sum_{i=1}^{M}\sum_{j=1}^{N} \mathrm{SDC}_{ij}\, w_{ij}^{n+1}(x,y)\,, \tag{4.8}$$

where (x_d^0, y_d^0) is the coordinate of the defect as initially estimated by **Equations 4.1 – 4.6**, and (x_d^n, y_d^n) the coordinate of the updated location after n iterations. In each iteration, β and P_{ij} (x, y) for a sensing path is updated in accordance with the defect location determined by previous paths. It can be derived from **Equation 4.8** that if the distance of the defect to all sensing paths is identical, the values of the scaling parameter β are a constant; otherwise the values can be various based on the distances. Continuous updating β and $P(x, y)$ not only improves the accuracy of defect localization, but also enhances the geometrical depiction and severity estimate of the defect.

4.3 Acquisition of GUWs Using Implanted Sensor Network

To experimentally examine the fidelity of the spray-coated sensing units for perceiving GUW signals in a broadband frequency regime, two CFRP laminates are prepared, with the identical configuration as that of the laminates detailed in Chapter 3.4. Four PZT wafers (labelled as P1 – P4) (PSN-33, Ø 12 mm, 1 mm thick) – used as wave actuators – are surface-mounted on each CFRP laminate, see **Figure 4.2**. One of the two CFRP laminates is pre-implanted with a sensor network comprising 16 nanocomposite sensing units (denoted by S1 – S16) between the 4th and 5th layers which are arranged in circular fashion – used as the wave receivers; and the other laminate is pre-implanted with a PZT wafer (PSN-33, Ø 12 mm, 1 mm thick) between the 4th and 5th layers as a benchmark laminate, for comparison and calibration.

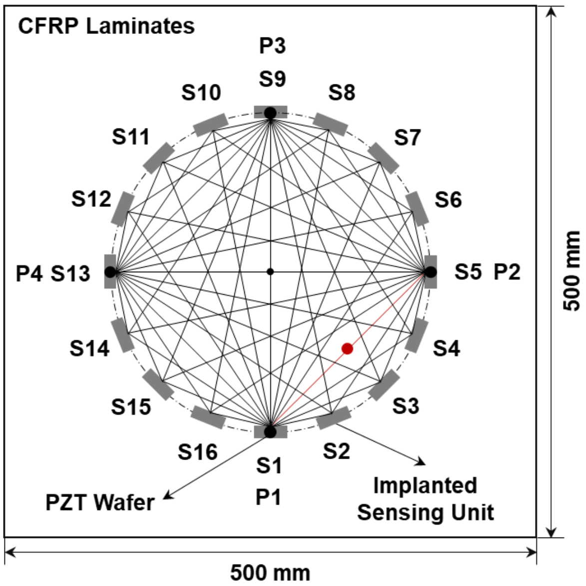

Figure 4.2 Dimensional sketch of the CFRP laminate with an implanted sensor network. (black dot: PZT wafer as wave actuator; grey rectangular: implanted sensing unit)

The experimental set-up is shown in **Figure 4.3**. In the set-up, the signal generation module consists of an arbitrary waveform generator on NI® PXIe-1071 platform, and a linear power amplifier (Ciprian® US-TXP-3); the data acquisition module includes a self-developed amplification unit for mitigating ambient noise, a resistor-adjustable Wheatstone bridge converting piezoresistive variation to electrical signals, and an oscilloscope (Agilent® DSO 9064A). Four PZT wafers are connected with the signal generation module, while the implanted sensor network and the implanted PZT wafer are respectively linked to the data acquisition module.

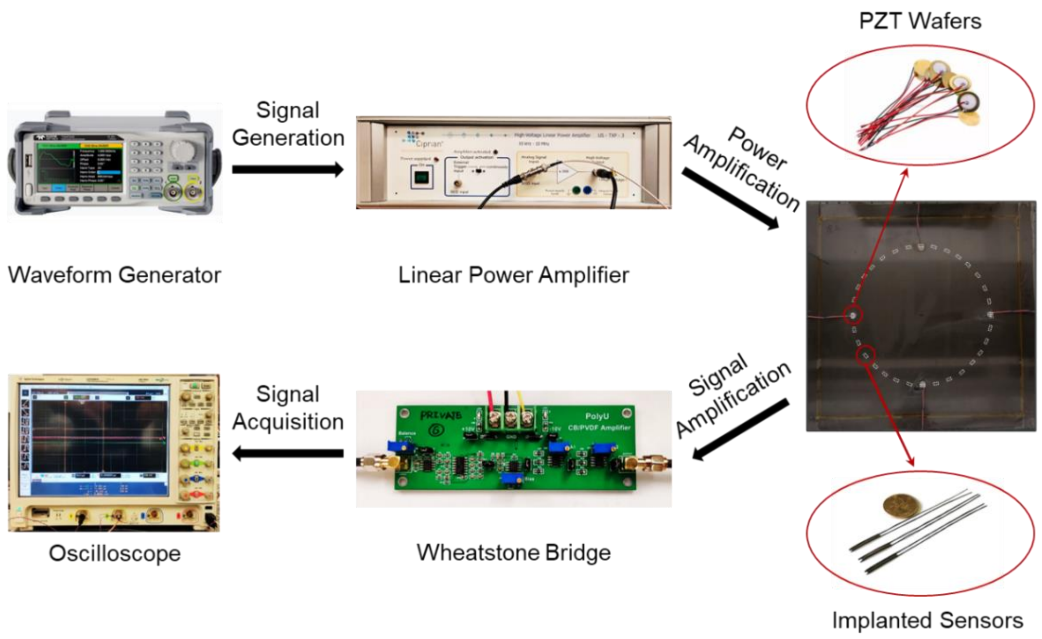

Figure 4.3 Experimental set-up for *in-situ* generation and acquisition of GUWs.

A series of five-cycle Hanning-function-modulated sinusoidal tonebursts with the central frequency varying from 150 kHz to 450 kHz (with an increment of 25 kHz) is generated with the arbitrary waveform generator, and applied on each PZT wafer in turn via the power amplifier, to emit GUWs into CFRP laminates. The modulated excitation provides concentrated energy in a narrowed frequency band, efficiently reducing wave dispersion and benefiting signal interpretation. **Figure 4.4** compares the signals, generated by P1 at 175 kHz, captured by S5 (*i.e.*, the sensing path P1 – S5), against the counterpart signal captured by the implanted PZT wafer in the benchmark laminate. Captured signals are processed with a first-order Butterworth filter to eliminate measurement noise. The first-arriving wave component (*i.e.*, the zeroth-order symmetric Lamb wave mode, denoted by S_0 in what follows) is clearly observed in both signals, showing quantitative agreement in terms of the arrival time and signal waveform. Not only the S_0 mode but also the zeroth-order anti-symmetric Lamb wave mode (denoted by A_0) is faithfully captured by the sensing units.

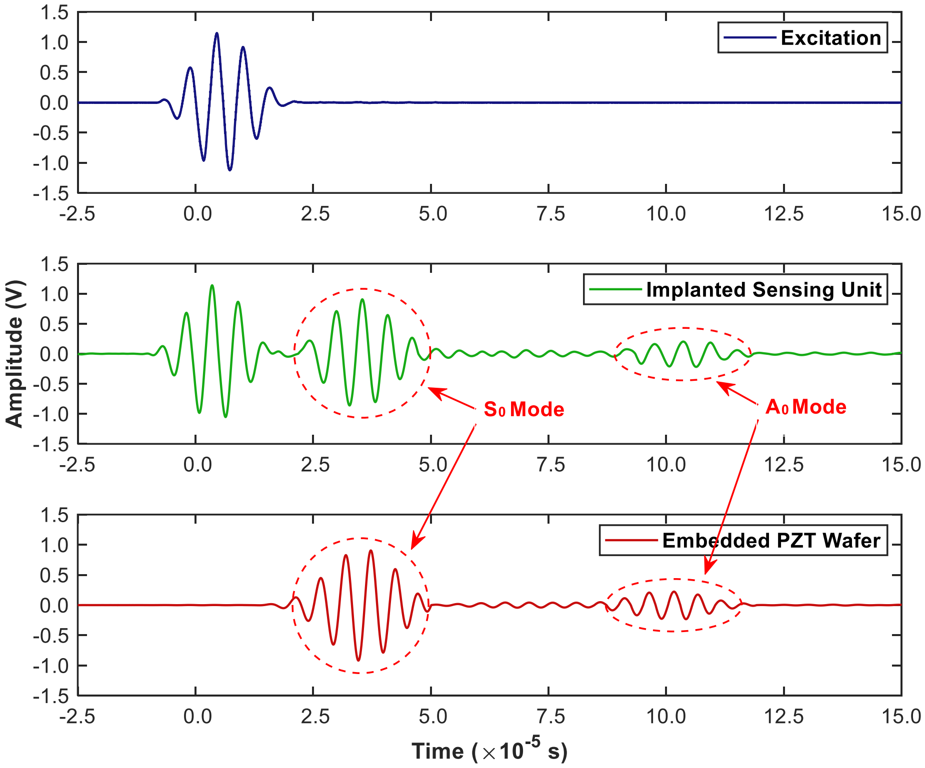

Figure 4.4 GUWs signals respectively captured by the implanted sensing unit and implanted PZT wafer along sensing path P1 – S5 at 175 kHz.

Figure 4.5 comparatively presents the signals captured by the same sensing path (P1 – S5) at 150, 175, 200, 225, and 250 kHz, respectively, arguing that the magnitudes of both the S_0 and A_0 modes are dependent on the excitation frequency. The maximum magnitudes of both wave modes are recorded at 175 kHz, as at this frequency the PZT wave actuator resonates.

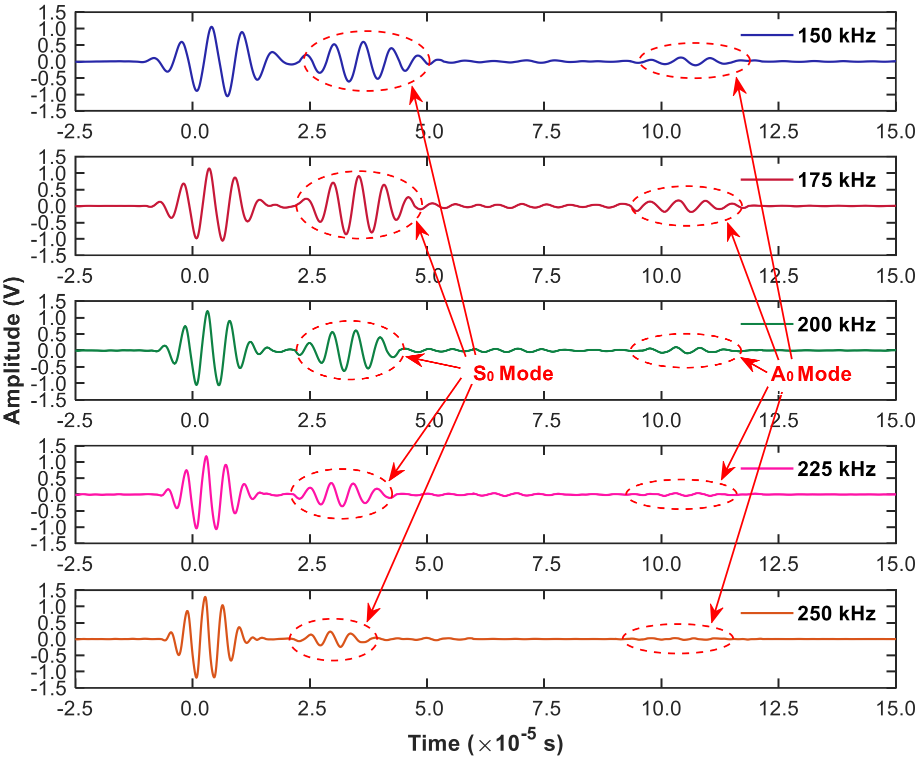

Figure 4.5 GUWs signals respectively captured by the implanted sensing unit along sensing path P1 – S5 at 150, 175, 200, 225, and 250 kHz.

Sweeping the excitation frequency from 150 to 450 kHz, **Figure 4.6** shows the spectrum of signals captured via P1 – S5, compared with the counterpart spectrum obtained by the implanted PZT wafer, to observe no remarkable discrepancy in sensing performance between these two types of sensor over a broad frequency range.

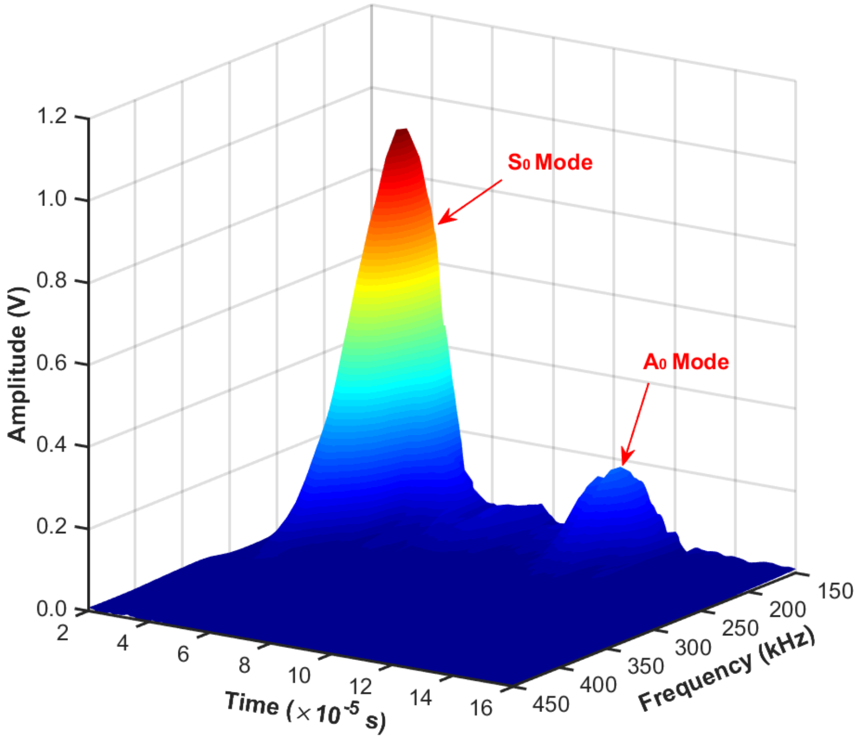

(a)

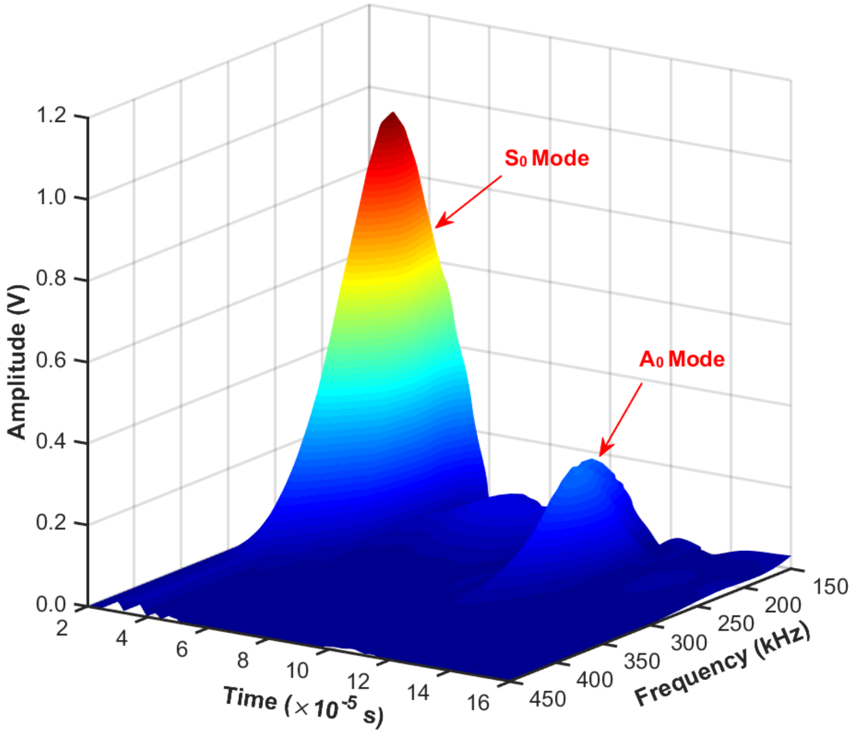

(b)

Figure 4.6 Spectra of signals under sweep frequency excitation for (a) the implanted sensing unit; (b) the implanted PZT wafer (captured along sensing path P1 – S5).

To further examine the sensitivity of the nanocomposite sensing unit when it is internally implanted in or surface-mounted on CFRP composites, an additional sensing unit is mounted atop the benchmark laminate. **Figure 4.7** displays the signals captured by the implanted and surface-mounted sensing units, respectively, showing good accordance in between. Note that the crosstalk included in signals at the commencement of excitation is generated by the high-voltage power amplifier, which, however, does not interfere with signal interpretation.

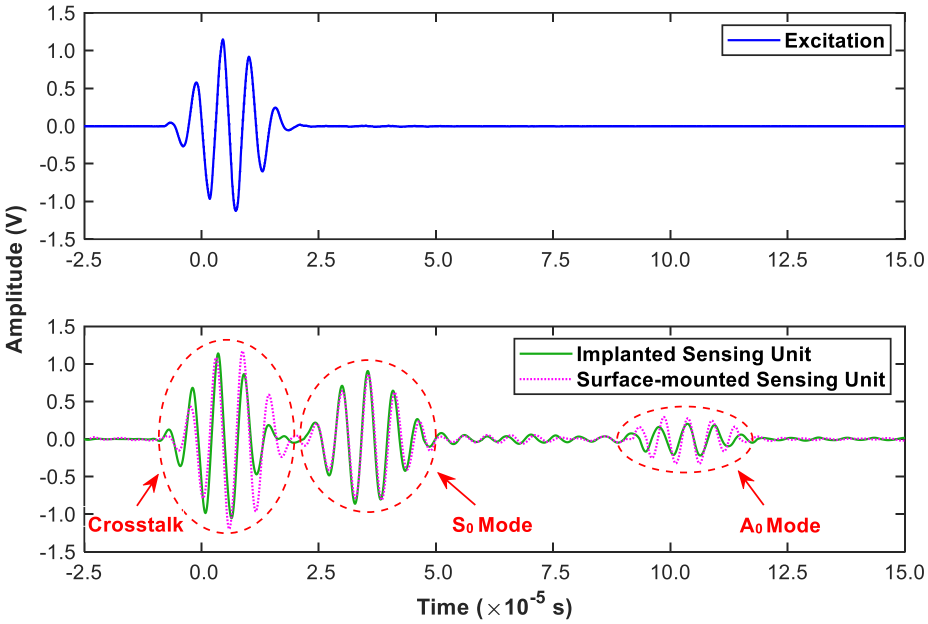

Figure 4.7 GUWs signals respectively captured by the implanted and surface-mounted sensing units along sensing path P1 – S5 at 175 kHz.

4.4 Proof-of-Concept: Anomaly Imaging

A steel cylinder (diameter: 20 mm, mass: 200 g) is surface-coupled with the above CFRP with the implanted sensor network using glycerol as a coupling agent, as artificial anomaly. Note the CFRP laminate before the introduction of the artificial anomaly is used as the reference condition for imaging. In view of the transducer network configuration (four PZT wafers as actuators and 16 nanocomposite sensing units as receivers, in **Figure 4.2**), a total of 60 sensing paths are technically available. As a typical signal for illustration, **Figure 4.8** compares the signals generated by P1 at 175 kHz and captured by S5, before and after the anomaly is introduced. Using **Equation 4.1**, SDC values for all the sensing paths are calculated and presented in **Figure 4.8**. The SDC value for the sensing path P1 – S5, which reads 0.0328, is higher than those for other sensing paths in which P1 serves as the actuator, **Figure 4.8(a)**, implying higher possibility of defect presence along P1 – S5. Similarly, higher SDC values are also observed for P2 – S1, P3 – S3 and P4 – S3, in **Figures 4.8(b)**, **(c)** and **(d)**, respectively. With calculated SDC values throughout the entire transducer network, the tomographic images are constructed using the conventional and enhanced RAPID algorithms (**Equations 4.4 – 4.8**), respectively, in **Figure 4.9**. It is apparent that there is no remarkable difference in the accuracy of anomaly positioning for two algorithms, while the enhanced RAPID algorithm using the iteratively updated scaling parameter β based on **Equation 4.7** shows superior accuracy when evaluating the shape of the anomaly, compared with the conventional algorithm which forces β as a constant of 1.05.

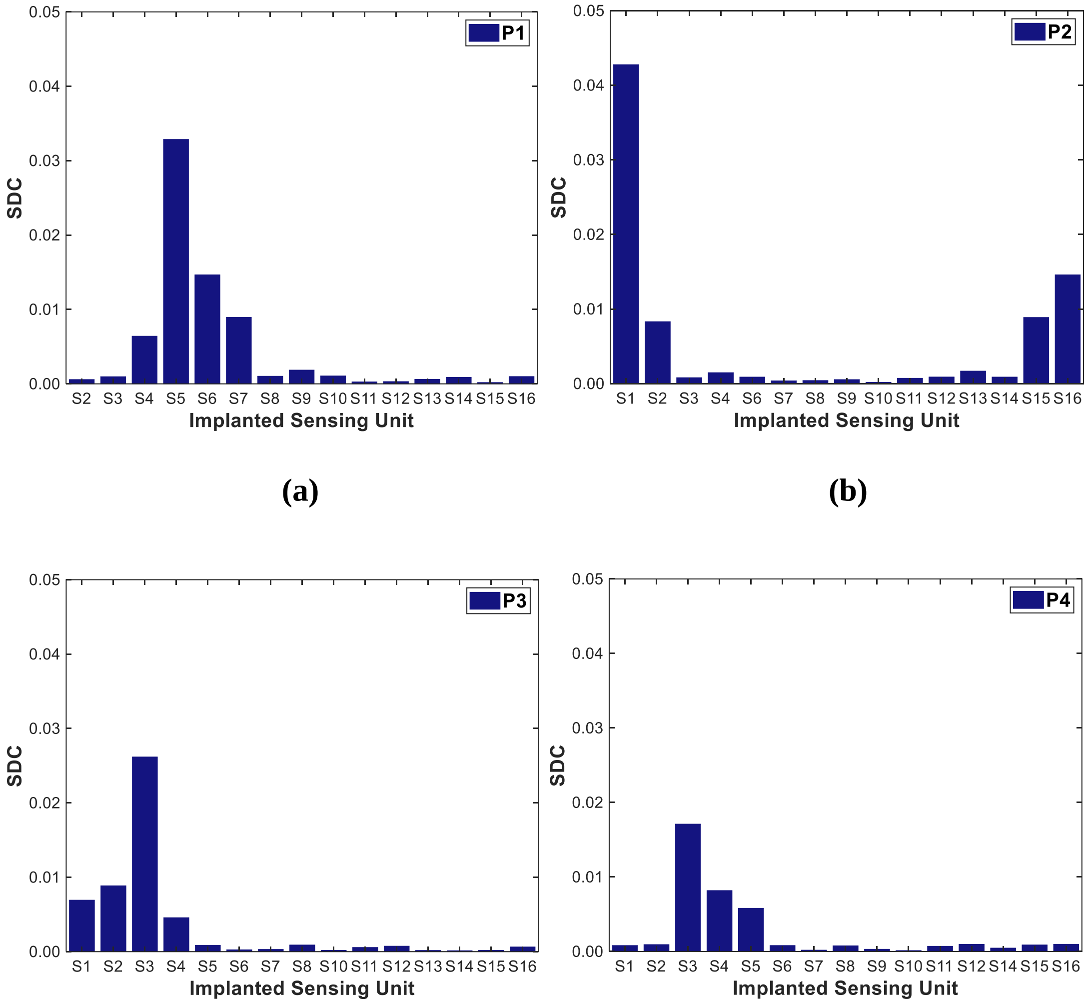

(a) **(b)**

(c) **(d)**

Figure 4.8 Calculated SDC values for different sensing paths when (a) P1, (b) P2, (c) P3, and (d) P4 are used as the wave actuator.

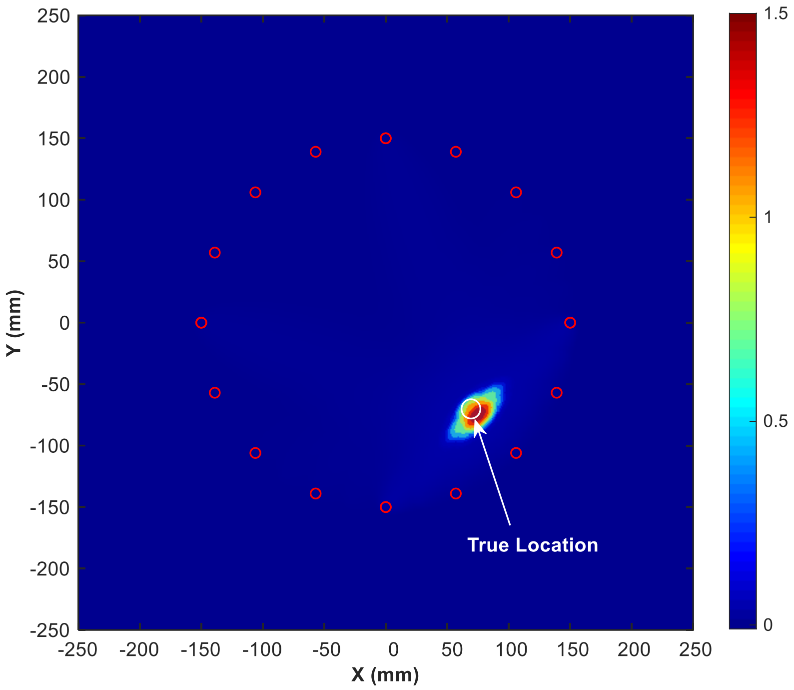

(a)

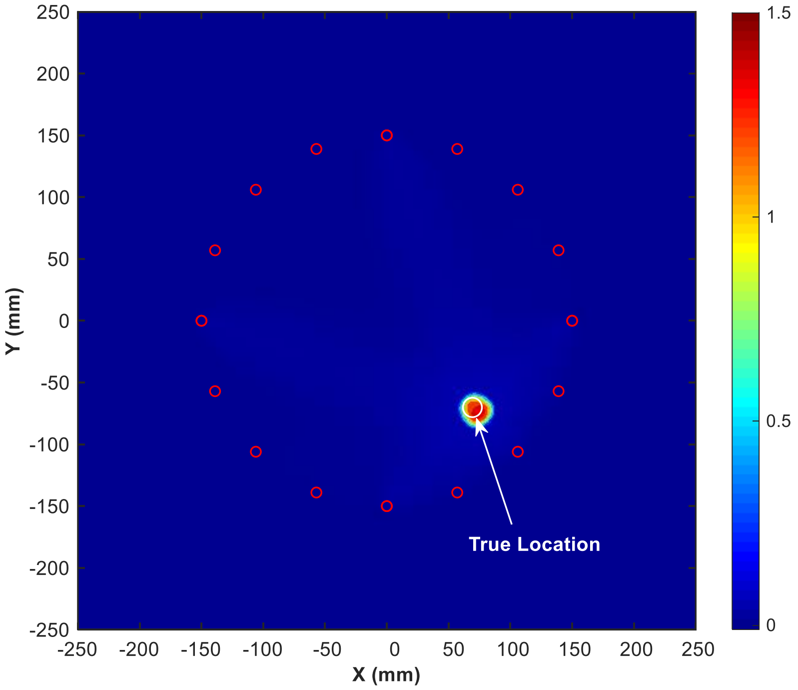

(b)

Figure 4.9 Tomographic images constructed using (a) conventional, and (b) enhanced RAPID algorithms.

4.5 Summary

In this chapter, using the developed implantable sensor network, in conjunction with the use of only a handful of surface-mounted PZT wafers as excitation sources, a dense sensor network can be configured, to circumvent the *limited-angle problem* that conventional UT-based imaging algorithms may have. The implanted sensor network has been proved owing the capability in perceiving GUWs in a broad frequency regime with high precision up to 450 kHz experimentally. The enhanced RAPID-based imaging algorithm, which is revamped by continuously iterating and updating the scale parameter β, presents superior accuracy, compared with the conventional RAPID algorithm when used to evaluate both the location and shape of anomaly, endowing the UT-based SHM with higher imaging resolution while not at the cost of sacrificing the composites' original integrity.

CHAPTER 5

CNN-facilitated Resolution-lossless UT of Composites with Restricted Sensing Capability

5.1 Introduction

In this chapter, a hierarchical, ART-based UT approach, facilitated by CNN-based ML, is developed, targeting resolution-lossless tomography for SHM of composite structures, even when the sensing capability of the composite structures is restricted owing to inadequate transducers of the sensor network. In this approach, a CNN, which features encoder-decoder-type architecture including the convolution and transposed convolution blocks with residual connections, is configured. The blurry ART images, as CNN inputs, are segmented using convolution and max-pooling to extract defect-modulated image features. The max-unpooling boosts the resolution of ART images with transposed convolution. For validation, the sensing capability of a sensor network, which is pre-implanted in a CFRP laminate, is purposefully restricted, to obtain an insufficient number of GUW signals via a mixed numerical and experimental method. Trained by the insufficient inputs, the CNN is used to detect and characterize artificial anomaly and delamination in the CFRP laminate.

5.2 The Algebraic Reconstruction Technique

UT using tomographic algorithms such as FBP, ART, FWI and RAPID, manifests strong dependence on the number of transducers of a sensor network, as well as the locations of individual transducers. By way of illustration, **Figure 5.1** shows schematically two sensor network configurations for UT of a plate waveguide, featuring 32 actuators/32 sensors, **Figure 5.1(a)**, and 4 actuators/32 sensors, **Figure 5.1(b)**, respectively. In both scenarios, 32 sensors are collocated in a circular fashion with an interval of 11.25° between two neighbouring sensors. The two sensor network configurations respectively render 1,024 and 128 sensing paths for UT construction, implying significant loss of sensing paths when the number of actuators is reduced from 32 to 4, while the number of sensors remains unchanged. Such loss potentially leads to restricted sensing coverage, incomplete data acquisition and accordingly ignorance of damage.

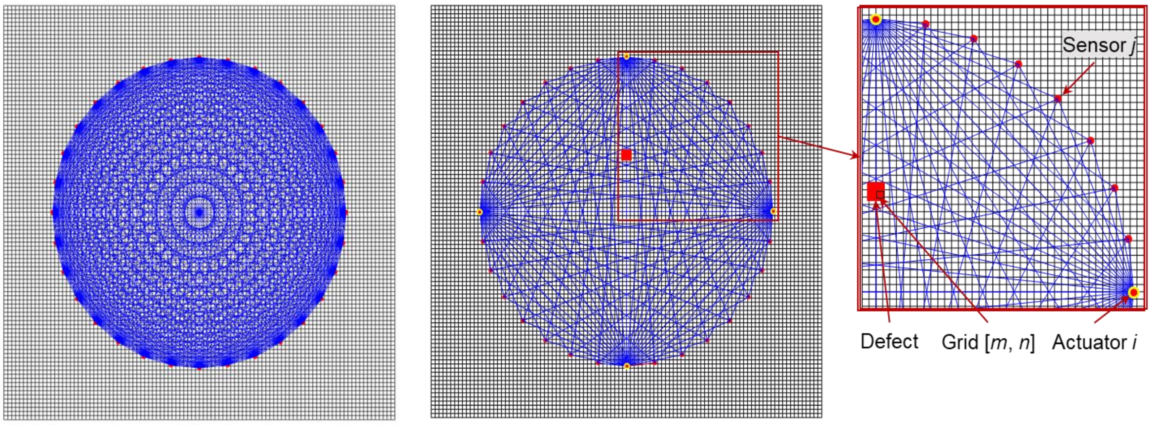

(a) (b)

Figure 5.1 Sensor network configurations for UT imaging with (a) 32 actuators and 32 sensors (red dot: a pair of collocated sensor and actuator); (b) 4 actuators (yellow dots) and 32 sensors (red dots).

Given the same sensing coverage, ART is superior to FBP in terms of imaging precision and accuracy, and ART shows greater convenience and simplicity than RAPID does [9]. UT based on iterative ART is implemented by virtue of the following five key steps: (i) the inspected area is virtually meshed into dense grid cells, **Figure 5.1(b)**; (ii) for an actuator-sensor pair of the sensor network, the change in signal features extracted from GUWs (*e.g.*, wave velocity, attenuation in magnitude, difference in time of flight or other wave features) is deemed as the sum of collective contribution from all the cells that lie on the straight sensing path between the actuator and sensor; (iii) the contribution of any cell is proportional to the length of the path in that cell, serving as a weight to regulate the contribution of individual cells; (iv) the presence of damage in any cell changes signal features, and the field value at individual cell along a path can therefore be defined in terms of the change; (v) fusion of field values established by all the available paths of the sensor network across the entire inspection area constructs a tomographic image, in which damage, if any, will be highlighted.

In this proposed approach, the change in the magnitude of a GUW signal owing to the attenuation of the probing GUW in grid cells along propagation path, is extracted for UT image construction, with which the field value of UT image is defined. For a sensor network with a total of I actuators and J sensors, it has

$$\begin{gathered} A[i,j] = A_{ini} \sum_{m,n \in ray[i,j]} EXP\left(-\frac{1}{C}\left(\mu[m,n] \cdot d[i,j,m,n]\right)\right), \\ (i = 1,\ 2,\cdots,I;\ j = 1,\ 2,\cdots,J) \end{gathered} \tag{5.1}$$

where $A[i, j]$ is the magnitude of a captured GUW signal after the probing GUW propagates from the i^{th} actuator to the j^{th} sensor; A_{ini} is the initial amplitude of the probing GUW; $\mu[m, n]$ represents the attenuation of GUW in cell $[m, n]$ along path $[i, j]$; $d[i, j, m, n]$ is the distance in cell $[m, n]$ that the wave travels along path $[i, j]$; C is a constant related to the wave attenuation [155].

Knowing cell distance $d[i, j, m, n]$ – that is the field value defined in terms of the attenuation of GUW in individual cell, $\mu[m, n]$ can be obtained from the measured $A[i, j]$ by solving **Equation 5.1** with iteration using all the available sensing paths of the sensor network. With an estimated initial attenuation value in the cell, $\mu^0[m, n]$, the average difference of attenuation value, $\Delta_{average}\mu[m, n]$, can be expressed as

$$\Delta_{average}\mu[m,n] = \frac{C[\ln(A^{k-1}[i,j]) - \ln(A^{k}[i,j])]}{L[i,j]}, \tag{5.2}$$

where k signifies the iteration number; $L[i, j]$ is the length of the sensing path $[i, j]$, namely from the i^{th} actuator to the j^{th} sensor. In a single iteration, all available sensing paths are involved in the calculation of **Equation 5.2**. Via each sensing path, the change in wave attenuation is obtained, and the change for each individual cell is updated by taking the average difference of attenuation value $\Delta_{average}\mu[m, n]$ obtained for that cell, which is then added to the current attenuation, as

$$\mu^{k+1}[m,n] = \mu^{k}[m,n] + \Delta_{average}\mu[m,n]. \tag{5.3}$$

The above steps are repeated till the desired accuracy is met, namely when $A^k[i, j]$ converges to the measured magnitude from either simulation or experiment. Upon extending the iteration via **Equation 5.2** to all the available sensing paths of the sensor network, the field value, μ[m, n], at each grid cell of the inspection area (*i.e.*, the field value) is obtained, with which the UT image is constructed. The constructed UT image reflects changes in wave attenuation magnitude across the entire inspection area, to highlight structural damage or material degradation which attenuates GUW signals at a higher degree than that induced by inherent viscoelasticity of the waveguide material.

5.3 CNN-enabled ART Imaging

The iterative nature of ART for calculating wave attenuation along a GUW propagation path, as detailed in the above, entails a dense meshing of the inspection area, as well as a dense sensor network to render a high degree of coverage of meshed cells. In the contrast, a sparse sensor network, with insufficient sensing paths, tends to inferior accuracy and ill-posed UT images, provided ART algorithm is adopted. To circumvent this deficiency, a hierarchical CNN is developed to supplement the above ART-based UT, targeting resolution-lossless tomographic imaging, even when the sensing capability of the sensor network is restricted.

The CNN is a feed-forward neural network, consisting of convolution layers, pooling layers and full connection layers, and it uses the convolutional layers to filter inputs and extract essential input features. Among convolution layers, the output C^l of the l^{th} convolution layer is obtained by convoluting the convolution kernels K^l with input C^{l-1}, consequence of which is then added with an offset, b^l, via a non-linear activation function f, as

$$C^l = f_{act}(C^{l-1} \otimes K^l + b^{l-1}), \tag{5.4}$$

where $\otimes$ denotes the convolution operation; the input C^{l-1} and output C^l are in the form of a vector or a matrix; the convolution kernels K^l performs as a filter; the offset b^l remains the value of one for a standard convolutional operation; the non-linear activation function f_{act} is selected as the ReLU function to ensure computational efficiency [30].

Upon the above convolutional operation via **Equation 5.4**, the outputs are transferred to the pooling layer for feature selection and filtering. The pooling layer features a pre-set pooling function, with which the original feature elements in the feature vector are superseded with its statistics. To achieve this, the max-pooling, instead of average-pooling, is used to recognize image edge, by only choosing the maximum values in the feature vectors as the key features. The outputs are down-sampled feature vectors that highlight the most prominent features of the image edge, rather than the average values of the features in average-pooling. For an ART image that is defined with a two-dimensional matrix, the larger the matrix value the lower the probability of defect it will be. This facilitates recognition of the edge of the defect and implementation of the down-sampling by using max-pooling. The down-sampling of feature vectors based on the max-pooling rule is defined as

$$C^{l+1} = down(C^l)\,. \tag{5.5}$$

After feature extraction and selection from the input data with the convolutional layers and pooling layers, the updated feature vectors are combined with selected key features in the full connection layers or transposed convolution layers, to deliver the outputs. Driven by such a training philosophy, the proposed CNN – a fully convolutional network, has of a hierarchical architecture of an encoder-decoder type with multiple skip connections.

Now consider a sparse sensor network with a restricted sensing capacity. Each actuator-sensor pair in the sensor network acquires the magnitudes of GUW signals, on which basis a UT image is constructed using ART algorithm. Owing to the restricted sensing capability and therefore insufficient GUWs to fulfil ART, the constructed image is expected to be low-resolution and blurry. The constructed image is the input of the hierarchical CNN. As seen in **Figure 5.2**, the proposed CNN embraces the encoder (indicated as encoding layers) and decoder (indicated as decoding layers). The encoder progressively enhances the blurry ART image into high-dimensional feature vectors via multiple layers. Subsequently, the decoder decodes the features that are generated and aggregated by the encoder via multiple layers, to produce a resolution-enhanced image as the output. The operational unit of the encoder is the convolution/max-pooling block with a residual connection (Res-Conn) block.

For illustration, use an ART image of 200×200 pixels – defined in a matrix of 200×200 elements, as an example. The inputted ART image is filtered by convoluting a 3×3 convolution kernel. In this process, the image matrix is down-sampled via **Equation 5.5**, to remain 100×100 matrix elements using the max-pooling with the stride equal to 2, which are the essential features of the original ART image. Res-Conn block carries out a batch normalization (BN) and a non-linear activation with ReLU in sequence. To avoid overfitting, the drop-out regularization layers are included in the Res-Conn block, to mitigate overfitting. Each convolution/max-pooling step with Res-Conn block is repeated three times, to facilitate remaining learning and to deep train the CNN efficiently. Similarly, the fundamental operational unit of the decoder is the transposed convolution/max-unpooling block with the Res-Conn block. Both the transposed convolution and max-unpooling double the up-sampling of the inputted feature vectors, each repeating three times. At the last, a resolution-enhanced ART image, with an augmented resolution of 1600×1600 pixels, is produced, by utilizing down-sampling (half) three times and up-sampling (double) six times. Throughout the CNN training, all the filters of the convolutional networks are updated based on the results from immediate past training.

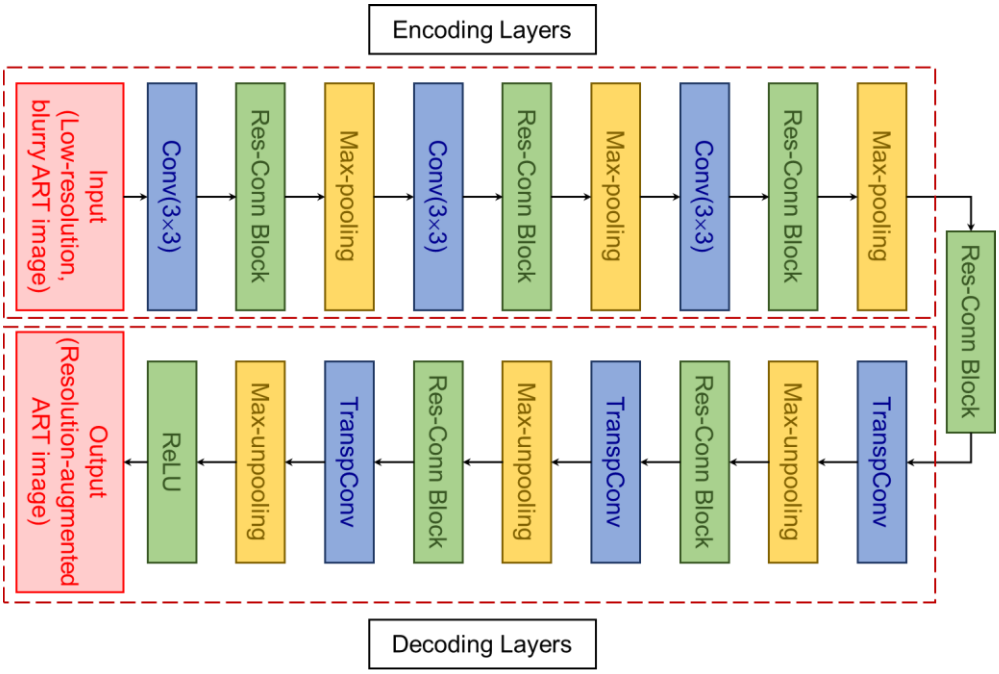

Figure 5.2 Hierarchical architecture of the proposed CNN

With the deep-trained CNN, an ART image of low resolution due to insufficient GUW signals provided by a sparse sensor network with a restricted sensing capacity, is enhanced significantly. In the meantime, the drop-out regularization layers and BN layers effectively avoid the overfitting in the Res-Conn blocks.

5.4 Numerical Simulation and Experiment for Training Data Generation

To fulfil the above deep-training, labelled image databases are of necessity that constitute pixel-wise labelled input/output image pairs for training and validation. To this end, a mixed approach, via numerical simulation and experiment, is developed to generate GUW signals under a diversity of damage scenarios and accordingly develop the labelled image databases using the ART algorithm.

5.4.1 Numerical Simulation for Training Data Generation

Three-dimension (3-D) finite element (FE) simulation is carried out to simulate GUW propagation under different damage scenarios. **Figure 5.3** displays the FE model of an 8-layer, 1.15 mm-thick, quasi-isotropic CFRP laminate with the stacking sequence of $[0°/90°/45°/-45°]_S$. The key material properties and parameters used in simulation are summarized in **Table 5.1**. The in-plane, radial tractions are applied on the surface of the CFRP laminate model, as shown in **Figure 5.3**, to introduce a probing GUW which takes the waveform of a 5-cycle toneburst with a centre frequency of 175 kHz. Under this wave excitation, the corresponding GUW wavefields in the CFRP laminate are acquired numerically at 32 sensing points, which are arranged in a circular manner with an interval of 11.25° and between the 4th and 5th layers of the laminate.

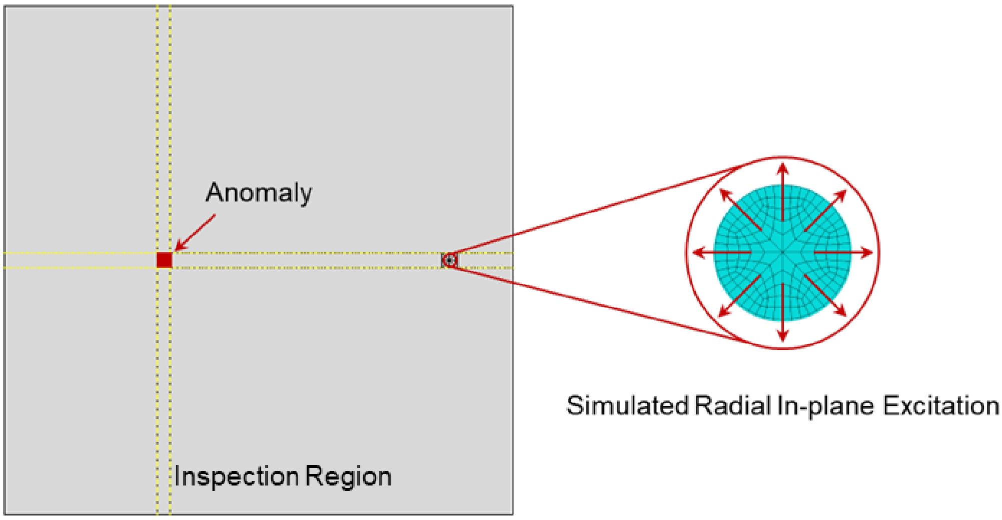

Figure 5.3 3-D FE model of a CFPR laminate for simulating GUW propagation under different damage scenarios

Table 5.1 Key material properties of CFRP laminate used in simulation

Properties	Value
Density (ρ)	1550 kg/m^3
Young's modulus (Longitudinal) (E_1)	144 GPa
Young's modulus (Transverse) (E_2)	10 GPa
Shear modulus (G_{12})	4.2 GPa
Poisson's ratio (μ_{12})	0.25

Without loss of generality, the specific type of defect considered is an adhesive anomaly on the surface of the CFRP laminate. Various sizes and locations of the defect, either of a circular or a rectangular shape, are simulated, leading to a total of 120 scenarios. Note that the sizes and locations of the defect are selected randomly from the Gaussian distribution, with the mean radius of 25 mm and the standard deviation of 12.5 mm for the circular defect, and the mean side length of 50 mm and the standard deviation of 25 mm for the rectangular defect. It takes ~120 min to accomplish the simulation of each scenario, based on a computer having 12 CPUs with 2.6 GHz of clock speed and 16 GB RAM.

5.4.2 Experiment for Training Data Generation

To improve the accuracy of the database for CNN training that is developed via numerical simulation in the above, a number of damage scenarios are created experimentally, in which GUWs under individual scenarios are acquired to supplement numerical simulation. A quasi-isotropic CFRP laminate (500 × 500 × 1.15 mm^3) is prepared in accordance with a standard autoclaving procedure. The laminate is of 8-layer unidirectional prepregs (T300, Torayca®) with the stacking sequence of $[0°/90°/45°/-45°]_S$.

The sensing units, as shown in **Figure 5.4(a)**, are formulated with GNSs and PVP, fabricated using a spray deposition process, and electrified via highly conductive CNT-fibres as wires. The width and length of the sensing unit are precisely controlled to be ~5 mm and ~20 mm respectively, and the thickness of each sensing unit is ~45 μm only – as calibrated in SEM images. A total of 32 thus-fabricated sensing units (denoted by S1 – S32) are networked with CNT-fibres-based wires to form a sensor network, which is then implanted between the 4th and 5th layers of each laminate during autoclaving, as illustrated schematically in **Figure 5.4(b)**. The autoclave mould is heated at a rate of 1.5 °C /min from an ambient temperature to 80 °C, followed with a post-curing at 130 °C for another one hour. The curing pressure remains at 160 psi, ensuring accurate positioning of each sensing unit in the CFRP laminate during fabrication. Upon full curing, the nominal thickness of the laminate measures ~1.15 mm. The CFRP laminate is then trimmed using a water jet cutter (OMAX® PROTOMAX). Four PZT wafers (labelled as P1 – P4) (PSN-33; Ø 12 mm, 1 mm-thick) – used as wave actuators – are surface-mounted on the CFRP laminate, in conjunction with the use the pre-implanted 32 sensing units, to form 4 × 31 = 124 sensing paths (note that each of the four surface-mounted PZT wafers is atop a pre-implanted sensing unit, accordingly reducing four actuator-sensor pairs).

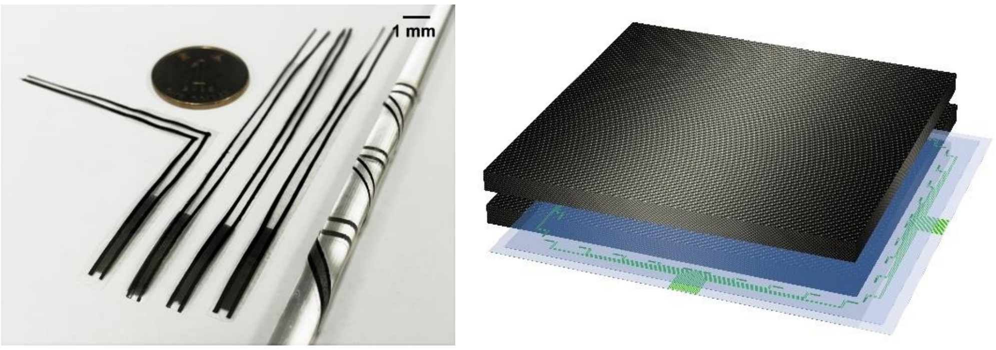

(a) **(b)**

Figure 5.4 (a) Fabricated light-weight, flexible sensing units formulated with nanocomposite hybrid; (b) conceptual illustration of CFRP laminate with pre-implanted sensing units.

The experimental set-up for *in-situ* generation and acquisition of GUWs is shown in **Figure 4.3** in Chapter 4.3. In the set-up, the signal generation module consists of an arbitrary waveform generator on NI® PXIe-1071 platform, and a linear power amplifier (Ciprian® US-TXP-3); the data acquisition module includes a self-developed amplification unit for mitigating ambient noise, a resistor-adjustable Wheatstone bridge for converting piezoresistive variation to electrical signals, and an oscilloscope (Agilent® DSO 9064A) for registering GUW signals. Four PZT wafers are connected with the signal generation module, while the 32 sensing units are linked to the data acquisition module. A five-cycle Hanning-function-modulated sinusoidal toneburst with the central frequency at 175 kHz is excited with the arbitrary waveform generator and applied on each PZT wafer in turn via the power amplifier, to emit probing GUW into the CFRP laminate. The modulated excitation provides concentrated energy in a narrowed frequency band, efficiently reducing wave dispersion and benefiting signal interpretation.

As representative signals acquired, **Figure 5.5** compares the GUW signals generated with P1 and captured with S9, before and after a rectangular anomaly (a rectangular steel block; measuring 50 × 30 × 50 mm^3, weighting mass 500 g) is adhered to the laminate using a glycerol as the coupling agent on the midpoint of the sensing path P1 – S9. Both the S_0 mode and A_0 mode are recognized in captured signals, according to their respective arrival time. The introduction of artificial anomaly on the laminate surface is observed to attenuate the magnitude of the probing GUW signal at a higher degree, in comparison with the counterpart signal.

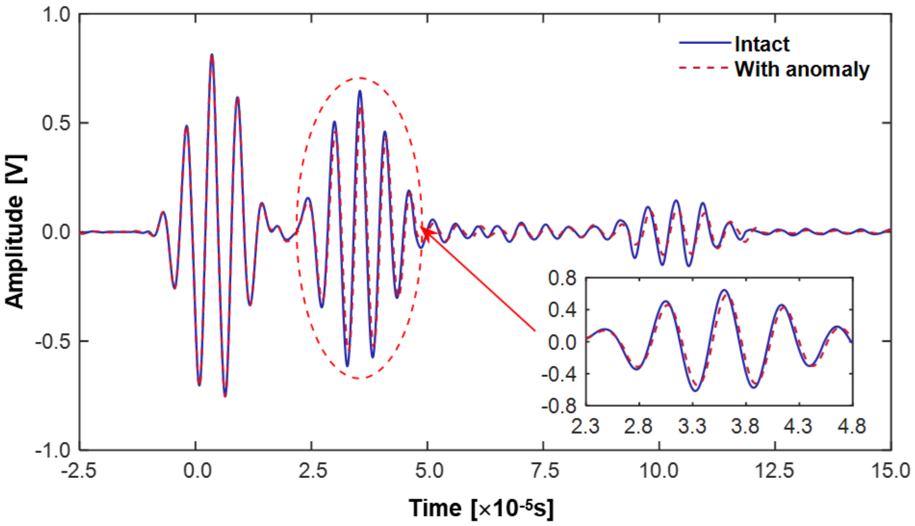

Figure 5.5 GUW signals captured via the sensing path P1 – S9 at 175 kHz before and after the artificial anomaly introduced.

Once the GUW databases are obtained via the mixed approach including numerical simulation and experiment, the labelled input/output image databases are computed using the ART algorithm as described in Chapter 5.2. For the configured labelled image databases, the CNN is trained with 128 labelled image pairs (96 scenarios from numerical simulation and 32 from experiment). **Table 5.2** shows the distribution of defect sizes and locations in numerical simulation and experiment for training databases. The inspection region is divided into Area I, II, III, and IV according to the four quadrants of the Cartesian coordinate system, as shown in **Figure 5.6**. Note that the sizes and locations of the defect are selected randomly from the Gaussian distribution.

Table 5.2 The distribution of defect sizes and locations in numerical simulation and experiment for training databases.

Types of defect	Locations of defect	Sizes of defect		Numbers of simulation scenarios	Numbers of experiment scenarios
		Radius / length (mm)	Height (mm)		
Circular anomaly	Area I	25 ± 12.5	30 ± 20	12	4
	Area II			12	4
	Area III			12	4
	Area IV			12	4
Rectangular anomaly	Area I	50 ± 25	30 ± 20	12	4
	Area II			12	4
	Area III			12	4
	Area IV			12	4
Total scenarios				96	32

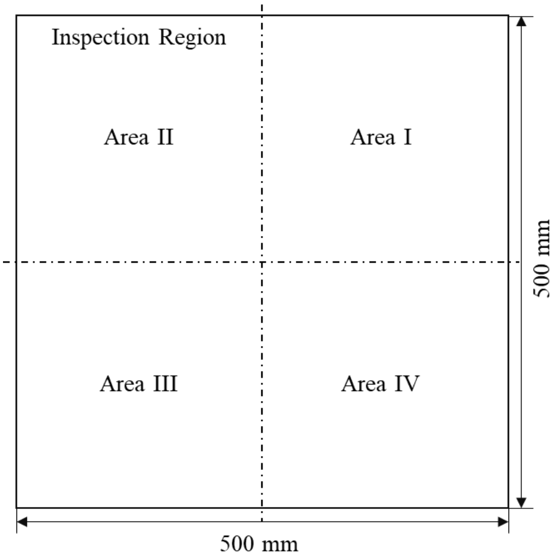

Figure 5.6 The inspection region with four divided areas.

5.5 Validation, Results and Discussion

To validate the developed CNN-facilitated resolution-lossless tomography approach, another 32 damage scenarios (24 from numerical simulation and eight from experiment) are obtained using the same simulation and experiment approach. **Figure 5.7** shows the UT image of a circular anomaly (a circular block; Ø 50 mm, 50 mm-thick) on the laminate surface, in numerical simulation. The ART image obtained via conventional ART algorithm as described in Chapter 5.2 is shown in **Figure 5.7(a)**, in which the image intensity is normalized with regard to its maximal. The image, in a low resolution, pinpoints the anomaly but with artifacts, as a result of the insufficient GUW signals for ART-based UT that are rendered by the sparse sensor network. The UT image is then used as the input to the deep-trained CNN, and the output image is compared in **Figure 5.7(b)**, in which the defect is precisely revealed with high resolution and minimized artifacts, in quantitative agreement with the real anomaly.

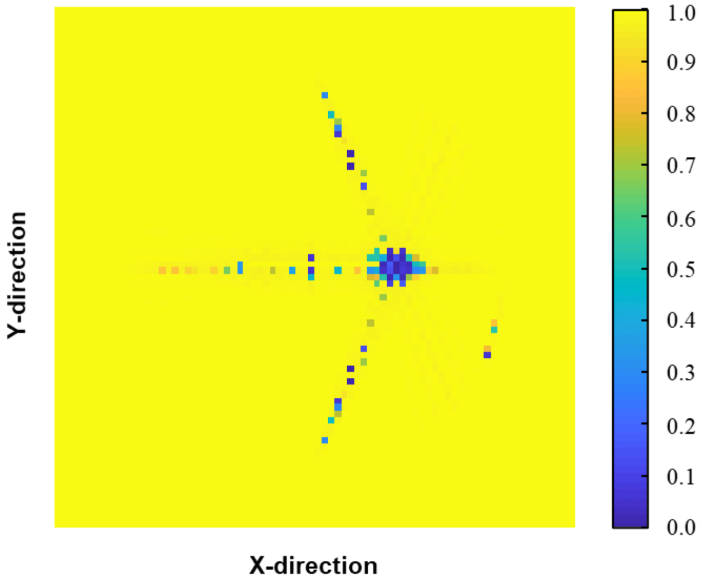

(a)

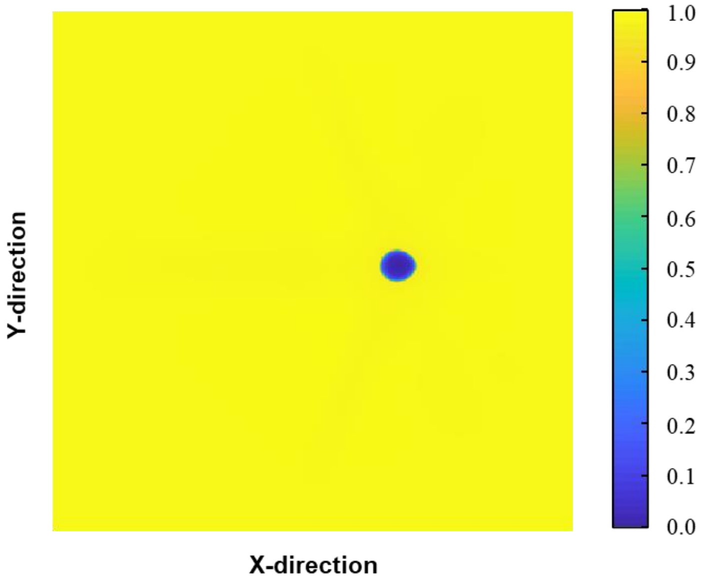

(b)

Figure 5.7 UT images of a circular anomaly on the CFRP laminate (in simulation): (a) image obtained using conventional ART algorithm; (b) resolution-enhanced image using trained CNN (with the image in (a) as CNN input).

In addition to the above validation using a simulated damage scenario, **Figure 5.8** shows the UT image of a circular anomaly (a rectangular steel block; measuring 50 ×

30 × 50 mm^3, weighting 500 g) on the laminate surface, in experiment. Analogously, the CNN-facilitated UT demonstrates enhanced resolution, adequate accuracy and minimized artifacts.

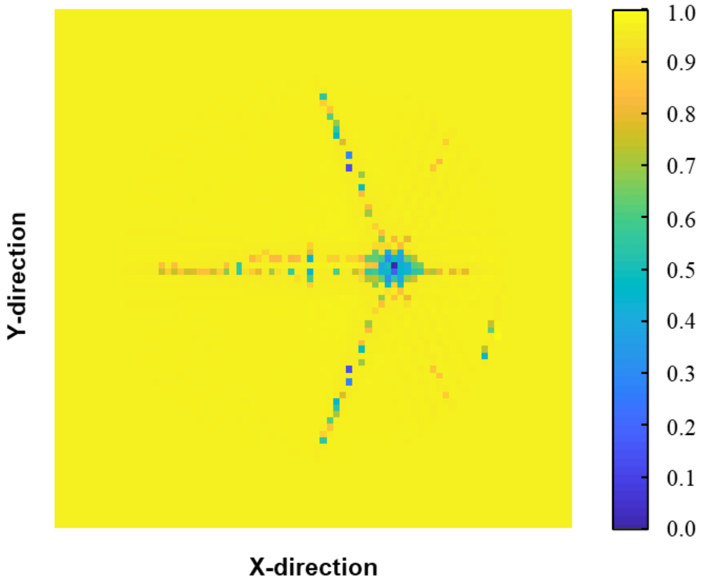

(a)

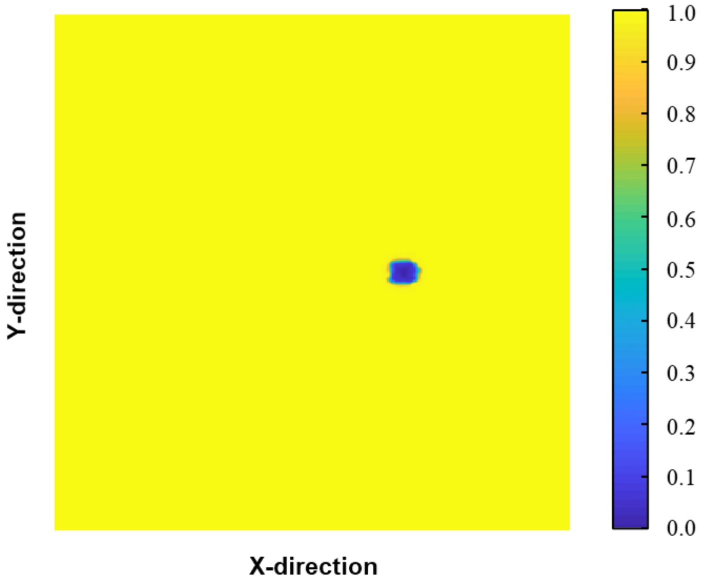

(b)

Figure 5.8 UT images of a rectangular anomaly on the CFRP laminate (in experiment): (a) image obtained using conventional ART algorithm; (b) resolution-enhanced image using trained CNN (with the image in (a) as CNN input).

To take a step further, to testify the compatibility of the trained CNN when extended to new inputs which are not included in the training, interlaminar delamination, rather than surface-adhered artificial anomaly used for database development, is also considered in the validation. **Figure 5.9** shows the UT images constructed of interlaminar delamination which is introduced by low-velocity impact using a hemispherical impactor in the CFRP laminate, in which more artifacts and lower image resolution are noted, compared with the UT images in **Figure 5.7(a)** and **Figure 5.8(a)** for surface anomaly. The low-resolution image is fed into the trained CNN, with result in **Figure 5.9(b)**, manifesting remarkably elevated contrast, minimized artifacts and enhanced resolution.

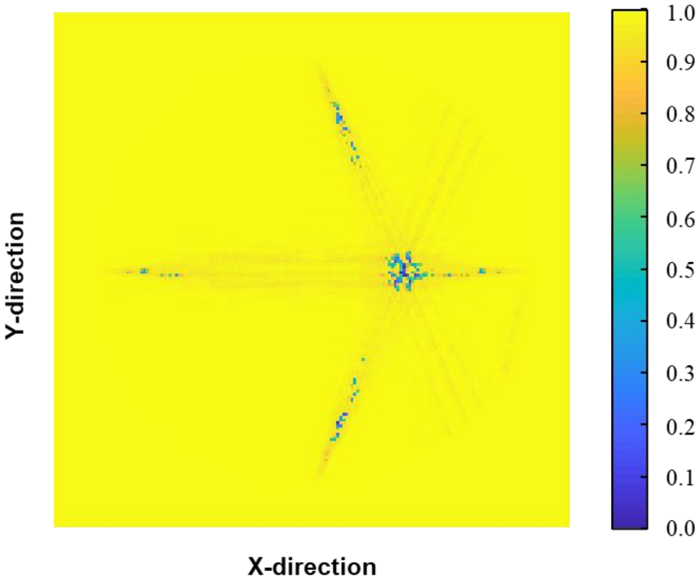

(a)

Figure 5.9 UT images of interlaminar delamination in the CFRP laminate (in experiment): (a) image obtained using conventional ART algorithm; (b) resolution-enhanced image using trained CNN (with the image in (a) as CNN input).

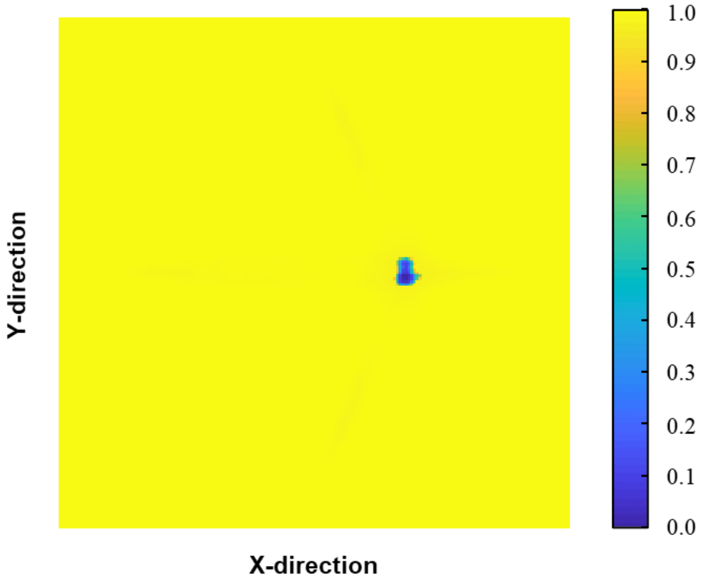

(b)

Figure 5.9 ***Cont.***

Extending the above validation from singular defect to multiple-defect, two sites of delamination are introduced by using a hemispherical impactor in the laminate. **Figure 5.10** displays the UT images constructed, to observe similar enhancement in imaging quality, in **Figure 5.10(b)**. This result is further compared with the image obtained using 32 surface-mounted PZT wafers, as shown in **Figure 5.10(c)**, in which are collocated consistently with the implanted sensors to form a dense sensor network on the same laminate. The CNN processed defect imaging result demonstrates lossless recovery of the delamination defect details from the low-resolution ART image. At the same time, it is also proved that the proposed method is effective in solving restricted sensing capability experimentally. Compared with the experimental tomography imaging result in **Figure 5.10(d)** using the same arrangement of PZT wafers, the quantitative performance evaluation metric (Dice coefficient) values for the two delamination defect close to 95%, which achieved a true resolution-lossless tomography imaging.

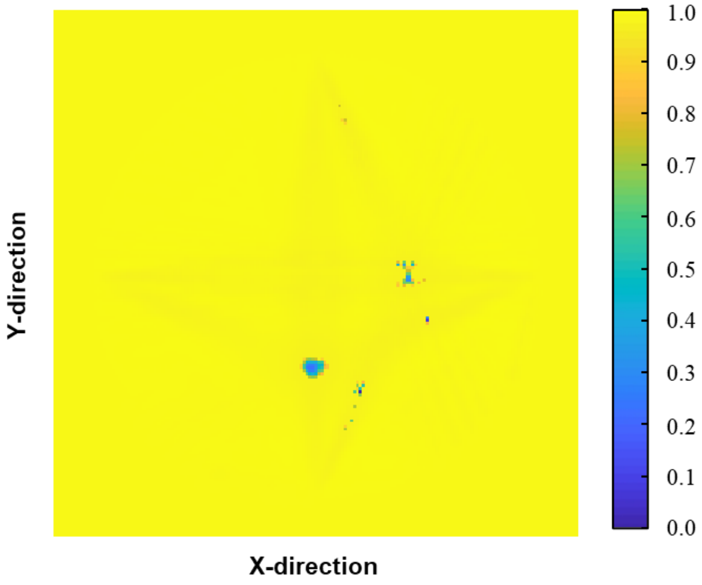

(a)

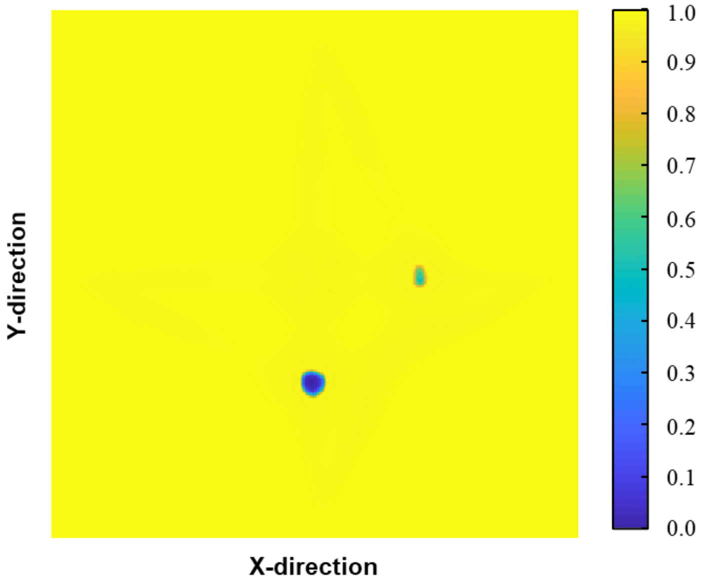

(b)

Figure 5.10 UT images of two sites of interlaminar delamination in the CFRP laminate (in experiment): (a) image obtained using conventional ART algorithm with a sparse sensor network (offering 124 sensing paths); (b) resolution-enhanced image using trained CNN (with the image in (a) as CNN input); (c) a dense sensor network on CFRP laminate surface consisting of 32 PZT wafers (offering 992 sensing paths); (d) image obtained using conventional ART image with the dense sensor network.

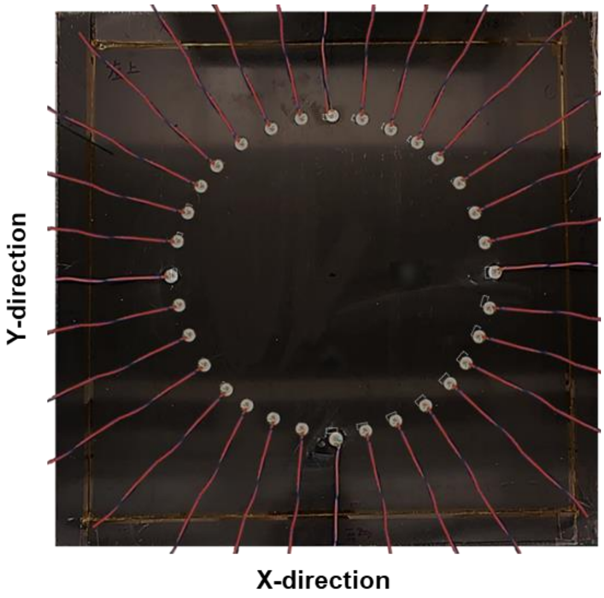

(c)

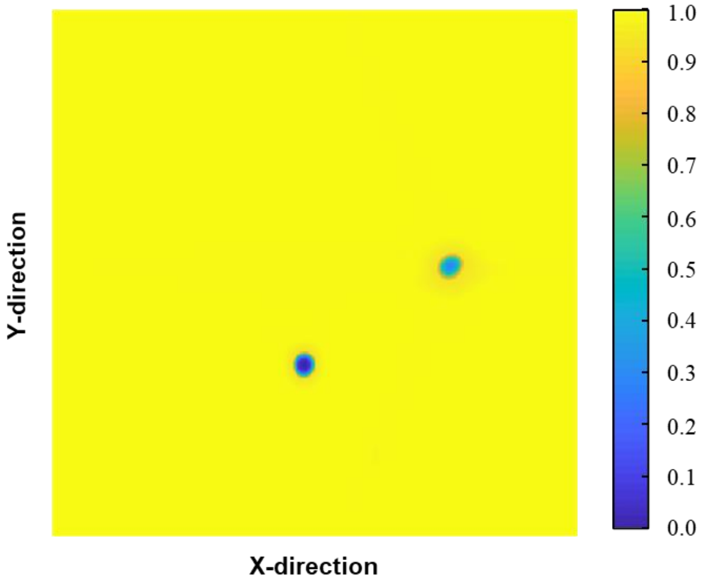

(d)

Figure 5.10 ***Cont.***

5.6 Summary

In this chapter, a new tomographic imaging approach, enabled by CNN-based ML and facilitated by ART, is developed to deliver resolution-lossless tomography for SHM of composite structures. The CNN features an encoder-decoder-type architecture including the convolution and transposed convolution blocks with residual connections. The blurry ART images are segmented using convolution and max-pooling to extract defect-associated details. The max-unpooling boosts the resolution of ART images with transposed convolution. To avoid overfitting, drop-out regularization layers and BN layers are also included in the Res-Conn blocks. To train and validate the CNN, a series of numerical simulations and experiments using implanted sensor network in CFRPs are conducted to generate GUW databases with inadequate sensing capability. This result demonstrates that the proposed approach can accurately image artificial anomaly and delamination in the laminate, effectively solve the restricted sensing capability and restore the defect details from a blurry ART image, and in the meantime remarkably reduce the false defect detection rate by suppressing misleading image artifacts.

CHAPTER 6

Conclusions and Recommendation for Future Study

6.1 Concluding Remarks

In this PhD study, an implantable, nanocomposite-inspired, piezoresistive sensor network is developed for implementing UT-based SHM of carbon fibre-reinforced polymer (CFRP) laminates. The nanocomposite ink, formulated with graphene nanosheets (GNSs) and polyvinylpyrrolidone (PVP), is tailored to acquire the percolation threshold of conductive nanofillers. The above ink is then deposited on partially precured B-stage epoxy films using spray deposition process and circuited via highly conductive carbon nanotube fibres (CNT-fibres) as wires, to form a dense sensor network, which is then implanted into CFRP laminates during autoclaving procedure. With a morphologically optimized nano-architecture in nanocomposites, the quantum tunnelling effect can be triggered in percolated networks, which enables the sensors to faithfully response from quasi-static loads to high-frequency guided ultrasonic waves (GUWs). Quasi-static tensile test is performed to gauge possible degradation in tensile properties and change in failure modes of the CFRP laminates owing to the implantation of a sensor network.

Using the developed implantable sensor network, in conjunction with the use of only a handful of surface-mounted PZT wafers as excitation sources, a dense sensor network can be configured, to circumvent the *limited-angle problem* that conventional UT-based imaging algorithms may have. The implanted sensor network has been proved owing the capability in perceiving GUWs in a broad frequency regime with high precision up to 450 kHz experimentally. The enhanced reconstruction algorithm for the probabilistic inspection of damage (RAPID)-based imaging algorithm, which is revamped by continuously iterating and updating the scale parameter β, presents superior accuracy, compared with the conventional RAPID algorithm when used to evaluate both the location and shape of anomaly, endowing the UT-based SHM with higher imaging resolution while not at the cost of sacrificing the composites' original integrity.

To further achieve real *in-situ* UT-based SHM and solve the restricted sensing capability due to inadequate sensing paths in the implanted sensor network, a hierarchical, algebraic reconstruction technique (ART) based tomographic imaging approach, facilitated by convolutional neural network (CNN) based machine learning (ML), is developed, targeting resolution-lossless tomography for SHM of composites. The blurry ART images, as the inputs to train a CNN with an encoder-decoder-type architecture, are segmented using convolution and max-pooling to extract defect-modulated image features. The max-unpooling boosts the resolution of ART images with transposed convolution. Trained with the insufficient databases via a mixed numerical and experimental method, the CNN is used to detect and characterize artificial anomaly and delamination in the CFRP laminates. Results demonstrate that the developed approach accurately images artificial anomaly and delamination, in the meantime it minimizes the false alarm by eliminating image artifacts.

In conclusion, starting from mechanism study, through design to fabrication of sensors, new breeds of implantable, nanocomposite-inspired, piezoresistive sensor network is developed. Successful application paradigms in UT of the implanted sensor network, either using the enhanced RAPID or ML-enabled imaging, have accentuated the alluring potentials of *in-situ* UT-based SHM.

6.2 Remaining Issues and Recommendation for Future Study

(i) Aerosol jet printing: aerosol jet printing is an emerging contactless direct write approach aimed at the production of fine features on a wide range of substrates, as shown in **Figure 6.1**. Compared with spray-coating and ink jet printing, aerosol jet printing has the following advantages: (i) aerosol jet printing allows to achieve a higher print resolution, namely, almost two to four times higher than ink jet printing; (ii) method of aerosol jet printing have less strict requirements for the viscosity of ink, and therefore, a larger amount of materials can be printed by using aerosol jet; (iii) aerosol jet printing has a greater opportunity to vary the distance between the print head to the substrate. Therefore, it is possible to print on non-flat (non-smooth) substrates.

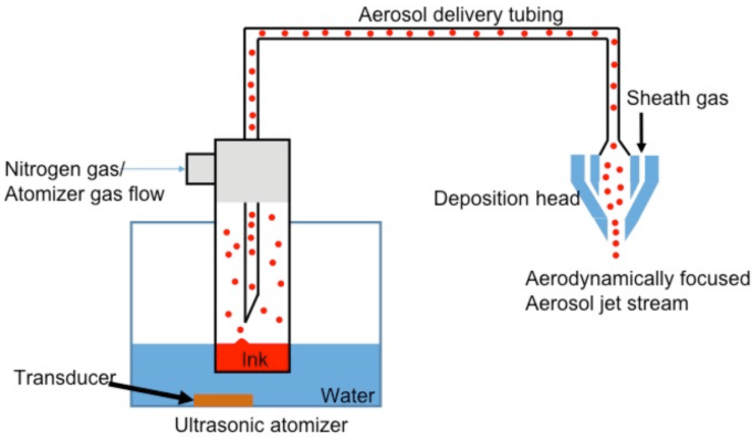

Figure 6.1 Schematic of Aerosol jet printing process.

(ii) Print circuit: with inevitable intrusion to composite structures, not only sensors but also cables and wires could degrade the structural integrity to some extent, regardless of their intended role of detecting defect- or damage-caused structural degradation and impose weight and penalty to original composite structures. The reliance on cables and wires to network individual sensors is still persistent. The use of printed circuits may reduce the weight and volume of cables and wires. **Figure 6.2** shows an example of using printed circuits as wires to form a dense sensor network.

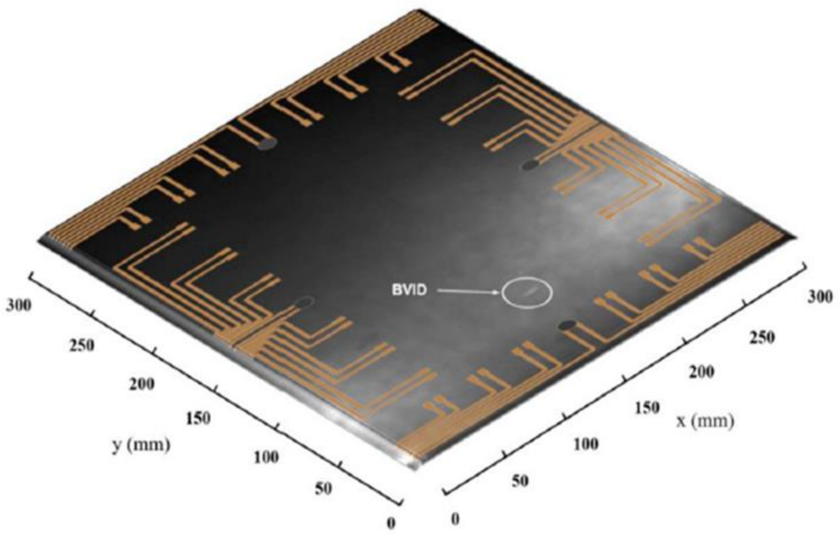

Figure 6.2 Illustration of using printed circuits to form a dense sensor network.

(iii) Sensor direction: in the process of making the nanocomposite ink, the nanofillers have been evenly dispersed inside the epoxy and ethanol. For an individual sprayed nanocomposite-inspired sensor, it can be considered as isotropic. But with the introduction of the electrode, the isotropic property already has been changed for the sensing unit Considering that the wave propagation is also directional. Hence, the characteristic of sensor direction is also part of the future works.

(iv) Laser ultrasonic: laser-ultrasonics uses lasers to generate and detect ultrasonic waves. It is a non-contact technique used to measure materials thickness, detect flaws and carry out materials characterization, as shown in **Figure 6.3**. Using laser ultrasonic as excitation to replace PZT wafers, which can further reduce the weight and volume penalty to the host composite structures.

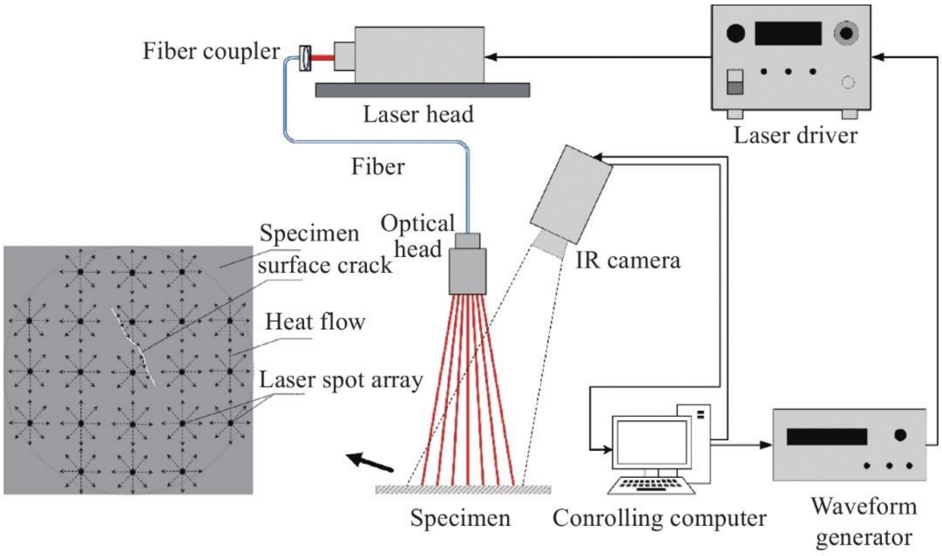

Figure 6.3 Schematic of the noncontact laser ultrasonic wavefield imaging system.

BIBLIOGRAPHY

[1] Su, Zhongqing, *et al*. "Identification of damage using Lamb waves: from fundamentals to applications." Vol. 48. Springer Science & Business Media, 2009.

[2] Subbarao, P. M. V., *et al*. "Performance of iterative tomographic algorithms applied to non-destructive evaluation with limited data." Ndt & E International 30.6 (1997): 359-370.

[3] McKeon, James C., *et al*. "Parallel projection and crosshole Lamb wave contact scanning tomography." The Journal of the Acoustical Society of America 106.5 (1999): 2568-2577.

[4] Malyarenko, Eugene V., *et al*. "Fan beam and double crosshole Lamb wave tomography for mapping flaws in aging aircraft structures." The Journal of the Acoustical Society of America 108.4 (2000): 1631-1639.

[5] Leonard, Kevin R., *et al*. "Ultrasonic Lamb wave tomography." Inverse Problems 18.6 (2002): 1795.

[6] Leonard, Kevin R., *et al*. "Multi-mode Lamb wave tomography with arrival time sorting. " The Journal of the Acoustical Society of America 117.4 (2005): 2028-2038.

[7] Wang, Kai, *et al*. "Analytical insight into “breathing” crack-induced acoustic nonlinearity with an application to quantitative evaluation of contact cracks." Ultrasonics 88 (2018): 157-167.

[8] Zhao, Xiang, *et al*. "Active health monitoring of an aircraft wing with embedded piezoelectric sensor/actuator network: I. Defect detection, localization and growth monitoring." Smart materials and structures 16.4

(2007): 1208.

[9] Zhao, Xiang, *et al*. "Ultrasonic Lamb wave tomography in structural health monitoring." Smart Materials and Structures 20.10 (2011): 105002.

[10] Ren, Yuanqiang, *et al*. "A diagnostic imaging approach for online characterization of multi-impact in aircraft composite structures based on a scanning spatial-wavenumber filter of guided wave." Mechanical Systems and Signal Processing 90 (2017): 44-63.

[11] Rao, Jing, *et al*. "Investigation of the reconstruction accuracy of guided wave tomography using full waveform inversion." Journal of Sound and Vibration 400 (2017): 317-328.

[12] Hubmer, Simon, *et al*. "Limited-angle acousto-electrical tomography." Inverse Problems in Science and Engineering 27.9 (2019): 1298-1317.

[13] Boukellif, Ramdane, *et al*. "Parameter identification of crack-like notches in aluminum plates based on strain gauge data." Structural Health Monitoring (2020): 1475921720981845.

[14] Yadav, Susheel Kumar, *et al*. "Reliability of crack quantification via acousto-ultrasound active-sensing structural health monitoring using surface-mounted PZT actuators/sensors." Structural Health Monitoring (2020): 1475921720921536.

[15] Si, Liang, *et al*. "Online structural state assessment for aerospace composite structures using an acousto-ultrasonics-based multi-damage index identification approach." Structural Health Monitoring (2020): 1475921719899334.

[16] Sikdar, Shirsendu, *et al*. "Nonlinear elastic wave propagation and breathing-debond identification in a smart composite structure." Composites Part B: Engineering 200 (2020): 108304.

[17] Su, Zhongqing, *et al*. "A built-in active sensor network for health monitoring of composite structures." Smart Materials and Structures 15.6 (2006): 1939.

[18] Qing, Xinlin P., *et al*. "Advances in the development of built-in diagnostic system for filament wound composite structures." Composites Science and Technology 66.11-12 (2006): 1694-1702.

[19] Masmoudi, Sahir, *et al*. "Use of piezoelectric as acoustic emission sensor for in-situ monitoring of composite structures." Composites Part B: Engineering 80 (2015): 307-320.

[20] Dziendzikowski, Michal, *et al*. "In-situ barely visible impact damage detection and localization for composite structures using surface mounted and embedded PZT transducers: A comparative study." Mechanical Systems and Signal Processing 78 (2016): 91-106.

[21] Loutas, T. H., *et al*. "Reliability of strain monitoring of composite structures via the use of optical fiber ribbon tapes for structural health monitoring purposes." Composite Structures 134 (2015): 762-771.

[22] Mei, Hanfei, *et al*. "Pure S0 and SH0 detections of various damage types in aerospace composites." Composites Part B: Engineering (2020): 107906.

[23] Saber, Nasser, *et al*. "Smart thin-film piezoelectric composite sensors based on high lead zirconate titanate content." Structural Health Monitoring 14.3 (2015): 214-227.

[24] Burton, Andrew R., *et al*. "Bio-compatible wireless inductive thin-film strain sensor for monitoring the growth and strain response of bone in osseointegrated prostheses." Structural Health Monitoring (2019): 1475921719831452.

[25] Giri, Paritosh, *et al*. "Characterization of carbon fiber reinforced polymer strengthened concrete and gap detection with a piezoelectric-based sensory

technique." Structural Health Monitoring 18.1 (2019): 172-179.

[26] Ghafari, Ehsan, *et al*. "Self-polarized electrospun polyvinylidene fluoride (PVDF) nanofiber for sensing applications." Composites Part B: Engineering 160 (2019): 1-9.

[27] Jung, Kyung-Chae, *et al*. "Performance evaluation of smart grid fabrics comprising carbon dry fabrics and PVDF ribbon sensors for structural health monitoring." Composites Part B: Engineering 163 (2019): 690-701.

[28] Choi, Kyungwho, *et al*. "Impact monitoring characteristics of piezoelectric paint sensor by thermal fatigue analysis for railroad vehicle applications." Structural Health Monitoring 19.6 (2020): 1951-1962.

[29] Alom, Md Zahangir, *et al*. "The history began from alexnet: A comprehensive survey on deep learning approaches." arXiv preprint arXiv:1803.01164 (2018).

[30] LeCun, Yann, *et al*. "Deep learning." nature 521.7553 (2015): 436-444.

[31] Antholzer, Stephan, *et al*. "Deep learning for photoacoustic tomography from sparse data." Inverse problems in science and engineering 27.7 (2019): 987-1005.

[32] Cai, Yongxing, *et al*. "Subwavelength ultrasonic imaging using a deep convolutional neural network trained on structural noise." Ultrasonics 117 (2021): 106552.

[33] Rautela, Mahindra, *et al*. "Combined two-level damage identification strategy using ultrasonic guided waves and physical knowledge assisted machine learning." Ultrasonics 115 (2021): 106451.

[34] Keshmiri Esfandabadi, Yasamin, *et al*. "Deep learning for enhancing wavefield image quality in fast non-contact inspections." Structural Health Monitoring 19.4 (2020): 1003-1016.

[35] Ebrahimkhanlou, Arvin, *et al*. "A generalizable deep learning framework for

localizing and characterizing acoustic emission sources in riveted metallic panels." Mechanical Systems and Signal Processing 130 (2019): 248-272.

[36] Song, Homin, *et al*. "Noncontact super-resolution guided wave array imaging of subwavelength defects using a multiscale deep learning approach." Structural Health Monitoring 20.4 (2021): 1904-1923.

[37] Hu, Ning, *et al*. "Ultrasensitive strain sensors made from metal-coated carbon nanofiller/epoxy composites." Carbon 51 (2013): 202-212.

[38] Staszewski, W. J. "Ultrasonic/guided waves for structural health monitoring." Key Engineering Materials. Vol. 293. Trans Tech Publications Ltd, 2005.

[39] Mitra, Mira, *et al*. "Guided wave based structural health monitoring: A review." Smart Materials and Structures 25.5 (2016): 053001.

[40] Diamanti, K., *et al*. "Lamb waves for the non-destructive inspection of monolithic and sandwich composite beams." Composites Part A: Applied science and manufacturing 36.2 (2005): 189-195.

[41] Dimitriadis, E. K., *et al*. "Piezoelectric actuators for distributed vibration excitation of thin plates." (1991): 100-107.

[42] Hinders, Mark K., *et al*. "Contact scanning Lamb wave tomography." The Journal of the Acoustical Society of America 104.3 (1998): 1790-1791.

[43] McKeon, James C., *et al*. "Parallel projection and crosshole Lamb wave contact scanning tomography." The Journal of the Acoustical Society of America 106.5 (1999): 2568-2577.

[44] Malyarenko, Eugene V., *et al*. "Fan beam and double crosshole Lamb wave tomography for mapping flaws in aging aircraft structures." The Journal of the Acoustical Society of America 108.4 (2000): 1631-1639.

[45] Leonard, Kevin R., *et al*. "Ultrasonic Lamb wave tomography." Inverse Problems 18.6 (2002): 1795.

[46] Leonard, Kevin R., *et al*. "Multi-mode Lamb wave tomography with arrival time sorting. " The Journal of the Acoustical Society of America 117.4 (2005): 2028-2038.

[47] Jansen, D. P., *et al*. "Lamb wave tomography of advanced composite laminates containing damage." Ultrasonics 32.2 (1994): 83-90.

[48] Hay, T. R., *et al*. "A comparison of embedded sensor Lamb wave ultrasonic tomography approaches for material loss detection." Smart Materials and Structures 15.4 (2006): 946.

[49] Yan, Fei, *et al*. "Ultrasonic guided wave imaging techniques in structural health monitoring." Journal of intelligent material Systems and Structures 21.3 (2010): 377-384.

[50] Rao, Jing, *et al*. "Guided wave tomography based on full waveform inversion." IEEE Transactions on Ultrasonics, Ferroelectrics, and Frequency Control 63.5 (2016): 737-745.

[51] Rao, Jing, *et al*. "Investigation of the reconstruction accuracy of guided wave tomography using full waveform inversion." Journal of Sound and Vibration 400 (2017): 317-328.

[52] Liu, Menglong, *et al*. "Applications of a nanocomposite-inspired in-situ broadband ultrasonic sensor to acousto-ultrasonics-based passive and active structural health monitoring." Ultrasonics 78 (2017): 166-174.

[53] Payo, Ismael, *et al*. "Dynamic characterization of piezoelectric paint sensors under biaxial strain." Sensors and Actuators A: Physical 163.1 (2010): 150-158.

[54] Rallini, M., *et al*. "Nanofillers in polymers." Modification of polymer properties. William Andrew Publishing, 2017. 47-86.

[55] Bhattacharya, Mrinal. "Polymer nanocomposites—a comparison between carbon nanotubes, graphene, and clay as nanofillers." Materials 9.4 (2016):

262.

[56] Ma, Peng-Cheng, *et al*. "Dispersion and functionalization of carbon nanotubes for polymer-based nanocomposites: A review." Composites Part A: Applied Science and Manufacturing 41.10 (2010): 1345-1367.

[57] Kim, Hyunwoo, *et al*. "Graphene/polymer nanocomposites." Macromolecules 43.16 (2010): 6515-6530.

[58] Li, Yehai, *et al*. "Dispersed sensing networks in nano-engineered polymer composites: From static strain measurement to ultrasonic wave acquisition." Sensors 18.5 (2018): 1398.

[59] Li, Yehai, *et al*. "Graphene-functionalized polymer composites for self-sensing of ultrasonic waves: An initiative towards “sensor-free” structural health monitoring." Composites Science and Technology 168 (2018): 203-213.

[60] Hu, Ning, *et al*. "Tunneling effect in a polymer/carbon nanotube nanocomposite strain sensor." Acta materialia 56.13 (2008): 2929-2936.

[61] Hu, Ning, *et al*. "Investigation on sensitivity of a polymer/carbon nanotube composite strain sensor." Carbon 48.3 (2010): 680-687.

[62] Li, Weikang, *et al*. "Carbon nanotube-graphene nanoplatelet hybrids as high-performance multifunctional reinforcements in epoxy composites." Composites Science and Technology 74 (2013): 221-227.

[63] Qiu, Ling, *et al*. "Ultrafast dynamic piezoresistive response of graphene-based cellular elastomers." Advanced Materials 28.1 (2016): 194-200.

[64] Zhou, Pengyu, *et al*. "An inkjet-printed, flexible, ultra-broadband nanocomposite film sensor for in-situ acquisition of high-frequency dynamic strains." Composites Part A: Applied Science and Manufacturing 125 (2019): 105554.

[65] Sebastian, James, *et al*. "Health monitoring of structural composites with

embedded carbon nanotube coated glass fiber sensors." Carbon 66 (2014): 191-200.

[66] Cao, Wuxiong, *et al*. "A Spray-on, Nanocomposite-based sensor network for in-situ active structural health monitoring." Sensors 19.9 (2019): 2077.

[67] Qin Y, Peng Q, Ding Y, Lin Z, Wang C, Li Y, *et al*. Lightweight, superelastic, and mechanically flexible graphene/polyimide nanocomposite foam for strain sensor application. ACS Nano. 2015;9(9):8933-41.

[68] Wu S, Peng S, Han ZJ, Zhu H, Wang CH. Ultrasensitive and stretchable strain sensors based on mazelike vertical graphene network. ACS Applied Materials & Interfaces. 2018;10(42):36312-22.

[69] Zeng, Zhihui, *et al*. "A coatable, light-weight, fast-response nanocomposite sensor for the in-situ acquisition of dynamic elastic disturbance: From structural vibration to ultrasonic waves." Smart Materials and Structures 25.6 (2016): 065005.

[70] Zeng, Zhihui, *et al*. "Ultra-broadband frequency responsive sensor based on lightweight and flexible carbon nanostructured polymeric nanocomposites." Carbon 121 (2017): 490-501.

[71] Liao, Yaozhong, *et al*. "Ultrafast response of spray-on nanocomposite piezoresistive sensors to broadband ultrasound." Carbon 143 (2019): 743-751.

[72] Liao, Yaozhong, *et al*. "An ultra-thin printable nanocomposite sensor network for structural health monitoring." Structural Health Monitoring (2019): 1475921719859338.

[73] Qiu, Lei, *et al*. "Impact monitoring for aircraft smart composite skins based on a lightweight sensor network and characteristic digital sequences." Sensors 18.7 (2018): 2218.

[74] Wang, Yu, *et al*. "A stretchable and large-scale guided wave sensor network for

aircraft smart skin of structural health monitoring." Structural Health Monitoring (2019): 1475921719850641.

[75] Su, Zhongqing, *et al*. "A built-in active sensor network for health monitoring of composite structures." Smart Materials and Structures 15.6 (2006): 1939.

[76] Masmoudi, S., *et al*. "Mechanical behaviour and identification of damage by acoustic emission of smart composites." Multidiscipline Modeling in Materials and Structures (2014).

[77] Masmoudi, Sahir, *et al*. "Use of piezoelectric as acoustic emission sensor for in situ monitoring of composite structures." Composites Part B: Engineering 80 (2015): 307-320.

[78] Masmoudi, Sahir, *et al*. "Effect of piezoelectric implant on the structural integrity of composite laminates subjected to tensile loads." Applied Composite Materials 24.1 (2017): 39-54.

[79] Masmoudi, Sahir, *et al*. "Fatigue behaviour and structural health monitoring by acoustic emission of E-glass/epoxy laminates with piezoelectric implant." Applied Acoustics 108 (2016): 50-58.

[80] Masmoudi, Sahir, *et al*. "Structural integrity of laminated composite with embedded piezoelectric sensors." Design and Modeling of Mechanical Systems-II. Springer, Cham, 2015. 673-680.

[81] Masmoudi, Sahir, *et al*. "Mechanical behavior and health monitoring by acoustic emission of unidirectional and cross-ply laminates integrated by piezoelectric implant." Applied acoustics 86 (2014): 118-125.

[82] Masmoudi, Sahir, *et al*. "Mechanical behaviour and health monitoring by acoustic emission of sandwich composite integrated by piezoelectric implant." Composites Part B: Engineering 67 (2014): 76-83.

[83] Chilles, James S., *et al*. "Monitoring cure and detecting damage in composites

with inductively coupled embedded sensors." Composites Science and Technology 134 (2016): 81-88.

[84] Dziendzikowski, Michał, *et al*. "Localizing impact damage of composite structures with modified RAPID algorithm and non-circular PZT arrays." Archives of Civil and Mechanical Engineering 17.1 (2017): 178-187.

[85] Dziendzikowski, M., *et al*. "In situ Barely Visible Impact Damage detection and localization for composite structures using surface mounted and embedded PZT transducers: A comparative study." Mechanical Systems and Signal Processing 78 (2016): 91-106.

[86] Dziendzikowski, Michal, *et al*. "Structural health monitoring of a composite panel based on PZT sensors and a transfer impedance framework." Sensors 18.5 (2018): 1521.

[87] Katunin, Andrzej, *et al*. "Damage identification in aircraft composite structures: A case study using various non-destructive testing techniques." Composite structures 127 (2015): 1-9.

[88] Wang, Calvin S., *et al*. Impact damage identification of composite structures with built-in piezoelectric sensor/actuator networks. STANFORD UNIV CA DEPT OF AERONAUTICS AND ASTRONAUTICS, 1999.

[89] Qing, Xinlin P., *et al*. "Advances in the development of built-in diagnostic system for filament wound composite structures." Composites science and technology 66.11-12 (2006): 1694-1702.

[90] De Rosa, Igor Maria, *et al*. "Use of PVDF as acoustic emission sensor for in situ monitoring of mechanical behaviour of glass/epoxy laminates." Polymer Testing 29.6 (2010): 749-758.

[91] Caneva, C., *et al*. "Monitoring of Impacted Aramid-Reinforced Composites by Embedded PVDF Acoustic Emission Sensors." Strain 44.4 (2008): 308-316.

[92] Park, Joung-Man, *et al*. "Nondestructive damage detection and interfacial evaluation of single-fibers/epoxy composites using PZT, PVDF and P (VDF-TrFE) copolymer sensors." Composites Science and Technology 65.2 (2005): 241-256.

[93] Blanas, P., *et al*. "Composite piezoelectric materials for health monitoring of composite structures." MRS Online Proceedings Library (OPL) 604 (1999).

[94] Schulze, Robert, *et al*. "Fiber-reinforced composite structures with embedded piezoelectric sensors." SENSORS, 2014 IEEE. IEEE, 2014.

[95] Bae, Ji-Hun, *et al*. "Characterization of low-velocity impact-induced damages in carbon/epoxy composite laminates using a poly (vinylidene fluoride–trifluoroethylene) film sensor." Composites Part B: Engineering 135 (2018): 189-200.

[96] Zhao, Gang, *et al*. "Impact localization on composite laminates using fiber Bragg grating sensors and a novel technique based on strain amplitude." Optical Fiber Technology 40 (2018): 172-179.

[97] Morse, Llewellyn, *et al*. "Reliability based impact localization in composite panels using Bayesian updating and the Kalman filter." Mechanical Systems and Signal Processing 99 (2018): 107-128.

[98] Fu, Heming, *et al*. "Fast detection of impact location using kernel extreme learning machine." Neural Computing and Applications 27.1 (2016): 121-130.

[99] Lopes Jr, Vicente, *et al*. "Impedance-based structural health monitoring with artificial neural networks." Journal of Intelligent Material Systems and Structures 11.3 (2000): 206-214.

[100] Park, Sang Oh, *et al*. "Detection of impact location for composite stiffened panel using FBG sensors." Advanced Materials Research. Vol. 123. Trans Tech Publications Ltd, 2010.

[101] Yue, N., *et al*. "Assessment of impact detection techniques for aeronautical application: ANN vs. LSSVM." Journal of Multiscale Modelling 7.04 (2016): 1640005.

[102] Seno, Aldyandra Hami, *et al*. "Impact localisation in composite plates of different stiffness impactors under simulated environmental and operational conditions." Sensors 19.17 (2019): 3659.

[103] Xiong, An-ping, *et al*. "Energy efficient multiresource allocation of virtual machine based on PSO in cloud data center." Mathematical Problems in Engineering 2014 (2014).

[104] Kang, Fei, *et al*. "Concrete dam deformation prediction model for health monitoring based on extreme learning machine." Structural Control and Health Monitoring 24.10 (2017): e1997.

[105] Na, S., *et al*. "Neural network approach for damaged area location prediction of a composite plate using electromechanical impedance technique." Composites Science and Technology 88 (2013): 62-68.

[106] De Oliveira, Mario A., *et al*. "Use of savitzky–golay filter for performances improvement of SHM systems based on neural networks and distributed PZT sensors." Sensors 18.1 (2018): 152.

[107] Palomino, Lizeth Vargas, *et al*. "Probabilistic neural network and fuzzy cluster analysis methods applied to impedance-based SHM for damage classification." Shock and Vibration 2014 (2014).

[108] AlThobiani, Faisal, *et al*. "An application to transient current signal based induction motor fault diagnosis of Fourier–Bessel expansion and simplified fuzzy ARTMAP." Expert Systems with Applications 40.13 (2013): 5372-5384.

[109] De Oliveira, Mario A., *et al*. "Performance analysis of simplified Fuzzy ARTMAP and Probabilistic Neural Networks for identifying structural damage

growth." Applied Soft Computing 52 (2017): 53-63.

[110] Alom, Md Zahangir, *et al*. "The history began from alexnet: A comprehensive survey on deep learning approaches." arXiv preprint arXiv:1803.01164 (2018).

[111] LeCun, Yann, *et al*. "Deep learning." nature 521.7553 (2015): 436-444.

[112] Antholzer, Stephan, *et al*. "Deep learning for photoacoustic tomography from sparse data." Inverse problems in science and engineering 27.7 (2019): 987-1005.

[113] Cai, Yongxing, *et al*. "Subwavelength ultrasonic imaging using a deep convolutional neural network trained on structural noise." Ultrasonics 117 (2021): 106552.

[114] Rautela, Mahindra, *et al*. "Combined two-level damage identification strategy using ultrasonic guided waves and physical knowledge assisted machine learning." Ultrasonics 115 (2021): 106451.

[115] Keshmiri Esfandabadi, Yasamin, *et al*. "Deep learning for enhancing wavefield image quality in fast non-contact inspections." Structural Health Monitoring 19.4 (2020): 1003-1016.

[116] Ebrahimkhanlou, Arvin, *et al*. "A generalizable deep learning framework for localizing and characterizing acoustic emission sources in riveted metallic panels." Mechanical Systems and Signal Processing 130 (2019): 248-272.

[117] Song, Homin, *et al*. "Noncontact super-resolution guided wave array imaging of subwavelength defects using a multiscale deep learning approach." Structural Health Monitoring 20.4 (2021): 1904-1923.

[118] Ahmed, Shahed, *et al*. "DSWE-Net: A deep learning approach for shear wave elastography and lesion segmentation using single push acoustic radiation force." Ultrasonics 110 (2021): 106283.

[119] Alom, Md Zahangir, *et al*. "Object recognition using cellular simultaneous

recurrent networks and convolutional neural network." 2017 International Joint Conference on Neural Networks (IJCNN). IEEE, 2017.

[120] Lakhani, Vrishabh Ajay, *et al*. "Multi-Language Identification Using Convolutional Recurrent Neural Network." arXiv preprint arXiv:1611.04010 (2016).

[121] Long, Jonathan, *et al*. "Fully convolutional networks for semantic segmentation." Proceedings of the IEEE conference on computer vision and pattern recognition. 2015.

[122] Moeskops, Pim, *et al*. "Automatic segmentation of MR brain images with a convolutional neural network." IEEE transactions on medical imaging 35.5 (2016): 1252-1261.

[123] Ronao, Charissa Ann, *et al*. "Human activity recognition with smartphone sensors using deep learning neural networks." Expert systems with applications 59 (2016): 235-244.

[124] Mor, Etai, *et al*. "A unified deep network for beamforming and speckle reduction in plane wave imaging: A simulation study." Ultrasonics 103 (2020): 106069.

[125] Abdeljaber, Osama, *et al*. "Real-time vibration-based structural damage detection using one-dimensional convolutional neural networks." Journal of Sound and Vibration 388 (2017): 154-170.

[126] Abdeljaber, Osama, *et al*. "1-D CNNs for structural damage detection: Verification on a structural health monitoring benchmark data." Neurocomputing 275 (2018): 1308-1317.

[127] De Oliveira, *et al*. "A new structural health monitoring strategy based on PZT sensors and convolutional neural network." Sensors 18.9 (2018): 2955.

[128] Chen, Fu-Chen, *et al*. "NB-CNN: Deep learning-based crack detection using

convolutional neural network and Naïve Bayes data fusion." IEEE Transactions on Industrial Electronics 65.5 (2017): 4392-4400.

[129] Xia, Min, *et al*. "Fault diagnosis for rotating machinery using multiple sensors and convolutional neural networks." IEEE/ASME transactions on mechatronics 23.1 (2017): 101-110.

[130] Janssens, Olivier, *et al*. "Convolutional neural network based fault detection for rotating machinery." Journal of Sound and Vibration 377 (2016): 331-345.

[131] Jeong, Haedong, *et al*. "Rotating machinery diagnostics using deep learning on orbit plot images." Procedia Manufacturing 5 (2016): 1107-1118.

[132] Guo, Sheng, *et al*. "A novel fault diagnosis method for rotating machinery based on a convolutional neural network." Sensors 18.5 (2018): 1429.

[133] Qi, Yumei, *et al*. "Stacked sparse autoencoder-based deep network for fault diagnosis of rotating machinery." Ieee Access 5 (2017): 15066-15079.

[134] Garrido, I., *et al*. "Introduction of the combination of thermal fundamentals and Deep Learning for the automatic thermographic inspection of thermal bridges and water-related problems in infrastructures." Quantitative InfraRed Thermography Journal (2022): 1-25.

[135] Nguyen, Thanh-Truong, *et al*. "Deep learning-based autonomous damage-sensitive feature extraction for impedance-based prestress monitoring." Engineering Structures 259 (2022): 114172.

[136] Gao, Fei, *et al*. "Damage characterization using CNN and SAE of broadband Lamb waves." Ultrasonics 119 (2022): 106592.

[137] Zhang, Han, *et al*. "Data Anomaly Detection for Bridge SHM Based on CNN Combined with Statistic Features." Journal of Nondestructive Evaluation 41.1 (2022): 1-13.

[138] Agarwal, Akshit, *et al*. "Development of a Machine Learning Based Model

for Damage Detection, Localization and Quantification to Extend Structure Life." Procedia CIRP 98 (2021): 199-204.

[139] Wang, Xinwei, *et al*. "A novel structural damage identification scheme based on deep learning framework." Structures. Vol. 29. Elsevier, 2021.

[140] Bao, Yuequan, *et al*. "Machine learning paradigm for structural health monitoring." Structural Health Monitoring 20.4 (2021): 1353-1372.

[141] Nelon, Christopher, *et al*. "The intersection of damage evaluation of fiber-reinforced composite materials with machine learning: A review." Journal of Composite Materials 56.9 (2022): 1417-1452.

[142] Belding, Matthew, *et al*. "A Machine learning-based approach to determining stress in rails." Structural Health Monitoring (2022): 14759217221085658.

[143] Taheri, Hossein, *et al*. "Artificial Intelligence, Machine Learning and Smart Technologies for Nondestructive Evaluation." Sensors 22.11 (2022): 4055.

[144] Li, Yixian, *et al*. "A convolutional neural network-based full-field response reconstruction framework with multitype inputs and outputs." Structural Control and Health Monitoring (2022): e2961.

[145] Rai, Akshay, *et al*. "Lamb wave based damage detection in metallic plates using multi-headed 1-dimensional convolutional neural network." Smart Materials and Structures 30.3 (2021): 035010.

[146] Wang, Zilong, *et al*. "Unsupervised deep learning approach using a deep auto-encoder with a one-class support vector machine to detect damage." Structural Health Monitoring 20.1 (2021): 406-425.

[147] Bowler, Alexander L., *et al*. Watson. "A review of ultrasonic sensing and machine learning methods to monitor industrial processes." Ultrasonics (2022): 106776.

[148] Badabagni, Sai, *et al*. "Damage classification based on stiffness reduction in cross-ply laminates with convolution neural networks." Sensors and Smart Structures Technologies for Civil, Mechanical, and Aerospace Systems 2022. Vol. 12046. SPIE, 2022.

[149] Nwankpa, Chigozie, *et al*. "Activation functions: comparison of trends in practice and research for deep learning." arXiv preprint arXiv:1811.03378 (2018).

[150] Agostinelli, Forest, *et al*. "Learning activation functions to improve deep neural networks." arXiv preprint arXiv:1412.6830 (2014).

[151] Ding, Bin, *et al*. "Activation functions and their characteristics in deep neural networks." 2018 Chinese control and decision conference (CCDC). IEEE, 2018.

[152] Bingham, Garrett, *et al*. "Evolutionary optimization of deep learning activation functions." Proceedings of the 2020 Genetic and Evolutionary Computation Conference. 2020.

[153] ASTM Committee D-30 on Composite Materials. Standard test method for tensile properties of polymer matrix composite materials. ASTM International, 2008.

[154] Sheen, Bongjae, *et al*. "A study on quantitative lamb wave tomogram via modified RAPID algorithm with shape factor optimization." International Journal of Precision Engineering and Manufacturing 13.5 (2012): 671-677.

[155] Ono, Kanji. "A comprehensive report on ultrasonic attenuation of engineering materials, including metals, ceramics, polymers, fiber-reinforced composites, wood, and rocks." Applied Sciences 10.7 (2020): 2230.